

Ultra-broadband time-resolved THz spectroscopy of perovskites and nanomaterials

Présentée le 11 septembre 2020

à la Faculté des sciences de base
Groupe Moser
Programme doctoral en chimie et génie chimique

pour l'obtention du grade de Docteur ès Sciences

par

Andrés BURGOS CAMINAL

Acceptée sur proposition du jury

Prof. U. A. Hagfeldt, président du jury
Prof. J.-E. Moser, directeur de thèse
Prof. E. Cánovas Díaz, rapporteur
Prof. T. Feurer, rapporteur
Prof. M. Chergui, rapporteur

Resumé

L'étude fondamentale de la dynamique des porteurs de charges s'est révélée être d'un grand intérêt pour l'optoélectronique en ouvrant la voie à de futurs développements. Les processus clés qui déterminent la photophysique d'un matériau se produisent souvent sur des échelles de temps très courtes. Afin de les caractériser, des techniques de spectroscopie ultra-rapide à très haute résolution temporelle peuvent être utilisées. Celles-ci s'appuient sur des lasers délivrant des impulsions ultra-brèves, de durées de l'ordre de dizaines à des centaines de fs. L'une de ces techniques est la spectroscopie térahertz résolue en temps (TRTS, en anglais), particulièrement utile dans l'étude des semi-conducteurs en raison de sa sensibilité à la concentration et à la mobilité des porteurs de charge. Celle-ci peut également être utilisée pour étudier les vibrations de basse fréquence et d'autres espèces photo-excitées, telles que les excitons. Dans ce travail, nous nous concentrons sur les développements récents basés sur la photonique des gaz qui permettent d'étendre la gamme de fréquences sondées de la technique jusqu'à plus de 20 THz, ce qui lui vaut le nom de TRTS à ultra-large bande. Cette thèse est dédiée à cette dernière et à son application dans l'étude de deux des sujets les plus actuels en optoélectronique : les nanomatériaux et les pérovskites d'halogénures de plomb (LHP, en anglais). La TRTS est employée le plus souvent en combinaison avec d'autres techniques de spectroscopie. Les LHP sont devenus l'un des matériaux les plus étudiés ces dernières années en raison de leurs performances photovoltaïques exceptionnelles et de la multitude d'autres applications potentielles. Néanmoins, de nombreuses propriétés doivent encore être pleinement comprises. Différentes versions de LHP de faible dimensionnalité attirent de surcroît une attention croissante en raison de propriétés intéressantes, telles que leur stabilité, leur rendement quantique d'émission ou les effets de confinement.

Les chapitres 1 et 2 sont introductoires. Le premier présente à la fois la théorie et la littérature récente qui se rapportent aux chapitres suivants. Le deuxième donne des ex-

plications détaillées sur la TRTS à ultra-large bande, l'analyse des données, le montage expérimental et les particularités du substrat. Il offre également une description résumée des autres techniques résolues en temps qui ont été utilisées. Les chapitres suivants sont classés en fonction de la complexité et de la réalisation croissante du potentiel de la TRTS à ultra-large bande. Chacun se concentre sur un matériau différent, dont la photophysique particulière est étudiée par TRTS.

Le chapitre 3 est une étude photophysique résolue en temps de nano-fils de Se. Ce matériau suscite un grand intérêt pour ses applications potentielles, de la catalyse à l'optoélectronique. Ici, nous étudions des échantillons en couches minces obtenus à partir d'un nouveau processus de synthèse simplifié. La dynamique et la mobilité des porteurs de charges sont investiguées pour la première fois en utilisant des techniques de spectroscopie ultra-rapides.

Dans le chapitre 4, les LHP tridimensionnelles sont étudiées avec un intérêt pour l'évolution initiale des porteurs de charge, y compris le refroidissement des porteurs chauds et la formation de polarons. L'étude se concentre sur l'augmentation de la photoconductivité qui peut être observée dans des LHP de compositions diverses au cours de la première ps suivant l'excitation. Un modèle complexe est proposé sur la base des observations des dépendances de la fluence et de la longueur d'onde et qui permet d'unifier la description des mécanismes précédemment identifiés.

Enfin, le chapitre 5 se concentre sur l'étude des pérovskites 2D où les effets de confinement diélectrique et quantique modifient complètement la photophysique, conférant au matériau un fort caractère excitonique. Alors que les deux chapitres précédents se focalisent principalement sur l'utilisation de la dynamique TRTS à fréquence moyenne, ici des spectres résolus en fréquence ainsi que la spectroscopie de conversion ascendante de fluorescence à large bande sont également utilisés dans l'étude de la dynamique de conversion entre porteurs et excitons.

Mots-clés: spectroscopie THz à ultra-large bande, photonique des gaz, pérovskites d'halogénures de plomb, pérovskites 2D, nano-fils de Se, photophysique, dynamique des porteurs de charges, polarons, excitons.

Abstract

The fundamental study of charge carrier dynamics has been shown to be of great interest for optoelectronics, paving the way forward for future developments. Often, some of the key processes that determine the photophysics of a material occur on very short timescales. In order to study and characterize them, we can use time-resolved spectroscopic techniques on the ultrafast timescale. These generally rely on pulsed lasers with ultra-short pulse lengths, in the order of tens to hundreds of fs. One such technique is time-resolved THz spectroscopy (TRTS), especially useful in the study of semiconductors due to its sensitivity to charge carrier concentration and mobility. Nonetheless, it can also be used to study low energy vibrations and other photoexcited species such as excitons. In this work, we focus on recent developments based on gas photonics that easily enables the extension of the probed frequency range towards 20 THz and beyond, giving it the name of ultra-broadband TRTS. This dissertation revolves around the technique and its application to study two of the hottest topics in optoelectronics: nanomaterials and lead halide perovskites (LHPs). This is often done in combination with other spectroscopic techniques. LHPs have become one of the most studied materials in recent years due to their outstanding performance in photovoltaics and their multitude of other potential applications. Nonetheless, many properties still need to be fully understood. In addition, lower dimensionality variations of LHPs are gaining increasing attention due to interesting qualities such as stability, emission quantum yield and confinement effects.

Chapters 1 and 2 are introductory chapters. The former introduces both the theory and the recent literature that is relevant to the following chapters. Meanwhile, the latter gives a detailed explanation of ultra-broadband TRTS, including data analysis, setup description and substrate suitability. It also gives a summarized description of other time-resolved techniques that were employed. The following chapters are ordered in increasing complexity and realization of the potential of ultra-broadband TRTS. Each

one focuses on a different material, exploring different photophysics that can be studied with TRTS.

Chapter 3 is a time-resolved photophysical study of Se nanowires. These materials have generated great interest for their potential applications, from catalysis to optoelectronics. Here, we study thin-film samples obtained from a novel and simple solution-based synthesis process. The charge carrier dynamics and mobility are studied for the first time employing ultrafast techniques.

In chapter 4, bulk LHPs are studied with an interest towards the early evolution of charge carriers, including hot carrier cooling and polaron formation. The study focuses on the rise in photoconductivity that can be observed in LHPs of diverse composition over the first ps after excitation. It proposes a complex model to unify previously reported mechanisms based on the fluence and wavelength dependencies.

Finally, chapter 5 turns towards the study of 2D LHPs where the dielectric and quantum confinement effects completely alter the photophysics, resulting in a strong excitonic character. While the previous two chapters mainly focus on the use of frequency-averaged TRTS dynamics, this one also makes use of frequency-resolved spectra as well as broadband fluorescence up-conversion spectroscopy to study the carrier-exciton dynamics.

Keywords: ultra-broadband THz spectroscopy, gas photonics, lead halide perovskites, 2D perovskites, Se nanowires, photophysics, charge carrier dynamics, polarons, excitons.

Contents

1	Introduction	11
1.1	Semiconductor photophysics	12
1.1.1	Band structure	12
1.1.2	Phonons	14
1.1.3	Photoexcited states	15
1.2	Nanomaterials	22
1.3	Lead halide perovskites	23
1.3.1	Bulk properties	25
1.3.2	2D perovskites	27
	References	30
2	Spectroscopic techniques	39
2.1	THz spectroscopy	40
2.1.1	Introduction	40
2.1.2	Classical time-resolved THz technologies	40
2.1.3	Ultra-broadband THz pulses through gas photonics	43
2.1.4	Setup	52
2.1.5	Data analysis	54
2.1.6	Substrates	62
2.2	Ultrafast transient absorption spectroscopy	63
2.2.1	Setup	65
2.3	Broadband fluorescence up-conversion spectroscopy	66
2.3.1	Setup	66
2.4	Nanosecond flash photolysis	67
	References	68

3	Charge carrier dynamics and mobilities in Se nanowires	73
3.1	Introduction	74
3.2	Results and analysis	75
3.2.1	Sample characterization	75
3.2.2	Charge carrier dynamics	77
3.2.3	Charge carrier mobility	80
3.3	Conclusions	82
	References	83
4	Hot carrier dynamics in bulk lead halide perovskites	87
4.1	Introduction	88
4.2	Results and analysis	89
4.2.1	Sample	89
4.2.2	A slow rise of the TRTS signal	90
4.2.3	Simple model	94
4.2.4	Complex model	97
4.2.5	Additional measurements	102
4.3	Conclusions	103
	References	104
5	Exciton-carrier dynamics in lead halide 2D perovskites	109
5.1	Introduction	110
5.2	Results and analysis	112
5.2.1	Introductory results	112
5.2.2	Spectral analysis	113
5.2.3	Fluence dependence and kinetic modelling	120
5.2.4	Influence of the cation	125
5.3	Conclusions	128
	References	130
	Conclusions and outlook	137
	Acknowledgments	141
	Appendices	143

A	Supplementary figures and tables	145
A.1	THz setup	145
A.2	Charge carrier dynamics and mobilities in Se nanowires	147
A.3	Hot carrier dynamics in bulk lead halide perovskites	149
A.4	Exciton-carrier dynamics in lead halide 2D perovskites	153
B	Additional derivations	157
B.1	Current density from Maxwell's equations	157
B.2	Refractive index	160
B.3	Models in frequency	160
B.4	Exponential equations	161
B.5	Simple carrier cooling model	162
B.6	Competition model	163
B.7	Kinetic model for 2D perovskites	164
C	List of symbols and abbreviations	167

Chapter 1

Introduction

This chapter gives an introductory review of the theoretical background and the relevant topics for this thesis. It begins with an overview of semiconductor photophysics. Then, it gives an introduction to nanostructured semiconductors and their special properties. Finally, it details the properties of lead halide perovskites both in the bulk and 2D forms.

1.1 Semiconductor photophysics

Semiconductors are the intermediate materials between metals and insulators. While pure semiconductor crystals are insulators at absolute zero temperature, they can be conductive with a higher or lower magnitude under different circumstances. Thermal energy, impurities and defects, light excitations or high enough voltages can effectively induce conductivity. These properties make them extremely useful for many applications from electronics to photovoltaics. In order to understand how the properties of semiconductors arise it is necessary to start with the band structure.^{1,2}

1.1.1 Band structure

The electronic structure of solids is divided into bands of allowed energy states and band gaps of forbidden energies. These are a consequence of the interaction between electrons and nuclei. The energy of the band gap is represented by E_g . If a band is half-filled the material is a metal. In that case, the conductivity can be explained from all of the close-lying available states. The system can often be approximated to a Fermi electron gas and the conductivity (σ) can be obtained from Ohm's law, with the form

$$\sigma = \frac{Ne^2\tau}{m}, \quad (1.1)$$

where e is the electron charge, m is its mass and τ is the mean time between collisions where the electric field acts on the carrier to accelerate it. This will be shown as part of the Drude model in the next chapter.

As fermions, electrons follow Fermi-Dirac statistics due to the Pauli exclusion principle. The distribution of occupied states follows

$$f(\epsilon, T, \epsilon_F) = \frac{1}{\exp[(\epsilon - \epsilon_F)/k_B T + 1]}, \quad (1.2)$$

where ϵ is the energy, ϵ_F is the Fermi level or chemical potential, T is the temperature and k_B is the Boltzmann constant. We can understand ϵ_F as the energy where a state will have an occupancy probability of 50%. In addition, it defines the work needed to add an electron to the material, provided we define a proper energy reference (vacuum, SHE, etc.). In a simplified way, we can distinguish between a metal where a band is half filled, and an insulator where one of the bands is completely filled and the next is empty.

We generally define the filled band (at $T = 0$ K) as the valence band while the first empty, or partially filled, band is the conduction band. At room temperature, intrinsic semiconductors are a special case of insulators where the bandgap is small enough that some electrons are promoted thermally according to Equation 1.2. This means that some electrons are present in the conduction band and some vacancies (holes) are left in the valence band (Figure 1.1). Electrons and holes are known as charge carriers, both of them giving rise to the conductivity.

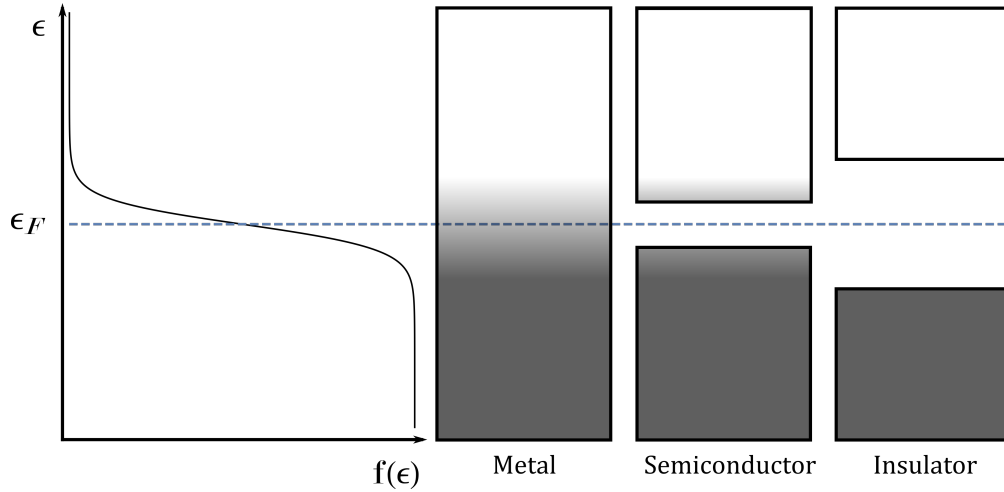


Figure 1.1: Scheme representing the band filling of a metal, a semiconductor and an insulator at room temperature. The Fermi level is represented by the dashed line.

Electrons in a band are characterized by a certain momentum or wavevector (k). Thus, band structures are typically plotted as a function of ϵ and k . This allows to directly distinguish between a direct and an indirect semiconductor. The former is characterized by having the conduction band minimum (CBM) and the valence band maximum (VBM) aligned on the same k . In that case, a photon of angular frequency ω , where

$$E_g \leq \hbar\omega, \quad (1.3)$$

is enough to produce the transition between the two band edges. On the contrary, in an indirect semiconductor the CBM and VBM have a k mismatch. In that case, an optical transition just across the bandgap requires a change in momentum much larger than the one carried by a photon, which is negligible at optical energies. In that case, emission

or absorption of phonons, quasiparticles corresponding to quanta of lattice vibrations, can supply the necessary change in k . Thus, the transition can occur when

$$E_g \leq \hbar\omega \pm \hbar\Omega, \quad (1.4)$$

where Ω , the angular frequency of the phonon, is typically much smaller than ω .

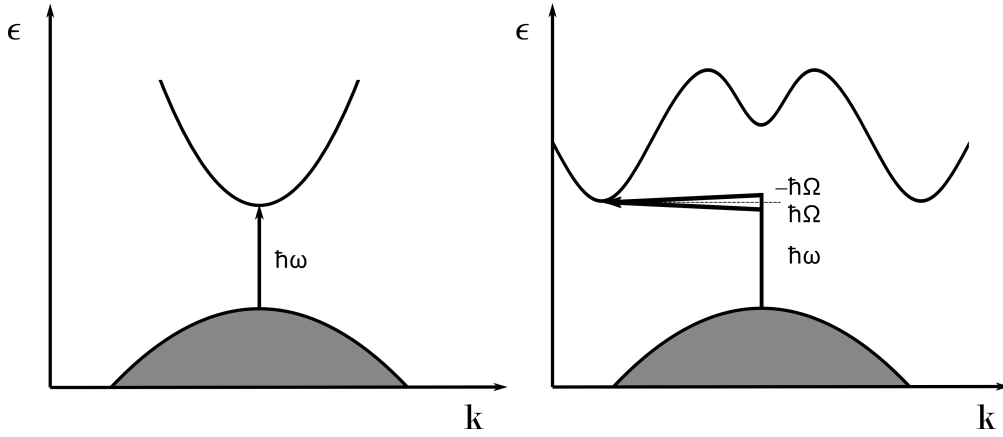


Figure 1.2: Difference in the band structure between a direct (left) and an indirect (right) semiconductor.

Indirect transitions are dependent on temperature since it determines the availability of phonons. In addition, being a two-step process, indirect transitions have a lower probability than direct ones. This explains the enhanced absorption coefficients of direct semiconductors such as lead halide perovskites compared to indirect ones such as crystalline silicon.³

1.1.2 Phonons

As previously mentioned, phonons are energy quanta of lattice vibrations. n phonons are generated when a vibrational mode is excited to the quantum number n . They are analogous to photons in electromagnetic waves. Unlike electrons, phonons follow Bose-Einstein statistics, where the phonon occupancy for a certain frequency Ω is given by

$$n = \frac{1}{\exp(\frac{\hbar\Omega}{k_B T}) - 1}. \quad (1.5)$$

Phonons are divided into transverse (T) and longitudinal (L) modes. The latter corresponds to oscillations in the propagation direction while the former corresponds to

perpendicular ones. Equally, when there is more than one atom in the unit cell of a solid, the phonons are further divided into optical (O) and acoustical (A) phonons, giving a total of four kinds of phonons: LO, TO, LA and TA. Acoustical phonons correspond to coherent oscillations with a net displacement of the center of mass, much like acoustic waves. On the contrary, optical phonons correspond to out-of-phase oscillations. Their name comes from the fact that they can interact with light. A representation of the four kinds of modes is shown in Figure 1.3. Acoustical phonons generally have a lower energy than optical ones.¹

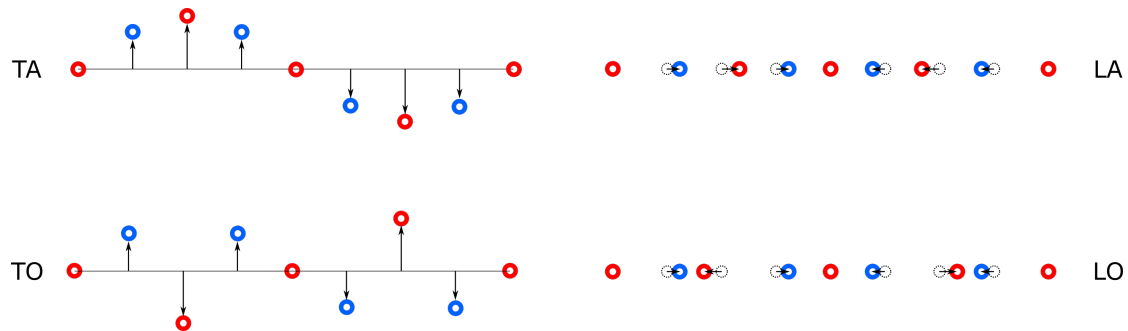


Figure 1.3: Schematic representation of the four kinds of phonons in a 1D lattice.

1.1.3 Photoexcited states

As implied earlier, semiconductors can interact with photons to promote electrons between bands, leading to different photoexcited states or particles and quasiparticles that, if present, occur at lower concentrations in the dark. These states include simple charge carriers but also excitons and polarons as well as more complex ones such as plasmons or polaritons that will not be treated in this text.

1.1.3.1 Charge carriers

As stated earlier, charge carriers are composed of electrons and holes. These can be produced by promoting an electron between the bands through photon absorption. Otherwise, they can already be present due to the thermal distribution or doping. In an intrinsic semiconductor, the Fermi level lies in-between the two bands. Therefore, in the dark, the only carriers present originate from thermal excitations according to the Fermi-Dirac distribution (Equation 1.2). However, defects and impurities can change

this, shifting the Fermi level. The presence of an impurity atom, replacing another from the lattice with an excess or a lack of electrons, will constitute a source of electrons and holes, respectively. These are also known as donor and acceptor impurities. In fact, the intentional addition of these impurities is called doping, a key process in the technological application of semiconductors. Furthermore, defects such as vacancies or interstitial atoms can also act as acceptor and donor states. Many of these defects and impurities lie at energies close to the band edge and can be observed as a tail of the optical absorption. Moreover, defect states in the band gap can become traps for the carriers, as they lie lower in energy than the band edge. Depending on the energy difference, these can be classified into deep and shallow traps. Traps play an important role in the charge carrier dynamics and recombination mechanisms.

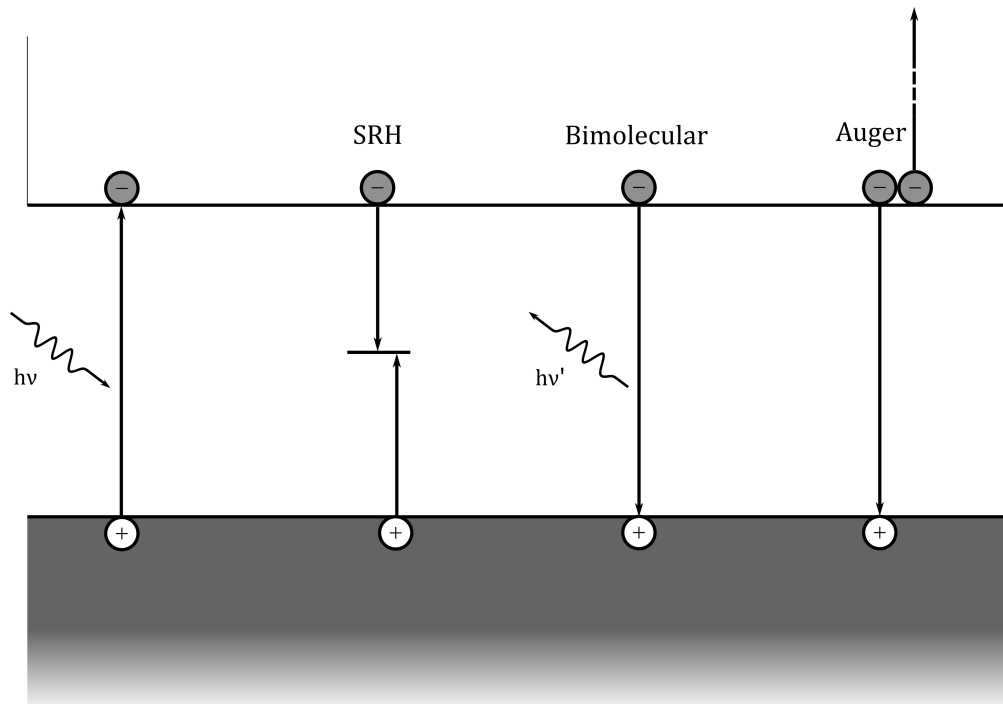


Figure 1.4: Schematic representation of carrier photoexcitation and the three types of recombination.

There are three main mechanisms for charge carrier recombination:

- Shockley-Read-Hall (SRH), also known as trap-assisted or simply monomolecular

recombination, is characterized by a recombination rate that varies linearly with carrier concentration. This is explained through the assumption that recombination takes place in recombination centers (traps) where carriers “fall” monomolecularly.^{4,5}

- Bimolecular recombination, where an electron and a hole recombine, potentially through the formation of an exciton. This process is typically radiative, especially in direct semiconductors. The recombination rate increases quadratically with the carrier concentration since the process involves two carriers.
- Auger recombination, named after the Auger effect, involves three carriers where an electron and a hole recombine transferring the energy to a third carrier that becomes hot. It then relaxes back to the band edge through phonon emission. Thus it is a nonradiative recombination mechanism and its rate is a cubic function of the carrier concentration.²

From these models, charge carrier recombination can be modeled as

$$\frac{dN}{dt} = -k_1N - k_2N^2 - k_3N^3, \quad (1.6)$$

where N is the carrier density and k_1 , k_2 and k_3 are the rate constants that predominantly describe the three processes mentioned before. These may also include other monomolecular, bimolecular or trimolecular processes, respectively.

Charge carriers are the source of photoconductivity ($\Delta\sigma$), the rise in conductivity upon illumination. It can be defined as

$$\Delta\sigma = eN\mu, \quad (1.7)$$

where e is the electron charge, N the charge carrier density and μ is the mobility. This can be further expanded to differentiate between electron (μ_e) and hole (μ_h) mobilities.⁶

$$\Delta\sigma = e(N_e\mu_e + N_h\mu_h). \quad (1.8)$$

However, throughout this work, we will consider that the photoconductivity is either dominated by one of the two or results from an average mobility. Under the Drude model, that will be further explained in the next chapter, the mobility follows

$$\mu = \frac{e\tau}{m^*}, \quad (1.9)$$

where τ is a scattering constant and m^* is the effective mass of the carrier. Logically, this expresses the fact that the mobility is indirectly proportional to the mass of the carrier. To understand the implications it is best to describe the origin and meaning of the effective mass.

In the periodic potential of a lattice, electrons are accelerated under an electric field as if they had an effective mass different from the mass of a free electron. At the band edge $\epsilon(k)$ is often approximated to the parabolic relationship

$$\epsilon(k) = \epsilon_0 + \frac{\hbar^2 k^2}{2m^*}, \quad (1.10)$$

where the curvature of the parabola is

$$\rho = \frac{d^2 \epsilon}{dk^2} = \frac{\hbar^2}{m^*}, \quad (1.11)$$

inversely proportional to m^* . Thus, carriers lying on high curvature valleys, typically at the band edge, present a lower m^* and a higher μ . When carriers are excited with excess energy the transition can occur at different k than the CBM. In addition, electrons with excess energy can scatter towards other valleys interacting with phonons. In those cases there will be a difference in μ between the relaxed carriers at the band edge and the hot carriers.^{1,7} This can be used to explore hot carrier cooling through μ -sensitive time-resolved techniques.

Typically, the effective mass in a semiconductor is lower than the free electron, with values usually in the 0.1-0.01 range.¹ However, exceptions, such as heavy fermion materials, exist.⁸

1.1.3.2 Excitons

Due to Coulomb interactions, electrons and holes can be bound into a quasiparticle known as an exciton. Excitons are characterized by a binding energy E_b that describes the strength of the interaction. Often, semiconductors show an absorption peak below the bandgap energy that corresponds to the excitons, and the difference in energy is given by E_b . In addition, excitons are neutral quasiparticles that can diffuse through the crystal and carry energy. Depending on the strength of E_b , excitons can be divided

into tightly bound Frenkel excitons and weakly bound Wannier-Mott excitons.¹

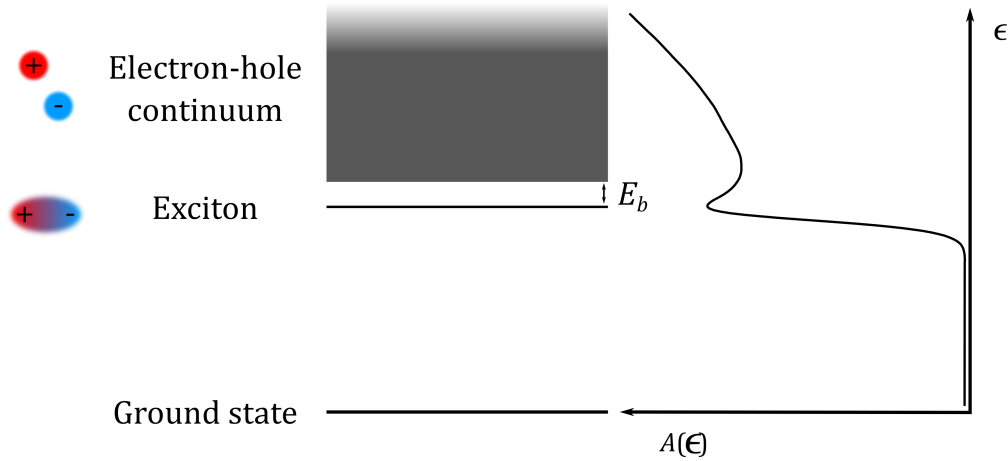


Figure 1.5: An adapted Jablonski diagram, where the exciton state and the electron-hole continuum are shown to correspond to the Absorbance ($A(\epsilon)$) spectrum of a direct semiconductor (CsPbBr_3) with a clear excitonic peak.

Frenkel excitons are small tightly bound excitons localized on a single atom or molecule, in the case of an organic semiconductor, presenting a large E_b . It can be understood as an excited state that diffuses through hopping. These are typical of low dielectric materials, since the electron-hole correlations and, therefore, E_b increase as the permittivity decreases.

Wannier-Mott excitons, on the other hand, show a much weaker interaction between the electron and the hole, which are separated across a larger distance than the lattice constant. These quasi-particles are generally understood as hydrogen atom-like systems characterized by a Bohr radius given by $R_b = \frac{\epsilon \hbar^2}{\mu e^2}$, where μ , not to be confused with the mobility, is the reduced mass of the exciton, $\mu = (\frac{1}{m_e} + \frac{1}{m_h})^{-1}$.⁹ As the permittivity ϵ increases, R_b increases, giving a more loosely bound pair due to the charge screening of the carriers by the lattice. Consequently, E_b is lower and excitons tend to split into free charges with thermal energy.

Exciton recombination generally proceeds through either monomolecular or bimolecu-

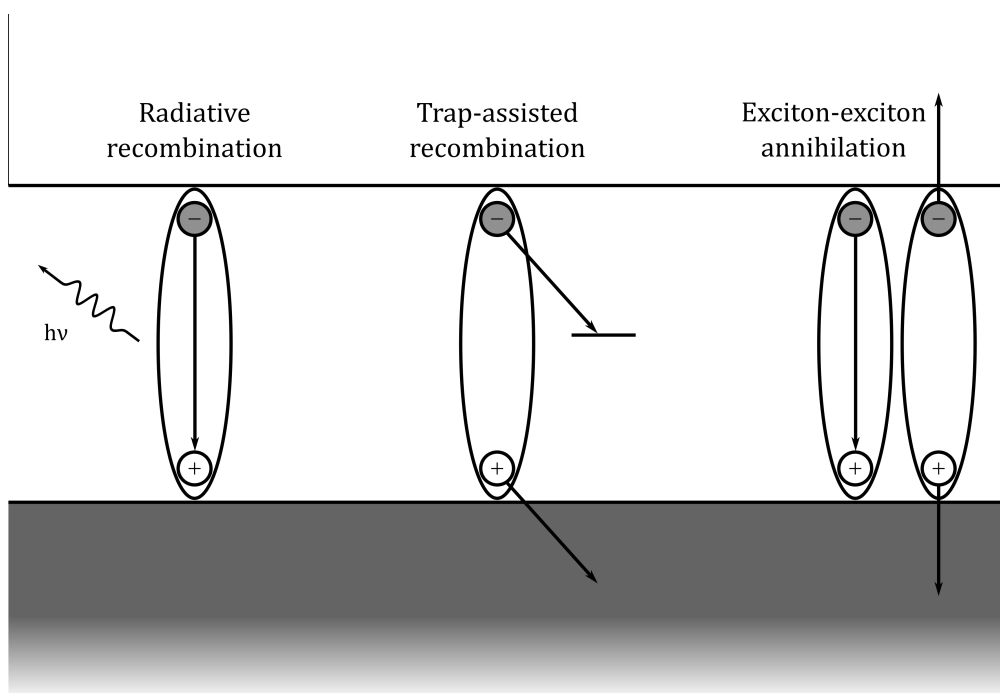


Figure 1.6: Exciton recombination mechanisms.

lar pathways. Among the first, the most common and straightforward mechanism is radiative recombination where the electron falls into the hole and emits a photon. Otherwise, excitons can also undergo trap assisted non-radiative recombination, where one of the carriers forming the exciton falls into a trap state and the other is promoted into its respective band. This is, therefore, an Auger type of process, but it involves only one exciton.^{10,11} Finally, the most common bimolecular recombination pathway is exciton-exciton annihilation, another Auger process where an exciton recombines while transferring its energy to a second exciton, which can either go to a higher excitonic state or split into carriers.¹²⁻¹⁵

1.1.3.3 Polarons

When charge carriers are present in a polarizable solid, such as polar crystals or ionic semiconductors, they form a quasiparticle known as a polaron. It can be described as the combination of a carrier with its self-induced polarization of the lattice.¹⁶ The

simplest theoretical description of polarons considers the interaction between carriers in a parabolic band, without spin or relativistic effects, and LO phonons. These are the so called standard or Fröhlich polarons. The theoretical background is based on the work from Landau¹⁷ and Pekar,¹⁸ and finally derived by Fröhlich in 1954.¹⁹ From it, the Fröhlich coupling constant (α) can be obtained as

$$\alpha = \frac{e^2}{\hbar c} \sqrt{\frac{m_b c^2}{2\hbar\omega_{LO}}} \left(\frac{1}{\varepsilon_{\text{inf}}} - \frac{1}{\varepsilon_0} \right), \quad (1.12)$$

where m_b is the carrier effective mass in the band, $\hbar\omega_{LO}$ is the phonon energy and ε_{inf} and ε_0 , not to be confused with the vacuum permittivity, are the electronic and static permittivities of the crystal, respectively.

Fröhlich polaron theories can be divided depending on their coupling regime (the strength of α) into strong,^{18,20} weak¹⁹ and intermediate couplings, where the last one generally includes all-coupling theories.¹⁶ Feynman's path integral is regarded as the most successful all-coupling approach.²¹

It is common to describe Fröhlich polarons as “large polarons” because the induced polarization extends over more than a unit cell. On the other hand, there exists a second type of polarons called “small polarons”. These are considered to be trapped by their self-induced polarization in a region of the order of a unit cell. Therefore, they are governed by short-range forces and the atoms immediately around it. In that case, Fröhlich's continuum approximation does not hold and must be treated in a different way. It is worth noting that, since small polarons are trapped in a self induced potential well, their transport properties are completely different. The movement is produced through a hopping mechanism that is thermally activated. This means that it depends on the availability of phonons and the mobility can be approximated to

$$\mu_{sp} \propto n_{ph} \sim e^{-\hbar\omega_{LO}/k_B T}, \quad (1.13)$$

where n_{ph} is the phonon density, at low enough temperatures. This is the complete opposite to Fröhlich polarons which exhibit a band-like transport limited by polaron-phonon scattering. In that case, the mobility decreases with temperature similar to

$$\mu_{Fp} \sim e^{\hbar\omega_{LO}/k_B T}. \quad (1.14)$$

In general, the effective mass of a polaron can be expected to be larger than the bare carrier due to the lattice displacement that it carries. As an example, in the weak carrier regime, derived by Fröhlich, the effective mass is given by

$$m^* = \frac{m_b}{1 - \alpha/6}. \quad (1.15)$$

Since α is always positive, with values in the 0.2-6 range, m^* will be larger than m_b .¹⁶

1.2 Nanomaterials

We can define a nanomaterial as having at least one dimension reduced to the 1-100 nm range. Depending on the number of dimensions that remain at bulk proportions we can speak of 3D or bulk materials; 2D, such as nanoplatelets or thin films and quantum wells; 1D, like nanowires or nanotubes; and 0D, commonly known as nanoparticles, quantum dots and nanoclusters. All of these structural confinements typically have strong consequences on their properties, such as bandgap, wettability, conductivity, melting point or light scattering.²² The origin of these changes can be divided into surface and quantum confinement effects.²³

Surface effects originate from the increase in the fraction of atoms lying on the surface which occurs as the volume decreases. In a sphere, the surface scales with r^2 while the volume scales with r^3 . Therefore, at small enough volumes a large fraction of atoms are at the surface. This fraction is also called dispersion. Atoms on the surface have a lower coordination number, which means they are less stable and can form bonds with adsorbing molecules. This is also the reason for nanoparticles presenting a lower melting point.²³ Furthermore, the increased dispersion produces a rise in the importance of surface states.²⁴ These may lie in the bandgap, behaving as traps and non-radiative recombination centers.²⁵

Quantum confinement effects directly affect the electronic structure of the material. As the spatial dimensions of a semiconductor decrease to *ca.* the exciton Bohr radius, a blue-shift of the absorption and emission spectra can be observed. Considering an “electron in a box” perspective, as the diameter of a particle becomes similar to the electron wavelength the energy levels become increasingly discrete.²⁶ Logically, the density of states equally decreases. Depending on the number of dimensions that are affected, the

density of states is altered in a different way, until reaching a molecular scenario for the smallest clusters (Figure 1.7). In addition, the band edge is more strongly affected and the result is a widening of the gap.²⁷ Moreover, the effect is gradual. This means that quantum dots emitting in all parts of the visible spectrum can be obtained from the same composition just by varying the size.²³ On the other hand, Kayanuma showed that strong quantum confinement effects are to be expected from the moment the particle is as small as twice the exciton Bohr radius.⁹

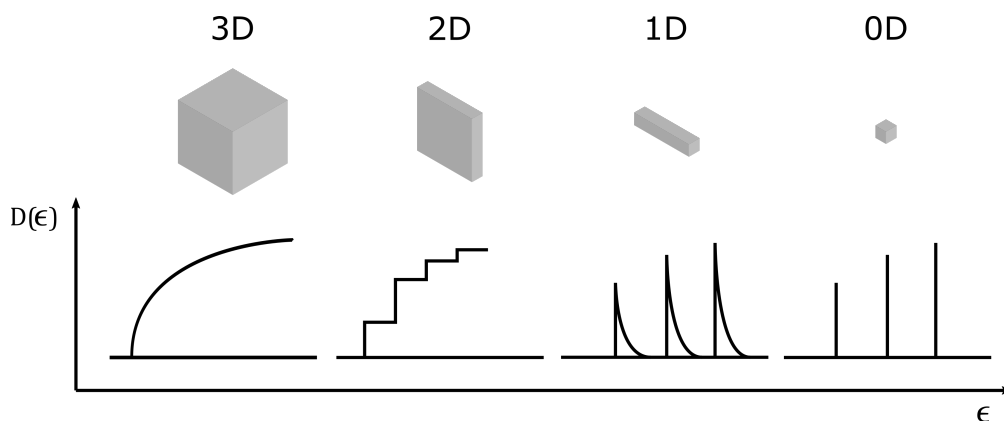


Figure 1.7: Schematic representation of the effects of quantum confinement in the density of states depending on the number of dimensions. Inspired from ref. [27]

There can be an additional effect called dielectric confinement. It is caused by the strong decrease in permittivity from the semiconductor to the ligands used to stabilize the nanostructure.^{28,29} This enhances correlations between electrons and holes that can largely increase the exciton binding energy.

1.3 Lead halide perovskites

In the past decade a family of materials have attracted a large part of the photovoltaic research effort and attention. These are the famous lead halide perovskites (LHP), also known as hybrid organic-inorganic perovskites (HOIP), where the latter highlights that some of the most used compositions contain organic cations. LHPs can be described through the general composition ABX_3 , where A is a voluminous monovalent cation,

usually methylammonium (CH_3NH_3^+) but also formamidinium ($\text{NH}_2\text{CHNH}_2^+$) or Cs^+ , B is a divalent heavy metal cation such as Pb^{2+} , and X is a halide (I^- , Br^- , Cl^-). In fact, the term “perovskite” includes all the possible materials with the ABX_3 formula showing a cubic crystalline structure formed by BX_6 octahedra in the corners and the A cation in the center (Figure 1.8).^{30–33} In addition, the structure includes several families of minerals including the original titanate perovskites like CaTiO_3 .³⁴ However, the purely cubic structure is usually present only at higher temperatures. In the case of $\text{CH}_3\text{NH}_3\text{PbI}_3$ for example, the organic cation has a higher degree of rotation in those conditions, giving an overall cubic symmetry. Otherwise, the preferred orientations of the cation distorts the unit cell into a rectangular prism giving a tetragonal phase at ambient temperature and an orthorhombic phase at low temperatures.^{31,35}

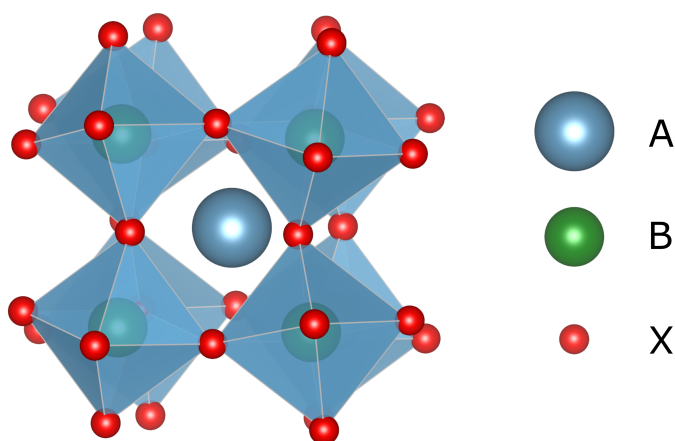


Figure 1.8: Example of a perovskite structure representation³⁶ taken from CaTiO_3 crystallographic data.³⁴ Notice that the distortion in the structure is also present in this mineral.

LHPs have attracted a great deal of attention due to the fast improvement and high power conversion efficiencies (PCE), with low processing costs, of perovskite solar cells (PSC). This easy-to-handle material has allowed many research teams in fairly common chemistry labs to carry out research at an accelerated pace. Between the years 2012 and 2020 the certified PCE of single junction PSCs has risen to 25.2%, in direct com-

petition with well established technologies like silicon or CIGS.³⁷ The first use of hybrid perovskites in solar cells was reported by Miyasaka's group in 2009 where it substituted the dye in a dye-sensitized solar cell (DSSC) in the form of nanoparticles with a PCE of 3.8%.³⁸ The inherent instability of the material in contact with a polar electrolyte limited its durability and efficiency. Further improvements were carried out by N.-G. Park and coworkers³⁹ until the idea of substituting the liquid electrolyte by the HTM Spiro-OMeTAD, used before in solid state DSSCs, gave the appropriate stability to the cell, showing even higher PCEs, reaching 9.7%.⁴⁰ This was quickly followed by further improvements by H. Snaith *et al.*⁴¹ going beyond 10% efficiency that rapidly escalated into the rush towards 20% in the following years.³⁵

Progress in the PCE has lost some momentum in the last few years and the focus has partially shifted towards improving other aspects such as the stability or toxicity as well as other applications such as light emitting devices, lasing or photodetectors.⁴² This is why related systems such as 2D perovskites are attracting a lot of attention. To conclude this introduction, we will review the properties of perovskites in the bulk and in 2D confined systems, which are two of the main subjects of study in this thesis.

1.3.1 Bulk properties

LHPs have a sharp optical band edge with a strong panchromatic absorption, owing to their direct bandgap, that is ideal for photovoltaic applications. Due to spin-orbit coupling from the presence of heavy atoms, such as lead or iodine, the conduction band is split into two, lowering the CBM.⁴³ In addition, the width of the bandgap is extremely tunable depending on the ionic compositions, with values that can range from 1.15 to 3.06 eV.⁴² For example, changes in the halide from I^- to Br^- or Cl^- will increase the bandgap due to a shift in the valence band.⁴⁴ Similarly, a change in the metal from Pb^{2+} to Sn^{2+} can decrease the bandgap. Interestingly, a gradual shift can be obtained through partial substitution and mixed compositions. In the end, a large part of the research effort has been directed towards the optimization of the right composition in order to enhance stability and performance.^{42,45,46}

Part of the reason why these materials have such an excellent photovoltaic performance lies in the surprisingly long charge carrier lifetimes, for a direct semiconductor, typi-

cally lying in the hundreds of ns to even several μs . It was shown that bimolecular recombination was particularly slow compared to what is expected from the Langevin model.^{43,47} This model establishes the limit for the ratio between recombination rate and mobility, assuming that recombination will occur once the electron and the hole enter their respective capture radii. However, the observed rates and mobilities picture a recombination scenario that is up to four orders of magnitude slower. This is highly desirable for photovoltaic applications and its origin has been extensively debated.⁴³ Indeed, the combination of considerable mobilities,⁴⁸ typically in the order of 1 to 100 $\text{cm}^2 \text{V}^{-1} \text{s}^{-1}$,⁴⁸ with low recombination rates,⁴⁹ give rise to long diffusion lengths and efficient extraction in sub-micron films.⁵⁰

Much attention has been devoted towards two possible explanations coming from either a Rashba effect^{51,52} or the polaronic nature of the carriers.⁵³⁻⁵⁵ While the latter will be given more importance in this dissertation, especially in Chapter 4, the former is also worth mentioning. Briefly, spin-orbit coupling produces a spin-splitting of the bands in the k dimension. However, this is not identical for the two bands, resulting in a slight indirect nature of the bandgap. Thus, k preservation makes recombination of relaxed carriers a slow process.⁵⁶ In addition, some results suggest that the resulting electronic structure makes recombination a spin-forbidden transition.⁵⁷ Polarons, on the other hand, would explain lower recombination rates from the screening effects of the polarization clouds surrounding the carriers.⁵³ Certainly, polarons are to be expected in such an ionic material, but the evidence has been piling up in favor of the fact that they are an important element in the description of charge carriers in LHPs. One of the first hints came from the temperature dependence of the mobility, which was shown to follow a $T^{-3/2}$ dependence.⁵⁸ This is typical of a mobility governed by acoustic phonon-electron scattering instead of impurity scattering. The decreasing mobility with temperature is consistent with the polaron picture. In addition, recent measurements of polaron formation and calculations have improved the understanding.^{54,59} Furthermore, polaron screening can help explain the long cooling times observed in these materials.^{55,60} Indeed, hot carrier cooling is particularly slow for LHPs at high excitation densities. This is usually explained through a hot phonon bottleneck effect, where the temperature of the LO phonon bath reaches the temperature of the hot carriers and the cooling becomes limited by phonon decay.^{61,62} This can be combined with acoustic phonon up-conversion⁶³

and Auger heating.⁶¹ Moreover, cooling times of over 100 ps have been observed and it has been proposed that these hot carriers are also protected as large polarons, even from cooling through the interaction with lattice phonons.⁵⁵

One key parameter, and the major limitation, for LHPs is the stability of the most useful compositions, which readily degrade under ambient conditions, especially in high humidity environments.⁶⁴ While improvements can be made in the halide composition⁶⁵ or layer engineering,⁶⁴ one of the most promising pathways is the use of layered perovskites, a family of nanostructured materials also known as 2D perovskites.^{66–70}

1.3.2 2D perovskites

The perovskite structure for the ABX_3 composition is only obtained under the right conditions. Given the radii R_A , R_B and R_X of the three ions, we can define the Goldschmidt tolerance factor $t = \frac{R_A + R_X}{\sqrt{2(R_B + R_X)}}$.⁷¹ For a 3D perovskite structure to be formed, it has been empirically found that t must be between 0.8 and 1. Nonetheless, if other stoichiometric proportions are used with larger cations, new structures can be formed that no longer follow the rule.⁷² Consequently, these are no longer the 3D structures of corner-sharing octahedra seen in Figure 1.8. Indeed, different lower dimensionality structures such as 2D,⁷³ where corner-sharing octahedra form a plane, 1D,⁷⁴ where they form a nanowire, or even 0D,⁷⁵ where they are isolated, can be obtained. All of them can be tuned in their properties depending on the composition. Furthermore, they are not as limited by the Goldschmidt factor and give a larger flexibility to explore different property changes.⁷² Certainly, colloidal nanocrystals and nanoplatelets can also be synthesized as nanostructured perovskites but their crystalline structure is based on either the 3D or the 2D.^{76,77} Here, we are particularly interested in the 2D perovskites as they have a deeper relation with photovoltaic research as well as equally interesting photophysics.

One of the most studied 2D perovskites are those with the Ruddlesden-Popper (RP) phase,⁷⁹ which have an offset between the BX_6 octahedra layers and have two monovalent large cations per interlayer (Figure 1.9). The general formula for the pure 2D composition is given by R_2BX_4 where R is a larger monovalent cation, most commonly organic for LHPs. An alternative phase is the Dion-Jacobson (DJ), where divalent cations are

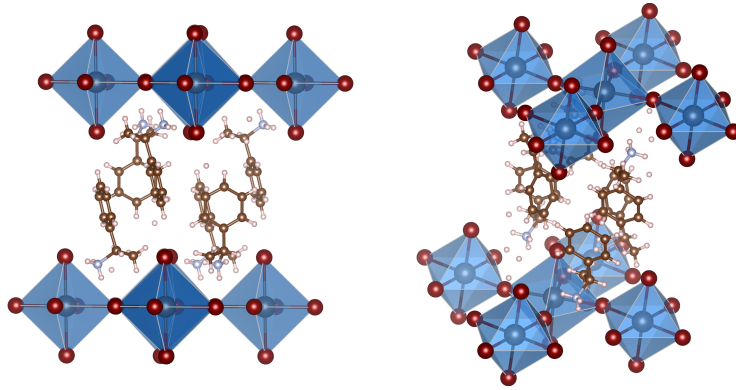


Figure 1.9: Crystal structure³⁶ of PEA_2PbI_4 ,⁷⁸ where PEA stands for the phenethylammonium cation, a Ruddlesden-Popper 2D perovskite. PbI_6 octahedra form layers separated by the low dielectric organic cations producing quantum and dielectric confinement.

used and the layers are aligned.⁸⁰ Focusing on the RP 2D perovskites, simply 2D herein, intermediate phases between 3D and 2D can be made with a mixture of small (A) and large (R) cations. These are known as quasi-2D and their composition is described by the formula $\text{R}_2\text{A}_{n-1}\text{B}_n\text{X}_{3n+1}$, where n is the number of layers between spacers.⁸¹ The 2D perovskite electronic structure suffers a considerable quantum confinement with a blue-shift of the band-gap. As n increases, for the quasi-2D compositions, the properties become closer to the 3D case.

While enhanced stability is one of the key properties that introduced 2D perovskite to the recent LHP research surge, there are other properties and applications worth mentioning. 2D perovskites are naturally ordered into a structure of barriers and quantum wells (QW), much like other well studied artificial structures such as AlGaAs/GaAs QW systems.⁸² Therefore, strong confinement effects are to be expected. On the one hand, quantum confinement reduces the bandgap and diminishes the space for electrons and holes, increasing the interaction. On the other hand, there is an additional dielectric confinement where, unlike in a 3D lattice, the low permittivity of the organic spacer screens poorly the electron-hole correlations and pushes further the exciton binding energy to values in the hundreds of meV. In fact, variations in the organic spacer, and thus its permittivity, can bring changes in the binding energy.^{29,83,84} All of these point to a clear prevalence of excitons as the photoexcited species in 2D perovskites,

contrary to their 3D counterparts, where charge carriers are the norm.⁴³ This makes them attractive for applications exploiting their excitonic character. First of all, 2D perovskites may constitute an easy to synthesize model system for the study of strongly bound excitons and the effects of dielectric confinement. In addition, other applications such as light emitting diodes⁸⁵ or even field effect transistors⁸⁶ are being explored.⁸¹ Certainly, for solar cell applications, a free carrier character is preferable, which is why most studies have focused on exploiting quasi-2D systems of at least $n = 3$, showing improved stability while maintaining decent carrier mobilities and extraction.^{67,87,88}

References

- (1) Kittel, C., *Introduction to Solid State Physics*, 5th; John Wiley & Sons, Inc.: 1976.
- (2) Pankove, J. I., *Optical Processes in Semiconductors*, 1st ed.; Dover Publications, Inc.: New York, 1975.
- (3) De Wolf, S.; Holovsky, J.; Moon, S.-J.; Löper, P.; Niesen, B.; Ledinsky, M.; Haug, F.-J.; Yum, J.-H.; Ballif, C. Organometallic Halide Perovskites: Sharp Optical Absorption Edge and Its Relation to Photovoltaic Performance. *J. Phys. Chem. Lett.* **2014**, *5*, 1035–1039.
- (4) Shockley, W.; Read Jr, W. T. Statistics of the Recombinations of Holes and Electrons. *Phys. Rev.* **1952**, *87*, 835.
- (5) Hall, R. N. Electron-Hole Recombination in Germanium. *Phys. Rev.* **1952**, *87*, 387–387.
- (6) Bube, R. H., *Photoconductivity of solids*. New York, 1960.
- (7) Beard, M. C.; Turner, G. M.; Schmuttenmaer, C. A. Transient Photoconductivity in GaAs as Measured by Time-Resolved Terahertz Spectroscopy. *Phys. Rev. B* **2000**, *62*, 15764–15777.
- (8) Coleman, P. In *Handbook of Magnetism and Advanced Magnetic Materials*; American Cancer Society: 2007.
- (9) Kayanuma, Y. Quantum-Size Effects of Interacting Electrons and Holes in Semiconductor Microcrystals with Spherical Shape. *Phys. Rev. B* **1988**, *38*, 9797–9805.
- (10) Hangleiter, A. Nonradiative Recombination Via Deep Impurity Levels in Semiconductors: The Excitonic Auger Mechanism. *Phys. Rev. B* **1988**, *37*, 2594–2604.
- (11) Szmytkowski, J. A Simple Model of the Trap-Assisted Recombination with the Excitonic Auger Mechanism. *Eur. Phys. J. Plus* **2020**, *135*, 37.
- (12) Soavi, G.; Conte, S. D.; Manzoni, C.; Viola, D.; Narita, A.; Hu, Y.; Feng, X.; Hohenester, U.; Molinari, E.; Prezzi, D.; Müllen, K.; Cerullo, G. Exciton–Exciton Annihilation and Biexciton Stimulated Emission in Graphene Nanoribbons. *Nat. Commun.* **2016**, *7*, 11010.
- (13) Özçelik, S.; Akins, D. L. Nature of Exciton–Exciton Annihilation in an Aggregated Cyanine Dye. *J. Phys. Chem. B* **1997**, *101*, 3021–3024.

-
- (14) Delport, G.; Chehade, G.; Lédée, F.; Diab, H.; Milesi-Brault, C.; Trippé-Allard, G.; Even, J.; Lauret, J.-S.; Deleporte, E.; Garrot, D. Exciton-Exciton Annihilation in Two-Dimensional Halide Perovskites at Room Temperature. *J. Phys. Chem. Lett.* **2019**, *10*, 5153–5159.
- (15) Chmeliov, J.; Narkeliunas, J.; Graham, M. W.; Fleming, G. R.; Valkunas, L. Exciton-Exciton Annihilation and Relaxation Pathways in Semiconducting Carbon Nanotubes. *Nanoscale* **2016**, *8*, 1618–1626.
- (16) Devreese, J. T. Polarons. *arXiv:cond-mat/0004497* **2000**.
- (17) Landau, L. D. Über Die Bewegung Der Elektronen in Kristallgitter. *Phys. Z. Sowjetunion* **1933**, *3*, 644–645.
- (18) Pekar, S. I., *Issledovaniya po Elektronnoj Teorii Kristallov*; Gostekhizdat: Moskva, 1951.
- (19) Fröhlich, H. Electrons in Lattice Fields. *Adv. Phys.* **1954**, *3*, 325–361.
- (20) Evrard, R. On the Excited States of the Polaron. *Phys. Lett.* **1965**, *14*, 295–296.
- (21) Feynman, R. P. Slow Electrons in a Polar Crystal. *Phys. Rev.* **1955**, *97*, 660–665.
- (22) Jeevanandam, J.; Barhoum, A.; Chan, Y. S.; Dufresne, A.; Danquah, M. K. Review on Nanoparticles and Nanostructured Materials: History, Sources, Toxicity and Regulations. *Beilstein J. Nanotechnol.* **2018**, *9*, 1050–1074.
- (23) Roduner, E. Size Matters: Why Nanomaterials Are Different. *Chem. Soc. Rev.* **2006**, *35*, 583–592.
- (24) Forstmann, F. The Concepts of Surface States. *Prog. Surf. Sci.* **1993**, *42*, 21–31.
- (25) Veamatahau, A.; Jiang, B.; Seifert, T.; Makuta, S.; Latham, K.; Kanehara, M.; Teranishi, T.; Tachibana, Y. Origin of Surface Trap States in Cds Quantum Dots: Relationship Between Size Dependent Photoluminescence and Sulfur Vacancy Trap States. *Phys. Chem. Chem. Phys.* **2014**, *17*, 2850–2858.
- (26) Leonid Gurevich; Luca Canali; Leo P. Kouwenhoven In *Quantum Confinement VI: Nanostructured Materials and Devices : Proceedings of the International Symposium*, M. Cahay, S. Bandyopadhyay, J. P. Leburton, J. S. Harris, D. J. Lockwood, Eds.; The Electrochemical Society: Pennington, New Jersey, 2001; Vol. 19.
- (27) Alivisatos, A. P. Semiconductor Clusters, Nanocrystals, and Quantum Dots. *Science* **1996**, *271*, 933–937.

-
- (28) Ishihara, T.; Hong, X.; Ding, J.; Nurmikko, A. V. Dielectric Confinement Effect for Exciton and Biexciton States in PbI_4 -Based Two-Dimensional Semiconductor Structures. *Surf. Sci.* **1992**, *267*, 323–326.
- (29) Hong, X.; Ishihara, T.; Nurmikko, A. V. Dielectric Confinement Effect on Excitons in PbI_4 -Based Layered Semiconductors. *Phys. Rev. B* **1992**, *45*, 6961–6964.
- (30) Jung, H. S.; Park, N.-G. Perovskite Solar Cells: From Materials to Devices. *Small* **2015**, *11*, 10–25.
- (31) Green, M. A.; Ho-Baillie, A.; Snaith, H. J. The Emergence of Perovskite Solar Cells. *Nat. Photonics* **2014**, *8*, 506–514.
- (32) Stranks, S. D.; Snaith, H. J. Metal-Halide Perovskites for Photovoltaic and Light-Emitting Devices. *Nat. Nanotechnol.* **2015**, *10*, 391–402.
- (33) Grätzel, M. The Light and Shade of Perovskite Solar Cells. *Nat. Mater.* **2014**, *13*, 838–842.
- (34) Liu, X.; Liebermann, R. C. X-Ray Powder Diffraction Study of CaTiO_3 Perovskite at High Temperatures. *Phys. Chem. Minerals* **1993**, *20*, 171–175.
- (35) Da Como, E.; De Angelis, F.; Snaith, H.; Walker, A., *Unconventional Thin Film Photovoltaics*; Energy & Environment; The Royal Society of Chemistry: Cambridge, 2016.
- (36) Momma, K.; Izumi, F. Vesta 3 for Three-Dimensional Visualization of Crystal, Volumetric and Morphology Data. *J. Appl. Cryst.* **2011**, *44*, 1272–1276.
- (37) Best Research-Cell Efficiency Chart, Photovoltaic Research, NREL., <https://www.nrel.gov/pv/cell-efficiency.html> (accessed 11/18/2019).
- (38) Kojima, A.; Teshima, K.; Shirai, Y.; Miyasaka, T. Organometal Halide Perovskites as Visible-Light Sensitizers for Photovoltaic Cells. *J. Am. Chem. Soc.* **2009**, *131*, 6050–6051.
- (39) Im, J.-H.; Lee, C.-R.; Lee, J.-W.; Park, S.-W.; Park, N.-G. 6.5% Efficient Perovskite Quantum-Dot-Sensitized Solar Cell. *Nanoscale* **2011**, *3*, 4088–4093.
- (40) Kim, H.-S.; Lee, C.-R.; Im, J.-H.; Lee, K.-B.; Moehl, T.; Marchioro, A.; Moon, S.-J.; Humphry-Baker, R.; Yum, J.-H.; Moser, J. E.; Grätzel, M.; Park, N.-G. Lead Iodide Perovskite Sensitized All-Solid-State Submicron Thin Film Mesoscopic Solar Cell with Efficiency Exceeding 9%. *Sci. Rep.* **2012**, *2*, 591.

- (41) Lee, M. M.; Teuscher, J.; Miyasaka, T.; Murakami, T. N.; Snaith, H. J. Efficient Hybrid Solar Cells Based on Meso-Superstructured Organometal Halide Perovskites. *Science* **2012**, *338*, 640–643.
- (42) Saliba, M.; Correa-Baena, J.-P.; Grätzel, M.; Hagfeldt, A.; Abate, A. Perovskite Solar Cells: From the Atomic Level to Film Quality and Device Performance. *Angew. Chem. Int. Ed.* **2018**, *57*, 2554–2569.
- (43) Herz, L. M. Charge-Carrier Dynamics in Organic-Inorganic Metal Halide Perovskites. *Annu. Rev. Phys. Chem.* **2016**, *67*, 65–89.
- (44) Tanaka, K.; Takahashi, T.; Ban, T.; Kondo, T.; Uchida, K.; Miura, N. Comparative Study on the Excitons in Lead-Halide-Based Perovskite-Type Crystals $\text{CH}_3\text{NH}_3\text{PbBr}_3$ $\text{CH}_3\text{NH}_3\text{PbI}_3$. *Solid State Commun.* **2003**, *127*, 619–623.
- (45) Saliba, M.; Matsui, T.; Domanski, K.; Seo, J.-Y.; Ummadisingu, A.; Zakeeruddin, S. M.; Correa-Baena, J.-P.; Tress, W. R.; Abate, A.; Hagfeldt, A.; Grätzel, M. Incorporation of Rubidium Cations into Perovskite Solar Cells Improves Photovoltaic Performance. *Science* **2016**, *354*, 206–209.
- (46) Snaith, H. J. Present Status and Future Prospects of Perovskite Photovoltaics. *Nat. Mater.* **2018**, *17*, 372–376.
- (47) Wehrenfennig, C.; Eperon, G. E.; Johnston, M. B.; Snaith, H. J.; Herz, L. M. High Charge Carrier Mobilities and Lifetimes in Organolead Trihalide Perovskites. *Adv. Mater.* **2014**, *26*, 1584–1589.
- (48) Herz, L. M. Charge-Carrier Mobilities in Metal Halide Perovskites: Fundamental Mechanisms and Limits. *ACS Energy Lett.* **2017**, 1539–1548.
- (49) Bi, Y.; Hutter, E. M.; Fang, Y.; Dong, Q.; Huang, J.; Savenije, T. J. Charge Carrier Lifetimes Exceeding 15 μs in Methylammonium Lead Iodide Single Crystals. *J. Phys. Chem. Lett.* **2016**, *7*, 923–928.
- (50) Stranks, S. D.; Eperon, G. E.; Grancini, G.; Menelaou, C.; Alcocer, M. J. P.; Leijtens, T.; Herz, L. M.; Petrozza, A.; Snaith, H. J. Electron-Hole Diffusion Lengths Exceeding 1 Micrometer in an Organometal Trihalide Perovskite Absorber. *Science* **2013**, *342*, 341–344.

-
- (51) Niesner, D.; Wilhelm, M.; Levchuk, I.; Osvet, A.; Shrestha, S.; Batentschuk, M.; Brabec, C.; Fauster, T. Giant Rashba Splitting in $\text{CH}_3\text{NH}_3\text{PbBr}_3$ Organic-Inorganic Perovskite. *Phys. Rev. Lett.* **2016**, *117*, 126401.
- (52) Etienne, T.; Mosconi, E.; De Angelis, F. Dynamical Origin of the Rashba Effect in Organohalide Lead Perovskites: A Key to Suppressed Carrier Recombination in Perovskite Solar Cells? *J. Phys. Chem. Lett.* **2016**, *7*, 1638–1645.
- (53) Zhu, X.-Y.; Podzorov, V. Charge Carriers in Hybrid Organic–Inorganic Lead Halide Perovskites Might Be Protected as Large Polarons. *J. Phys. Chem. Lett.* **2015**, *6*, 4758–4761.
- (54) Miyata, K.; Meggiolaro, D.; Trinh, M. T.; Joshi, P. P.; Mosconi, E.; Jones, S. C.; Angelis, F. D.; Zhu, X.-Y. Large Polarons in Lead Halide Perovskites. *Sci. Adv.* **2017**, *3*, e1701217.
- (55) Joshi, P. P.; Maehrlein, S. F.; Zhu, X. Dynamic Screening and Slow Cooling of Hot Carriers in Lead Halide Perovskites. *Adv. Mater.* **2019**, 1803054.
- (56) Maiti, A.; Khatun, S.; Pal, A. J. Rashba Band Splitting in $\text{CH}_3\text{NH}_3\text{PbI}_3$: An Insight from Spin-Polarized Scanning Tunneling Spectroscopy. *Nano Lett.* **2020**, *20*, 292–299.
- (57) Zheng, F.; Tan, L. Z.; Liu, S.; Rappe, A. M. Rashba Spin–Orbit Coupling Enhanced Carrier Lifetime in $\text{CH}_3\text{NH}_3\text{PbI}_3$. *Nano Lett.* **2015**, *15*, 7794–7800.
- (58) Karakus, M.; Jensen, S. A.; D’Angelo, F.; Turchinovich, D.; Bonn, M.; Cánovas, E. Phonon–Electron Scattering Limits Free Charge Mobility in Methylammonium Lead Iodide Perovskites. *J. Phys. Chem. Lett.* **2015**, *6*, 4991–4996.
- (59) Bretschneider, S. A.; Ivanov, I.; Wang, H. I.; Miyata, K.; Zhu, X.; Bonn, M. Quantifying Polaron Formation and Charge Carrier Cooling in Lead-Iodide Perovskites. *Adv. Mater.* **2018**, 1707312.
- (60) Frost, J. M.; Whalley, L. D.; Walsh, A. Slow Cooling of Hot Polarons in Halide Perovskite Solar Cells. *ACS Energy Lett.* **2017**, *2*, 2647–2652.
- (61) Fu, J.; Xu, Q.; Han, G.; Wu, B.; Huan, C. H. A.; Leek, M. L.; Sum, T. C. Hot Carrier Cooling Mechanisms in Halide Perovskites. *Nat. Commun.* **2017**, *8*, 1300.

- (62) Yang, Y.; Ostrowski, D. P.; France, R. M.; Zhu, K.; van de Lagemaat, J.; Luther, J. M.; Beard, M. C. Observation of a Hot-Phonon Bottleneck in Lead-Iodide Perovskites. *Nat. Photonics* **2016**, *10*, 53–59.
- (63) Yang, J. et al. Acoustic-optical phonon up-conversion and hot-phonon bottleneck in lead-halide perovskites. *Nat. Commun.* **2017**, *8*, DOI: 10.1038/ncomms14120.
- (64) Yang, J.; Siempelkamp, B. D.; Liu, D.; Kelly, T. L. Investigation of CH₃NH₃PbI₃ Degradation Rates and Mechanisms in Controlled Humidity Environments Using in Situ Techniques. *ACS Nano* **2015**, *9*, 1955–1963.
- (65) Hieulle, J.; Wang, X.; Stecker, C.; Son, D.-Y.; Qiu, L.; Ohmann, R.; Ono, L. K.; Mugarza, A.; Yan, Y.; Qi, Y. Unraveling the Impact of Halide Mixing on Perovskite Stability. *J. Am. Chem. Soc.* **2019**, *141*, 3515–3523.
- (66) Xiao, X.; Dai, J.; Fang, Y.; Zhao, J.; Zheng, X.; Tang, S.; Rudd, P. N.; Zeng, X. C.; Huang, J. Suppressed Ion Migration Along the in-Plane Direction in Layered Perovskites. *ACS Energy Lett.* **2018**, *3*, 684–688.
- (67) Smith, I. C.; Hoke, E. T.; Solis-Ibarra, D.; McGehee, M. D.; Karunadasa, H. I. A Layered Hybrid Perovskite Solar-Cell Absorber with Enhanced Moisture Stability. *Angew. Chem.* **2014**, *126*, 11414–11417.
- (68) Gangadharan, D. T.; Ma, D. Searching for Stability at Lower Dimensions: Current Trends and Future Prospects of Layered Perovskite Solar Cells. *Energy Environ. Sci.* **2019**, *12*, 2860–2889.
- (69) Lu, J.; Jiang, L.; Li, W.; Li, F.; Pai, N. K.; Scully, A. D.; Tsai, C.-M.; Bach, U.; Simonov, A. N.; Cheng, Y.-B.; Spiccia, L. Diammonium and Monoammonium Mixed-Organic-Cation Perovskites for High Performance Solar Cells with Improved Stability. *Adv. Energy Mater.* **2017**, *7*, 1700444.
- (70) Ye, J.; Zheng, H.; Zhu, L.; Liu, G.; Zhang, X.; Hayat, T.; Pan, X.; Dai, S. Enhanced Moisture Stability of Perovskite Solar Cells With Mixed-Dimensional and Mixed-Compositional Light-Absorbing Materials. *Solar RRL* **2017**, *1*, 1700125.
- (71) Goldschmidt, V. M. Die Gesetze der Krystallochemie. *Naturwissenschaften* **1926**, *14*, 477–485.
- (72) Saparov, B.; Mitzi, D. B. Organic–Inorganic Perovskites: Structural Versatility for Functional Materials Design. *Chem. Rev.* **2016**, *116*, 4558–4596.

- (73) Stoumpos, C. C.; Cao, D. H.; Clark, D. J.; Young, J.; Rondinelli, J. M.; Jang, J. I.; Hupp, J. T.; Kanatzidis, M. G. Ruddlesden–Popper Hybrid Lead Iodide Perovskite 2D Homologous Semiconductors. *Chem. Mater.* **2016**, *28*, 2852–2867.
- (74) Yuan, Z.; Zhou, C.; Tian, Y.; Shu, Y.; Messier, J.; Wang, J. C.; van de Burgt, L. J.; Kountouriotis, K.; Xin, Y.; Holt, E.; Schanze, K.; Clark, R.; Siegrist, T.; Ma, B. One-Dimensional Organic Lead Halide Perovskites with Efficient Bluish White-Light Emission. *Nat. Commun.* **2017**, *8*, 1–7.
- (75) Cha, J.-H.; Han, J. H.; Yin, W.; Park, C.; Park, Y.; Ahn, T. K.; Cho, J. H.; Jung, D.-Y. Photoresponse of CsPbBr₃ and Cs₄PbBr₆ Perovskite Single Crystals. *J. Phys. Chem. Lett.* **2017**, *8*, 565–570.
- (76) Protesescu, L.; Yakunin, S.; Bodnarchuk, M. I.; Krieg, F.; Caputo, R.; Hendon, C. H.; Yang, R. X.; Walsh, A.; Kovalenko, M. V. Nanocrystals of Cesium Lead Halide Perovskites (CsPbX₃, X = Cl, Br, and I): Novel Optoelectronic Materials Showing Bright Emission with Wide Color Gamut. *Nano Lett.* **2015**, *15*, 3692–3696.
- (77) Vale, B. R. C.; Socie, E.; Burgos-Caminal, A.; Bettini, J.; Schiavon, M. A.; Moser, J.-E. Exciton, Biexciton, and Hot Exciton Dynamics in CsPbBr₃ Colloidal Nanoplatelets. *J. Phys. Chem. Lett.* **2019**, 387–394.
- (78) Billing, D. G. Bis(1-phenylethylammonium) Tetraiodoplumbate(II). *Acta Cryst. E* **2002**, *58*, m669–m671.
- (79) Ruddlesden, S. N.; Popper, P. New Compounds of the K₂NiF₄ Type. *Acta Cryst.* **1957**, *10*, 538–539.
- (80) Mao, L.; Ke, W.; Pedesseau, L.; Wu, Y.; Katan, C.; Even, J.; Wasielewski, M. R.; Stoumpos, C. C.; Kanatzidis, M. G. Hybrid Dion–Jacobson 2D Lead Iodide Perovskites. *J. Am. Chem. Soc.* **2018**, *140*, 3775–3783.
- (81) Chen, Y.; Sun, Y.; Peng, J.; Tang, J.; Zheng, K.; Liang, Z. 2D Ruddlesden–Popper Perovskites for Optoelectronics. *Adv. Mater.* **2018**, *30*, 1703487.
- (82) Lin, C.-F.; Lee, B.-L. Extremely broadband AlGaAs/GaAs superluminescent diodes. *Appl. Phys. Lett.* **1997**, *71*, 1598–1600.

- (83) Chernikov, A.; Berkelbach, T. C.; Hill, H. M.; Rigosi, A.; Li, Y.; Aslan, O. B.; Reichman, D. R.; Hybertsen, M. S.; Heinz, T. F. Exciton Binding Energy and Nonhydrogenic Rydberg Series in Monolayer WS₂. *Phys. Rev. Lett.* **2014**, *113*, 076802.
- (84) Chen, P.; Bai, Y.; Lyu, M.; Yun, J.-H.; Hao, M.; Wang, L. Progress and Perspective in Low-Dimensional Metal Halide Perovskites for Optoelectronic Applications. *Solar RRL* **2018**, *2*, 1700186.
- (85) Liang, D.; Peng, Y.; Fu, Y.; Shearer, M. J.; Zhang, J.; Zhai, J.; Zhang, Y.; Hamers, R. J.; Andrew, T. L.; Jin, S. Color-Pure Violet-Light-Emitting Diodes Based on Layered Lead Halide Perovskite Nanoplates. *ACS Nano* **2016**, *10*, 6897–6904.
- (86) Matsushima, T.; Hwang, S.; Sandanayaka, A. S. D.; Qin, C.; Terakawa, S.; Fujihara, T.; Yahiro, M.; Adachi, C. Solution-Processed Organic–Inorganic Perovskite Field-Effect Transistors with High Hole Mobilities. *Adv. Mater.* **2016**, *28*, 10275–10281.
- (87) Tsai, H. et al. High-Efficiency Two-Dimensional Ruddlesden–Popper Perovskite Solar Cells. *Nature* **2016**, *536*, 312–316.
- (88) Quan, L. N.; Yuan, M.; Comin, R.; Voznyy, O.; Beauregard, E. M.; Hoogland, S.; Buin, A.; Kirmani, A. R.; Zhao, K.; Amassian, A.; Kim, D. H.; Sargent, E. H. Ligand-Stabilized Reduced-Dimensionality Perovskites. *J. Am. Chem. Soc.* **2016**, *138*, 2649–2655.

Chapter 2

Spectroscopic techniques

This chapter serves as an in-depth description of the ultra-broadband time-resolved terahertz spectroscopy setup built during this thesis. It describes the principles of THz generation and detection using gas photonics as well as the data acquisition and treatment processes. Lastly, it gives an overview of the other time-resolved techniques employed in this work.

2.1 THz spectroscopy

2.1.1 Introduction

THz stands for the frequency range in the far infrared, *i. e.*, with frequencies typically in the 0.1 to 10 THz range. This constitutes the “THz gap”, referring to the classical difficulty in accessing this part of the electromagnetic spectrum. It is situated between the electronically available microwave and the optical infrared and visible radiations.

The use of THz radiation includes many potential applications including space exploration, plasma fusion diagnostics, industrial characterization, communications, radar scaled scattering simulation, medical diagnosis, imaging and, certainly, spectroscopy of materials as well as chemical and biological systems. One of the key advantages of THz waves relies upon the different absorptive responses coming from different materials. While water or metals are completely opaque, insulators such as plastics or semiconductors can be fully transparent. Furthermore, many materials show unique spectral signatures that can be used to identify them. This can have relevant applications from security imaging to industrial quality control.¹ Nonetheless, it is on the spectroscopic applications where this text will focus, due to its importance in the study of optoelectronic materials. THz radiation is sensitive to low energy transitions in molecules and materials in all phases. In solid semiconductors it is especially useful for the characterization of charge carrier dynamics. Additionally, it is sensitive to other resonant behavior such as vibrations, intra-excitonic transitions and plasmon resonances.²

When it comes to THz ultrafast spectroscopy, two names are commonly found: THz time-domain spectroscopy (TDS) and time resolved THz spectroscopy (TRTS). The former typically refers to the recording of THz spectra through the Fourier transform of a waveform while the latter is used when pump-probe experiments are involved, thus showing a “time-resolved” evolution. The two terms can sometimes be used interchangeably.

2.1.2 Classical time-resolved THz technologies

Although THz radiation can be obtained from different sources, including synchrotrons and free-electron lasers, we are going to focus on the utilization of fs lasers for the gen-

eration and detection of ultrafast THz pulses.

THz generation (and detection) can be explained using Maxwell's equations for the interaction of electromagnetic waves and matter

$$\nabla \times E = -\frac{\partial B}{\partial t}, \quad (2.1)$$

$$\nabla \times H = J + \frac{\partial D}{\partial t}, \quad (2.2)$$

where E and H are the electric and magnetic fields, while B is the magnetic flux, J the current and D the electric displacement. These equations can be expanded into

$$\nabla \times E = \frac{\partial \mu H}{\partial t}, \quad (2.3)$$

$$\nabla \times H = \sigma E + \frac{\partial \varepsilon E}{\partial t}, \quad (2.4)$$

where μ is the magnetic permeability, σ is the conductivity and ε is the permittivity. In addition, it is important to note the relationship between D and the dielectric polarization P , where $D = \varepsilon_0 E + P$, ε_0 being the vacuum permittivity. This is given by the relation between electric susceptibility χ_e and the relative permittivity ($\chi_e = \varepsilon_r - 1$). Therefore, $P = \varepsilon_0 \chi_e E$.

As will be presented in the following sections, the generation of THz waves will arise from the transient changes of either J , through a change in σ , or P , through non-linearities involving χ_e .

2.1.2.1 Photoconductive antennas

Briefly, this method exploits the transient changes in σ upon ultrafast excitation of a semiconductor generating free carriers. This semiconductor is submitted to an electric field which accelerates the carriers producing a current $J(t)$. This is a transient current, as it builds up a polarization that opposes the electric field when electrons and holes become increasingly separated. It is the transient nature of $J(t)$ which produces the emission of THz, similarly to how an alternating current in an antenna produces radio waves. Likewise, in the THz detection using antennas, an ultrafast gating pulse is used to generate free carriers between two electrodes that decay in 1 ps or less. Instead of applying a DC bias, the incoming THz field is the one accelerating the carriers and

producing a measurable current. This current can therefore be directly related to the magnitude and sign of the passing THz field at the moment of the gate arrival. The response time of the semiconductor has to be short compared to the changes in THz electric field in order to obtain accurate measurements.^{3,4}

2.1.2.2 Optical rectification and electro-optic sampling

The second, and most commonly encountered, method is based on the use of non-linear crystals. Optical rectification is a second order non-linear process occurring in crystals when an intense laser beam propagates through them under certain conditions. The process can be understood by describing the electric field dependence of $\chi_e(E)$ with the electric field. At high field the non-linear properties can be described as a Taylor expansion of the scalar relationships

$$P = \varepsilon_0 \chi_e(E) E = \varepsilon_0 (\chi_{e1} + \chi_{e2} E + \chi_{e3} E^2 + \dots) E. \quad (2.5)$$

The second order non-linear effects appear from the corresponding polarization term $P_2^{nl} = \varepsilon_0 \chi_{e2} E^2$. If we consider monochromatic light, we can obtain

$$P_2^{nl} = \varepsilon_0 \chi_{e2} E^2 = \varepsilon_0 \chi_{e2} E_0^2 \cos(\omega t)^2 = \frac{1}{2} \varepsilon_0 \chi_{e2} E_0^2 (1 + \cos(2\omega t)). \quad (2.6)$$

There are two clear terms, a DC polarization (1) and a second harmonic generation ($\cos(2\omega t)$). However, this alone does not explain the generation of THz radiation. For that we need to consider what happens when using short fs pulses. Due to the Fourier transform relationship and the Heisenberg uncertainty principle, fs pulses are somewhat broadband in the frequency domain and are formed by many different frequencies with small differences between them. We can simplify that by considering the second order polarization obtained with two frequencies ω_1 and ω_2 .

$$\begin{aligned} P_2^{nl} &= \varepsilon_0 \chi_{e2} E_1 E_2 = \varepsilon_0 \chi_{e2} E_0^2 \cos(\omega_1 t) \cos(\omega_2 t) \\ &= \frac{1}{2} \varepsilon_0 \chi_{e2} E_0^2 (\cos((\omega_1 - \omega_2)t) + \cos((\omega_1 + \omega_2)t)). \end{aligned} \quad (2.7)$$

This shows two new second order phenomena named sum and difference frequency generation. If the two frequencies are very close, such as in a fs pulse, the second term can be approximated to the second harmonic generation while the first term produces a low energy radiation that lies in the THz range. The shorter the fundamental pulses the

more frequencies are used and a broader THz pulse can be obtained. Sub-10 fs pulses can give very broadband pulses going up to 100 THz.⁵ Electro-optic sampling is based on the same second order polarization. Without going into detail, the presence of the THz electric field changes the polarization of a gate pulse that copropagates through the crystal. This change in polarization can be directly related to the THz electric field magnitude and sign in order to obtain the complete waveform. The most common crystals for both generation and detection are ZnTe, GaP and GaSe but other materials such as LiNbO₃, LiTaO₃, or organics like 4-N,N-dimethylamino-4'-N-methylstilbazolium tosylate (DAST) have also been used. These methods allow one to obtain strong and stable THz pulses with good signal to noise, but are generally limited in bandwidth because of phonon resonances and coherence lengths. The accessible range depends on the crystal but the most common ZnTe typically gives access to the 0.5 to 3 THz range.

2.1.3 Ultra-broadband THz pulses through gas photonics

In order to obtain short and broadband THz pulses using standard fs lasers with pulses in the order of several tens of fs it is best to avoid the use of crystals or antennas that can limit the bandwidth through different mechanisms. In the past two decades, a method of generating and detecting broadband pulses has been developed. Starting from the first results in the year 2000⁶ it is now possible to build a setup with broadband capabilities without the need for extremely short pulses, that produces spectrally clean results with a high time-resolution. The following section details the mechanisms by which broadband THz pulses are obtained and detected in the work presented in this thesis. Setup development has been a key part and many improvements have been implemented over the years from the different results found in the literature. We will also try to give a description of the particularities and problems that have to be taken into account in order to build such a functioning setup.

2.1.3.1 THz generation through a two color plasma

THz generation through two color plasmas was initially thought as a four-wave mixing (FWM) process,⁶ a third order (χ_{e3}) process through which a third frequency ω_3 can be obtained from two different frequencies ω_1 and ω_2 in the form $\omega_3 = 2\omega_1 - \omega_2$. If the two original frequencies are the fundamental of a laser and its second harmonic, the result is very similar to the optical rectification portrayed in the previous section,

generating a THz pulse. Since the generation occurs in a gas with no phonon resonances the bandwidth is only limited by the bandwidth (and length) of the original pulse.⁷ Although FWM serves as a good simple explanation it fails at explaining some of the observed phenomena. For example, THz generation requires the generation of a plasma and it increases as the plasma becomes stronger. In addition, it was found that the process was maximized at certain phase shifts between the two colors. Also, the actual origin of the χ_{e3} nonlinearity in a gas plasma was unclear. In order to explain the discrepancies, a transient current model was developed.⁸⁻¹⁰ In it, the THz emission comes from the formation of a net transient plasma current under an asymmetric laser field,

$$J = eN_e v_e, \quad (2.8)$$

where e , N_e and v_e are the electron charge, density and net velocity, respectively. In order to obtain a current surge that emits THz, a net drift velocity is needed. The drift velocity is the average velocity a particle had during a certain period of time. Furthermore, in order to produce a net current in a centrosymmetric system, such as gases or their plasmas, it is necessary to break the symmetry. In other words, it is necessary to obtain a net drift velocity for the generated electrons in a plasma. This is achieved by mixing the fundamental and the second harmonic of a pulsed laser beam considering their relative phase-shift. This can be shown from a semi-classical point of view with a small simulation. Parting from a simplified combination of a monochromatic fundamental (ω) and its second harmonic (2ω), the total electric field is given by the equation

$$E(t) = E_1 \cos(\omega t + \phi) + E_2 \cos(2(\omega t + \phi) + \theta). \quad (2.9)$$

Knowing that $\frac{dv(t)}{dt} = \frac{eE}{m_e}$ and considering that electrons appear after tunnel ionization with $v_0 = 0$, integration gives the velocity of electrons at a certain moment in time expressed as

$$v(t) = \frac{eE_1}{m_e\omega} (\sin(\omega t + \phi) - \sin(\phi)) + \frac{eE_2}{m_e 2\omega} (\sin(2(\omega t + \phi) + \theta) - \sin(2\phi + \theta)). \quad (2.10)$$

The drift velocity of an electron can now be calculated as the average velocity over one cycle with the operation

$$v_d = \frac{\int_0^{\frac{2\pi}{\omega}} v(t) dt}{\frac{2\pi}{\omega}}. \quad (2.11)$$

This yields

$$v_d = \frac{eE_1}{m_e\omega} \sin(\phi) + \frac{eE_2}{2m_e\omega} \sin(2\phi + \theta), \quad (2.12)$$

when multiplied by -1 for the sake of simplification. This simplified model, in which other aspects such as light polarization or spatial distribution are not considered, allows one to demonstrate the THz output efficiency dependence on the phase-shift θ between the two colors. A plot of the electric field E at the moment of ionization ($t = 0$) and the drift velocity, v_d , against phase ϕ is shown in Figure 2.1.

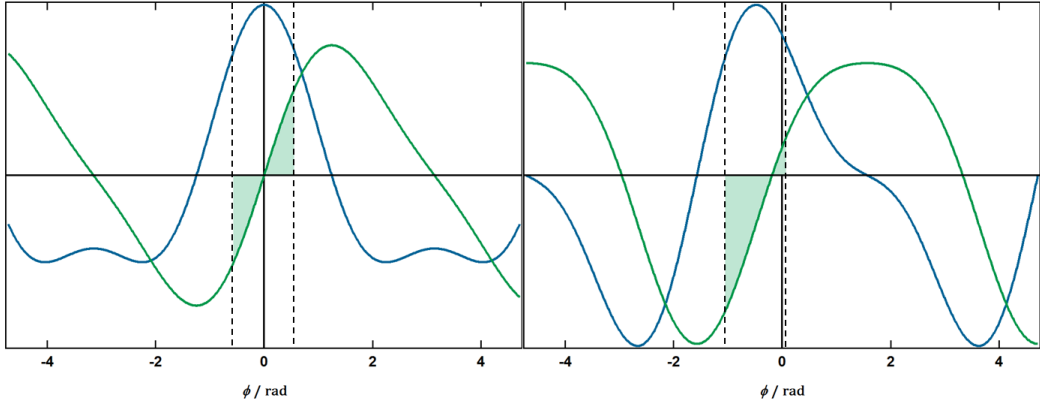


Figure 2.1: Laser electric field (Blue) and electron drift velocity (Green) simulation for $\theta = 0$ (Left) and $\theta = \pi/2$ (Right).

Clearly, when looking around the maximum laser electric field, where tunnel ionization is most likely to occur, there is a net drift velocity for $\theta = \pi/2$. On the contrary, for $\theta = 0$ it cancels out. In fact, $\theta = \pi/2$ is the optimum phase shift. It is worth noting that θ can be easily modified in experiments through the different phase velocity dispersion for the two wavelengths in air. Hence, different distances between the BBO crystal and the plasma should yield different THz generation intensities. Indeed, experiments show an oscillatory response of THz generation with distance (d) that can be extrapolated to zero for the $d = 0$ case. This means that for $\theta = 0$ the generation is negligible since for $d = 0$ both colored pulses are still in phase. Thus, experiments are in agreement with the transient current model while the polarization-based four-wave mixing model predicts a maximum conversion for in-phase pulses.^{8,9} Interestingly, when the phase shift does not optimize THz generation it optimizes third harmonic generation (3ω).^{8,10} In conclusion, the BBO-plasma distance is a critical parameter to be optimized.

Another parameter that should be taken into account is the polarization of the fundamental and the second harmonic. At phase matching conditions for optimum second harmonic generation (SHG), the polarization of the ω and 2ω resulting pulses is perpendicular. Thus, they interact poorly, yielding a negligible THz generation. Hence, the BBO angle is usually mismatched for optimum THz generation. The yield for such conditions is lower than what could be obtained with optimum SHG at equal polarization, as shown in the literature.¹¹⁻¹³ In order to attain such conditions an ultra-thin dual wavelength waveplate (DWP) can be used between the BBO and the plasma. As explained in reference [11] an ultra-thin DWP allows to obtain paralleled ω and 2ω pulses at optimum BBO phase matching conditions. In addition, the ultra-thin thickness minimizes the temporal dispersion assuring the overlap of the two pulses in time. It was reported that an enhancement of 1.4 in total THz generation is expected, which could be larger for longer pulses than the 20 fs ones reported in ref.[11] due to a better temporal overlap. In addition, this stabilizes the THz polarization, critical for its detection.^{11,12,14}

2.1.3.2 THz detection through air biased coherent detection

In order to detect broadband THz pulses it is imperative to avoid being limited by phonon resonances in crystals, such as the ones used in electro-optic sampling, or the carrier response, characteristic of photoconductive antennas. An ideal pathway is to rely again on the use of gas photonics. Such method has been developed in Prof. Zhang's group under the name of air biased coherent detection (ABCD).¹⁵

As first described in ref. [15], ABCD makes use of a third order non-linear process. Before adding any external bias, the interaction between the fundamental of a pulsed laser with frequency ω (the gating beam) with itself and a THz field, focused in a gas, generates second harmonics (2ω). This would be four-wave mixing for sum frequency generation, the opposite to the generation process, and it is typically known as THz field induced second harmonic generation (TFISHG).¹⁶ However, the 2ω photons are also generated as a white light generation process through self-phase modulation involving only the gating beam. In turn, the additionally generated 2ω can interact with the THz to modulate the total output. Let us consider simple linearly polarized laser fields in the same polarization plane to describe it in the following way:

The total 2ω electric field $E_{2\omega}$ depends on

$$E_{2\omega} \propto \chi_{e3} E_{THz} E_{\omega} E_{\omega} + E_{2\omega}^{WL}, \quad (2.13)$$

where E_{ω} is the electric field of the fundamental, $E_{2\omega}^{WL}$ is the 2ω electric field generated through white light generation in a plasma filament and E_{THz} is the electric field of the THz. The intensity that will be measured by a PMT ($I_{2\omega}$) is proportional to the square of the electric field, yielding

$$I_{2\omega} \propto (\chi_{e3} E_{THz} I_{\omega})^2 + I_{2\omega}^{WL} + 2\chi_{e3} E_{THz} I_{\omega} E_{2\omega}^{WL}, \quad (2.14)$$

where I is the intensity. Using a method of detection such as a lock-in amplifier or a shot to shot difference, chopping the THz pulses at 500 Hz while the gating beam stays at 1 kHz, the signal obtained follows the equation

$$\Delta I_{2\omega} \propto (\chi_{e3} E_{THz} I_{\omega})^2 + 2\chi_{e3} E_{THz} I_{\omega} E_{2\omega}^{WL}, \quad (2.15)$$

where only the terms containing E_{THz} are present in one of every two pulses. The first term in Equation 2.15 is incoherent, giving only information about the intensity of the THz. Moreover, if the gating beam intensity is high enough to produce a plasma and, thus, white light, the second term will arise and even be predominant. Furthermore, this term is coherent and gives information about the electric field of the THz, allowing one to obtain the complete waveform.¹⁷ However, a way to unequivocally measure the E_{THz} and not I_{THz} is needed. This is where the external bias field of the ABCD method comes into play. If we introduce an E_{Bias} term, we can obtain an additional 2ω component coming through a third order non-linear process, known as electric-field induced second harmonic generation (EFISHG)¹⁸ so that

$$E_{2\omega} \propto \chi_{e3} E_{THz} E_{\omega} E_{\omega} + \chi_{e3} E_{Bias} E_{\omega} E_{\omega} + E_{2\omega}^{WL}. \quad (2.16)$$

Following a similar development as before and going beyond what is explained in ref. [15] by combining it with ref. [17], we can consider the extra component of $E_{2\omega}$ coming from white light generation ($E_{2\omega}^{WL}$).

$$I_{2\omega} \propto (\chi_{e3} E_{THz} I_{\omega})^2 + (\chi_{e3} E_{Bias} I_{\omega})^2 + I_{2\omega}^{WL} + 2\chi_{e3} I_{\omega} E_{THz} E_{2\omega}^{WL} + 2(\chi_{e3} I_{\omega})^2 E_{THz} E_{Bias} + 2\chi_{e3} I_{\omega} E_{Bias} E_{2\omega}^{WL}. \quad (2.17)$$

Once again, using 500 Hz chopping on the THz beam and using a 1 kHz bias field the differential signal can be extracted yielding

$$\Delta I_{2\omega} \propto (\chi_{e3} E_{THz} I_{\omega})^2 + 2\chi_{e3} I_{\omega} E_{THz} E_{2\omega}^{WL} + 2(\chi_{e3} I_{\omega})^2 E_{THz} E_{Bias}. \quad (2.18)$$

The two first terms are the same as seen previously. The third one, however, is new, fully coherent and gives a stronger signal thanks to the E_{Bias} term. However, the incoherent $(\chi_{e3} E_{THz} I_{\omega})^2$ term is still present. Alternatively, as originally described in ref. [15], the THz beam can be maintained at 1 kHz and the bias field set to 500 Hz, giving opposite electric fields for each THz pulse. This yields the treated signal described by

$$\Delta I_{2\omega} \propto 4(\chi_{e3} I_{\omega})^2 E_{THz} E_{Bias} + 4\chi_{e3} I_{\omega} E_{Bias} E_{2\omega}^{WL}. \quad (2.19)$$

In this case, only one fully coherent term gives information about the THz field. In addition, this term is twice as big due to the opposing polarity of the bias field. A second term that does not depend on the THz field will also be present. This second term is constant and will constitute an offset on the signal unless a low enough power is used for the gating beam, removing the $E_{2\omega}^{WL}$ term. This is what N. Karpowicz *et al.* probably consider in ref. [15] for their treatment, obtaining only the first term. Nonetheless, this term is still important to explain some of the offsets that can be observed during the use of the setup.

When choosing between the two different signal extraction methods, one has to consider the advantages and disadvantages of each one. On the one hand, although the former method is more straightforward in its configuration and extrapolation to pump-probe experiments, it requires a high power of the gating beam to bury the incoherent term under the then more intense coherent terms. In turn, this introduces a bigger noise and a very strong $E_{2\omega}^{WL}$ signal that saturates the PMT. This translates into a lower signal-to-noise ratio for the former method. On the other hand, reducing the gating beam power makes the latter method much more advantageous. Indeed, the offset term (Equation 2.19) can be greatly reduced until it is insignificant while the signal is increased due to the factor 4 and the desaturation of the PMT. In addition, the noise is found to be lower, further increasing the signal-to-noise ratio. Careful control of the polarization, the BBO-plasma distance and the laser power for generation finally yields a 150 fs (FWHM) THz pulse ranging from 0.5 to 25 THz (Figure 2.2).

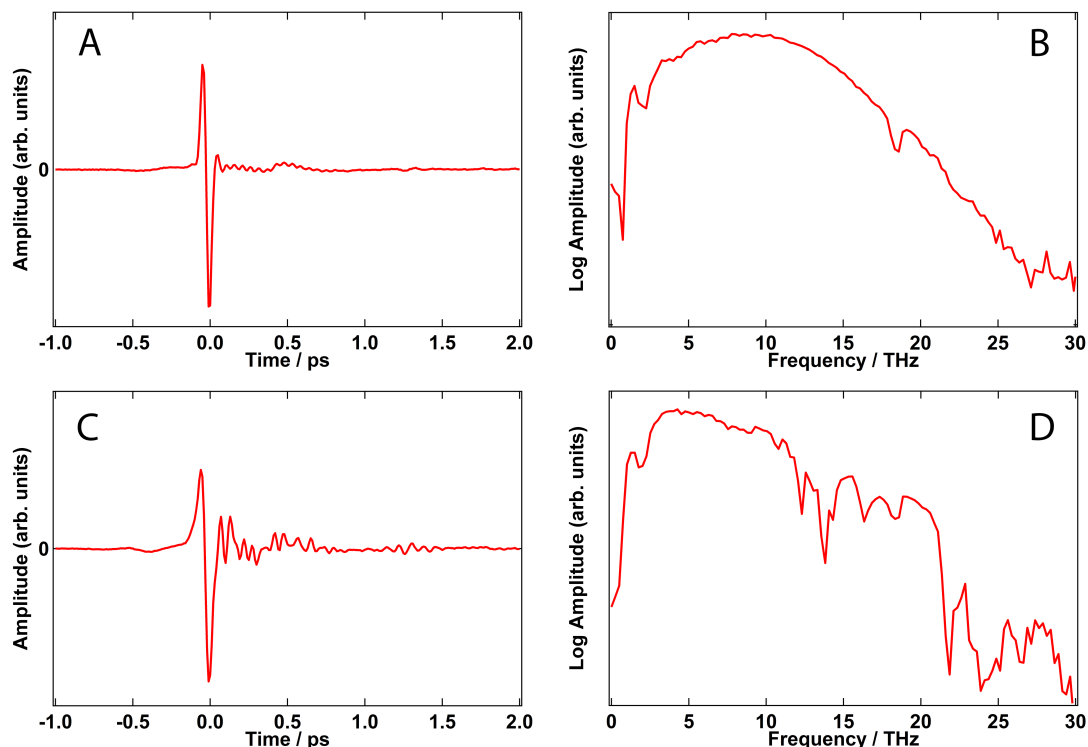


Figure 2.2: THz waveform (left) and spectrum (right) extracted through the 500 Hz bias method in N₂ (top) and butane (bottom) atmospheres.

An additional way of improving the signal-to-noise ratio is through the use of a gas with a higher non-linear susceptibility. As reported by X.-C. Zhang's group^{19,20} the use of gases, such as butane, with higher polarizability and, consequently, third order non-linear susceptibility, yields up to a two orders of magnitude increase in the $I_{2\omega}$ output. We developed a hermetically sealed box, containing the electrodes, where the detection process can be carried out with different gases at atmospheric pressure. Indeed, the use of butane allows to improve the signal-to-noise by 2 to 4 times. However, in order to carry out the detection, a window transparent to both the THz and the visible is needed. The best affordable material is polymethylpentene (TPXTM) which has several absorption bands starting from 12 THz (See Figure 2.2.D). This improved the pump-probe frequency-averaged dynamics measurements but introduced serious artifacts in the photoinduced spectra. Diamond would be an ideal material for the window as it shows a flat THz transmission. In fact, the implementation of a diamond window was

underway at the time of writing this text.

2.1.3.3 Pump-probe experiments

In a pump-probe experiment, the sample is excited with an optical pump pulse and probed in the THz. There are two intrinsic kinds of measurements that can be carried out in TRTS:

Waveform measurements scan the probe-gate delay in order to obtain the full THz waveform. The resulting data can be Fourier transformed to obtain the frequency resolved spectrum. Such measurements can be carried out without pump in order to obtain the complex refractive index of a material as is typically done in THz-TDS. Alternatively, a pump pulse can be used to obtain photoinduced spectra at a certain pump-probe delay. As will be shown in the data treatment section, it is preferable to scan the pump-probe and the probe-gate delays simultaneously. This ensures that all points of the waveform have experienced the same time interval with respect to the arrival of the pump.

Frequency-averaged time evolution measurements are carried out maintaining the probe-gate delay at a constant position, typically the maximum in E_{THz} . For these measurements to be trustworthy it is mandatory to have a flat frequency response, obtained from the waveform measurement, or, at least, to prove that the phase of the photoinduced response (ΔE) is not changing over time. Otherwise, waveform measurements at different pump-probe intervals are necessary to first understand the evolution of the signal.

Ideally, the complete information is obtained through the realization of 2D maps where a waveform is measured for each delay. These can be extremely costly in terms of time, as the gate-probe delay has to be scanned for every pump-probe delay. Nonetheless, they allow to better process and understand the data.^{21,22}

When measuring the effects of photoexcitation with TRTS, it is generally needed to obtain the dark THz field (E) and the photoexcited one (E_{ex}), the difference, ΔE , being the induced change. In classical spectrometers based on optical rectification and electro-optic sampling in ZnTe, it is common to measure E and ΔE separately.^{23,24} This is acceptable for long and stable pulses with fast scanning rates. However, when using

broadband pulses containing high frequencies it is mandatory to minimize any phase error from measuring these two quantities separately. Some approaches have been already used before for electro-optic sampling²⁵ and ABCD.²⁶ We developed a different approach taking advantage of our shot to shot acquisition card and the ability to choose the E_{bias} flipping frequency.

As is depicted in Figure 2.3, we implemented a method consisting of chopping the pump pulses to 500 Hz and setting the bias field at 250 Hz. This allows one to obtain ΔE and E simultaneously, correcting for any drift on the pulse arrival that might occur. In addition, it corrects for the noise occurring over seconds, as both components will contain it, but it adds the shot to shot noise due to the difference operation. In the end, the pros outweigh the cons and this is the measurement method used for all pump-probe results in this thesis. In classical TRTS, ΔE can be obtained directly, by chopping the pump at 500 Hz, which already can account for this noise cancellation. However, in an ABCD configuration the need to compare between positive and negative field excludes this possibility. Finally, the two possibilities are to either obtain E and E_{ex} separately or simultaneously. Certainly, the simultaneous acquisition has many advantages, being the clear choice, and it is particularly important when acquiring spectra. An example of the noise reduction due to simultaneous acquisition of a frequency-averaged pump-probe scan is shown in the Appendix (Figure A.1).

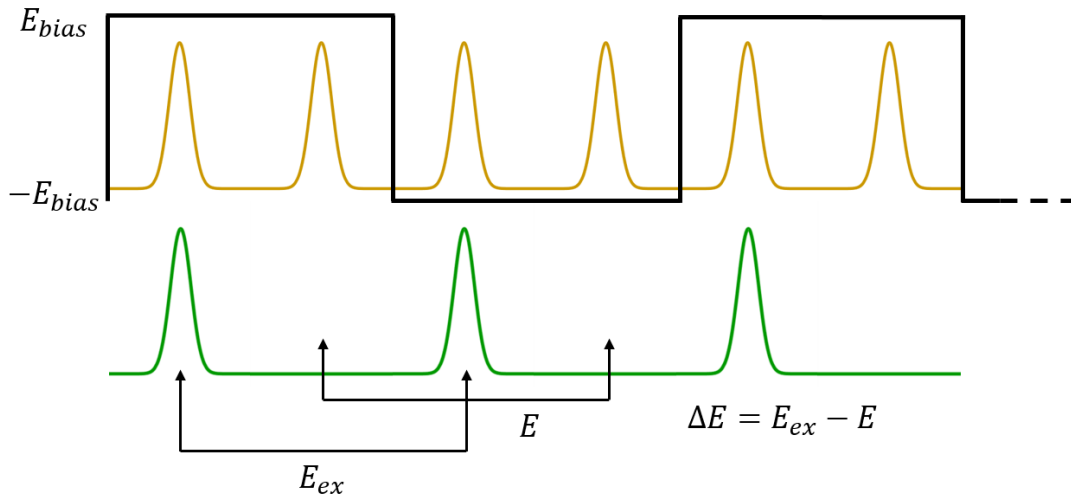


Figure 2.3: Pump-probe measurement method. The repetition rate for the THz (yellow) is 1 kHz while the pump (green) is chopped to 500 Hz. A square bias field is set to 250 Hz to compare pulses one position away from each other.

2.1.4 Setup

The following setup was built during this PhD thesis on top of a previously existing setup, based on optical rectification and electro-optic sampling, which was built and modified by Verner K. Thorsmølle, Jan C. Brauer²³ and Arun A. Paraecattil.²⁷ Preliminary work was carried out by or in collaboration with Ahmad Ajdarzadeh.

The TRTS setup (see Figure 2.4) has been previously described in refs. [28, 29]. Three beams were split from the fundamental output (45 fs pulse duration, $\lambda = 800$ nm, 1 kHz repetition rate) of an amplified Ti:sapphire laser (Libra USP HE Model, Coherent) and used for the TRTS experiments. The first beam was employed to pump a white light-seeded optical parametric amplifier (OPerA Solo, Coherent) that provided the pump pulses for the pump-probe experiment at tuneable wavelengths. Alternatively, the same beam could be diverted to obtain 400 nm pulses through second harmonic generation in a BBO crystal. The pump pulses were directed towards the sample through a divergent

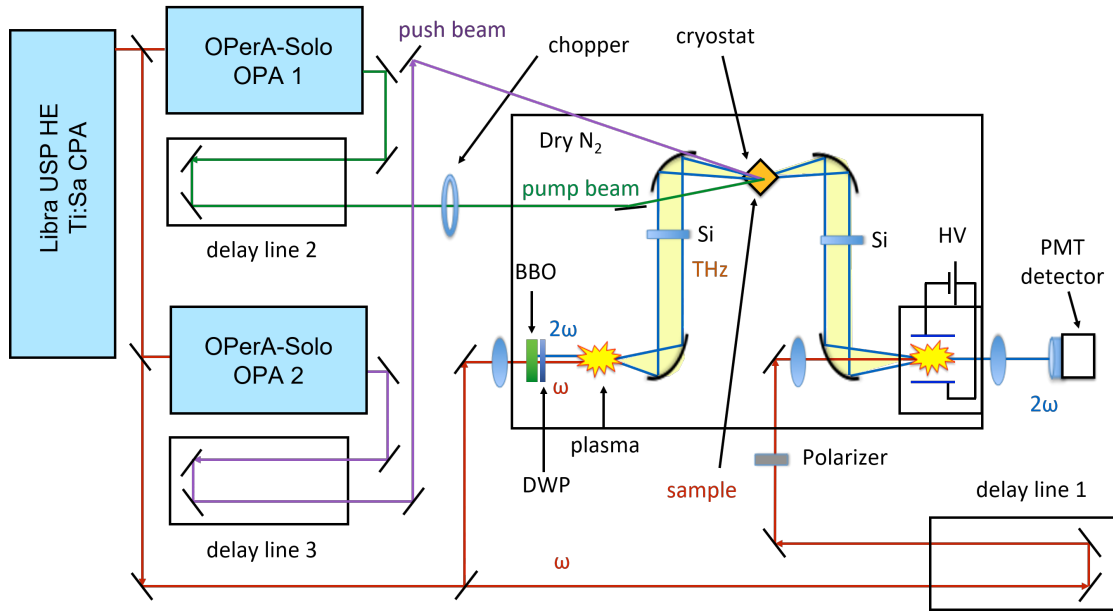


Figure 2.4: TRTS setup.

lens in order to broaden the beam. This ensured a homogeneous excitation of the probed region. The more powerful of the two remaining beams ($390 \mu\text{J}$ per pulse) was used to generate the probe beam, consisting of a train of short and broadband THz pulses, through a two-color plasma method.⁸ The beam was focused with a fused silica lens ($f = 75 \text{ mm}$), and the second harmonic was generated with a $100 \mu\text{m}$ BBO crystal. At the focal point, the electric field of the two-color beam was sufficiently strong to form a plasma filament in nitrogen that radiated a broadband THz pulse (200 fs , $1\text{--}20 \text{ THz}$) that was subsequently collimated and focused with parabolic gold mirrors onto the sample. The sample holder was contained inside a cryostat that can be used for low temperature measurements. To maximize THz generation, a dual wavelength waveplate was used immediately after the BBO crystal to obtain fundamental and second harmonic beams of equal polarization after type 1 phase matching.¹¹ The transmitted beam went through two additional parabolic mirrors towards a homemade ABCD (air-biased coherent detection) detector.¹⁵ Silicon wafers were used to filter the visible light from the THz generation and pumping. The remaining beam ($40 \mu\text{J}/\text{pulse}$) was used as a gate for the detection, generating a second harmonic signal proportional to the THz electric field measured with a PMT (PMM01, Thorlabs). The SHG process was carried out in the ABCD detector through the use of an oscillating 2 kV bias at either 500 or

250 Hz. This was generated with a function generator (wave Station 3122, Teledyne Lecroy) and amplified with a high voltage amplifier (Model 2220, Trek). It was applied across two electrodes separated by ~ 1 mm. The process could be carried out in an enclosed box with TPXTM windows, where the atmosphere was replaced with butane gas.¹⁹ This configuration resulted in an increase in the sensitivity at the expense of frequencies in the 12-20 THz range. It was used to increase the signal-to-noise ratio in the frequency-averaged dynamics. This setup also has an additional OPA that can be used to generate a push beam to carry out pump-push-probe experiments. The data was acquired through a LabVIEW software (National Instruments).

2.1.5 Data analysis

In addition to the selectivity of TRTS to charge carriers and low energy resonances, one of the inherent advantages of this technique lies in the possibility to extract additional information such as charge carrier mobility or permittivity in a material. This can be obtained from ΔE and E .

2.1.5.1 Data treatment

When investigating solid thin film samples of semiconducting materials for optoelectronic applications, the quantity that is generally determined first is the photoconductivity ($\Delta\sigma$). From it, other parameters such as carrier mobility or behavior can be extracted. $\Delta\sigma$ is the change in conductivity upon photoexcitation and it can be extracted from TRTS measurements. Based on ref. [22] we can show how to obtain $\Delta\sigma$ from measurable quantities such as E and ΔE .

Assuming that ΔE is small compared to E and considering a thin film, we can use Ohm's law to relate the photoconductivity ($\Delta\sigma(\omega)$) to the current density $J(t)$ generated in a material, with photogenerated charges, due the passing of a THz electric field ($E(t)$).

$$\Delta\sigma(\omega) = \frac{F[J(t)](\omega)}{F[E(t)](\omega)}, \quad (2.20)$$

where F is the Fourier transform operator, necessary to obtain the response in the frequency domain.

$$F[f(t)](\omega) = \int_{-\infty}^{\infty} f(t)e^{i\omega t} dt. \quad (2.21)$$

It can be shown that the current density is proportional to ΔE (See Section B.1, in the Appendix).

$$J(t) = -\frac{\varepsilon_0 c (n_A + n_B)}{L} \Delta E(t), \quad (2.22)$$

where n_A and n_B are the refractive indexes of the layers before and after the photoactive layer (typically air and the substrate) and L is its thickness. Thus, from Equations 2.20 and 2.22, we can obtain an equation for the determination of $\Delta\sigma(\omega)$

$$\Delta\sigma(\omega) = -\frac{\varepsilon_0 c (n_A + n_B)}{L} \frac{\Delta E(\omega)}{E(\omega)}. \quad (2.23)$$

This equation is valid under a steady-state condition, where $\Delta\sigma(\omega)$ does not substantially change along the duration of the pulse. However, this is not always the case, especially at very short pump-probe delays. A solution was introduced by Beard et al. in ref. [21] where a 2D map is produced and $\Delta\sigma(\omega, \tau)$ is obtained along the diagonal. Alternatively, ΔE can be measured scanning simultaneously the pump-probe and the gate-probe delays, allowing to obtain ΔE waveforms where all the data points have a constant delay (τ) from the arrival of the pump.^{23,24} $\Delta E(t)$ and $E(t)$ are easily obtained through the methods previously mentioned. However, it is rather common to obtain small to moderate offsets in the data. In E , the offset may come from the process explained in Section 2.1.3.2. On the other hand, ΔE may have an offset coming from the pump light, especially if the second harmonic is used. These offsets, since they are present at all delay times, are easily measured and subtracted.

In order to use Equation 2.23, the refractive indexes n_A and n_B must be determined. We can approximate that the refractive index of air, or N_2 , is $n_A \approx 1$. However, the refractive index of the substrate n_B may have to be determined for the frequencies involved. This can be obtained from a linear THz-TDS measurement of the transmitted THz pulse through the sample (E) and one transmitted only through air (E_{ref}). Applying a fast Fourier transform (FFT) operation to both signals, we can obtain their respective power (P and P_{ref}) and phase (ϕ and ϕ_{ref}). The phase must be “unwrapped”, removing the discontinuities typically present due to the result being in the range from $-\pi$ to π rad. An example is shown in the Appendix (Figure A.2). The refractive index can then be calculated as

$$n = 1 + \frac{c}{2\pi\omega L} (\phi - \phi_{ref}). \quad (2.24)$$

Additionally, the absorption coefficient α can be calculated with the power:

$$\alpha = -\frac{1}{L} \ln\left(\frac{P}{P_{ref}}\right). \quad (2.25)$$

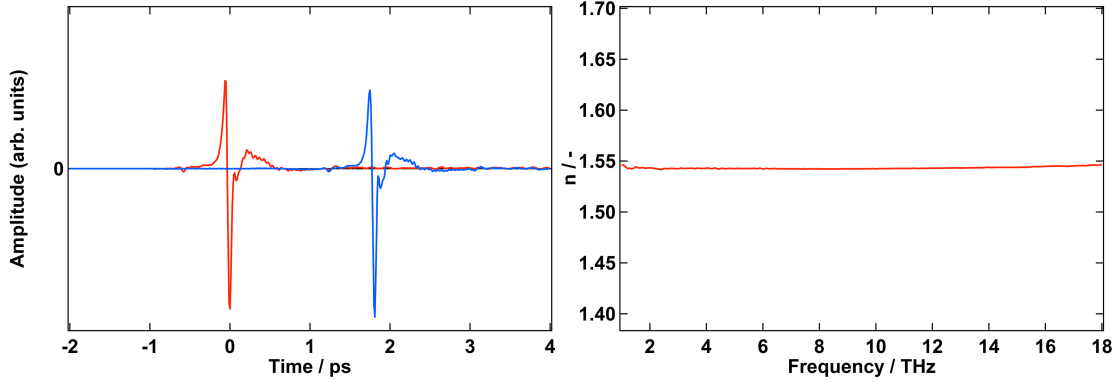


Figure 2.5: Difference in pulse arrival (left) when transmitted through a 1 mm HDPE sheet (blue) and corresponding refractive index (right).

In Figure 2.5 we show the calculation of the refractive index of an HDPE sheet, necessary for the measurements carried out in the following chapters. A flat response across the different frequencies can be observed averaging *ca.* 1.543. Alternatively, if the two pulses have the same shape it means that the phase velocity is equal at all frequencies, meaning that the refractive index is equally constant. In that case a simpler equation can be used:

$$n = \frac{c}{L} \Delta t + n_{ref}. \quad (2.26)$$

From the difference in arrival time Δt and the thickness L we can directly calculate the refractive index of the sheet material. This equation is obtained directly from the definition of refractive index as the relation between the speed of light in vacuum (c) and the phase velocity in a material (Section B.2, in the Appendix). From this equation we equally obtain $n = 1.543$ for HDPE. Likewise, a value of 1.54 can be found in the literature.³⁰

2.1.5.2 Models

Once the photoconductivity spectra have been obtained, it is useful to apply different models to either extract further information or prove a hypothesis. Several models have

been proposed over the past decades. Here, we review the most important ones, relevant for the work that will be presented in the following chapters.

Drude model

The simplest and most commonly applied model is the Drude model. Originally proposed by P. Drude,³¹ it considers a classical electron gas with an average scattering time τ . We can start from a DC condition in order to obtain its conductivity σ_{DC} and other parameters.^{4,32,33} This model considers that charge carriers will attain an average velocity, the drift velocity v_{dr} , by accelerating over the average time τ . We define the drift velocity

$$v_{dr} = \frac{qE\tau}{m^*}, \quad (2.27)$$

where qE is the Coulomb force applied on a charge carrier under an electric field E . v_{dr} is simply obtained by dividing the force by the effective mass m^* (acceleration) and multiplying by τ . We can use it to calculate the current density as

$$J = Nqv_{dr} = \frac{Ne^2E\tau}{m^*}, \quad (2.28)$$

where N is the carrier density and knowing that $q = -e$ for electrons (equally valid for holes). Then, from Ohm's law, the σ_{DC} is easily obtained as

$$\sigma_{DC} = \frac{J}{E} = \frac{Ne^2\tau}{m^*}. \quad (2.29)$$

We can then define the plasma frequency ω_p as

$$\omega_p = \sqrt{\frac{Ne^2}{\varepsilon_0 m^*}}, \quad (2.30)$$

so that

$$\sigma_{DC} = \varepsilon_0 \omega_p^2 \tau. \quad (2.31)$$

Additionally, we can use Equation 2.29 to define the mobility μ as a function of τ , since

$$\sigma_{DC} = eN\mu. \quad (2.32)$$

Then,

$$\mu = \frac{e\tau}{m^*}. \quad (2.33)$$

Therefore, knowing the scattering time and the effective mass, the DC mobility can be obtained.

We can now turn our attention to the frequency resolved $\sigma(\omega)$ that is obtained through this model. One way to derive it is from the impulse-response formalism.^{34,35} Going back to Ohm's law, $J(\omega) = \sigma(\omega)E(\omega)$, we can use the convolution theorem to say that

$$J(t) = \int_{-\infty}^{\infty} \sigma(t - t')E(t')dt'. \quad (2.34)$$

In the impulse-response formalism we consider the electric field to be an instantaneous impulse represented as

$$E(t') = E_i\delta(t'), \quad (2.35)$$

where E_i is the impulse magnitude. Thus, after substitution, the convolution gives

$$J(t) = \int_{-\infty}^{\infty} \sigma(t - t')E_i\delta(t')dt' = \sigma(t)E_i. \quad (2.36)$$

Now, the impulse-response can be defined as

$$\frac{J(t)}{E_i} = \sigma(t) \equiv j(t). \quad (2.37)$$

According to the Drude model, carriers scatter with a rate of $1/\tau$, meaning that their impulse-response is damped with that rate so

$$j(t) = j(0)e^{-\frac{t}{\tau}}\Theta(t), \quad (2.38)$$

where $\Theta(t)$ is the unit step function. It is the mathematical way of representing that there is no current before t_0 . $\sigma(\omega)$ is the result of the straightforward Fourier transform

$$\sigma(\omega) = \int_{-\infty}^{\infty} j(t)e^{i\omega t}dt. \quad (2.39)$$

Which, upon substitution turns into

$$\sigma(\omega) = \int_0^{\infty} j(0)e^{-\frac{t}{\tau}}e^{i\omega t}dt, \quad (2.40)$$

where the step function is taken into account by truncating the integration to $[0, \infty)$. It is considered that the electrons initially behave as perfectly free since the impulse is greater than any other forces being applied to them. In addition, the impulse $E_i\delta(t)$, by definition, is equivalent to an impulse of electric field E_i given during 1 unit of

time. Therefore, with a similar reasoning as for σ_{DC} , the initial response is given by $j(0) = ne^2/m^*$. Solving Equation 2.40 gives the classical Drude formula with its variants

$$\sigma(\omega) = \frac{ne^2}{m^*} \frac{\tau}{1 - i\omega\tau} = \frac{\sigma_{DC}}{1 - i\omega\tau} = \frac{\varepsilon_0\omega_p^2\tau}{1 - i\omega\tau}. \quad (2.41)$$

The Drude formula shows a nice consistency, as it can also be obtained from a semi-classical Boltzmann transport equation as well as from the Kubo-Greenwood formalism.^{4,33} An example of a Drude fit for a Si wafer using the ultra-broadband THz setup is shown in Figure 2.6. This also serves as a demonstration of the broadband capabilities of the setup.

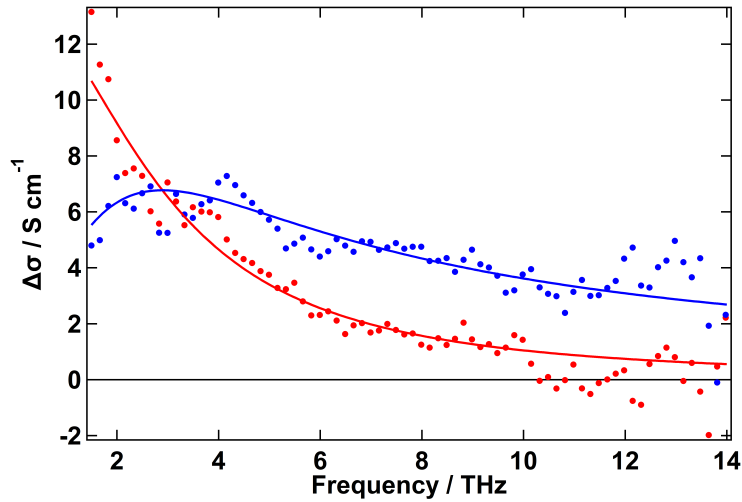


Figure 2.6: Real (red) and imaginary (blue) parts of the photoconductivity measured on a silicon wafer 2 ps after photoexcitation at $\lambda_{exc} = 510nm$. The response can be fitted to a Drude model (solid lines).

Fitting the Drude equation to TRTS spectra can directly yield the carrier density and mobility if the effective mass is known. It also identifies the material as a classical material where charge carriers behave as a classical electron gas. The Drude model has been successfully applied in different materials such as ZnO³⁶ or GaAs.⁵ However, semiconductors often present small deviations from the Drude spectrum. These can be

modeled from extensions of the model such as the Cole-Davidson model

$$\sigma(\omega) = \frac{\sigma_{DC}}{(1 - i\omega\tau)^\beta}, \quad (2.42)$$

where the parameter β has been added to account for a distribution of τ . This model showed very good agreement with doped Si.³⁷ Further modification into a generalized Drude model (GD),

$$\sigma(\omega) = \frac{\sigma_{DC}}{(1 - (i\omega\tau)^{1-\alpha})^\beta}, \quad (2.43)$$

has been used to fully account for the spectral response in GaAs.²¹

Drude-Smith model

The Drude model considers that the scattering is randomized in all directions. Therefore, on average, it can be considered that the carriers are stopped in the direction of the electric field after each collision. This allows one to derive the Drude model using v_{dr} . However, it cannot be expected that this randomized scattering will occur in all kinds of materials. Additionally, many materials show a strong deviation from the Drude response, where the real part of $\sigma(\omega)$ has a maximum at zero frequency and the imaginary part is always positive. Sometimes the real part shows actually a local minimum at zero frequency and a negative imaginary part. This is especially common in nanostructured or polycrystalline samples. Smith proposed a generalization of the Drude model through Poisson statistics with the idea that carriers may retain some velocity after a collision.³⁴ Since the probability of having n collisions in the interval $(0, t)$ is given by

$$p_n(0, t) = \left(\frac{t}{\tau}\right)^n \frac{e^{-\frac{t}{\tau}}}{n!}, \quad (2.44)$$

we can rewrite the impulse-response function from the Drude model as

$$j(t) = j(0)e^{-\frac{t}{\tau}} \left[1 + \sum_{n=1}^{\infty} \frac{c_n \left(\frac{t}{\tau}\right)^n}{n!} \right] \Theta(t), \quad (2.45)$$

where c_n is the fraction of the carrier's velocity that is preserved after the n^{th} collision and it takes values ranging from $[-1, 0]$ to model back-scattering. This means that part of the impulse-response will change direction as the back-scatterings occur (Figure 2.7).

After Fourier transform and substitution, it gives the general formula

$$\sigma(\omega) = \frac{\varepsilon_0 \omega_p^2 \tau}{(1 - i\omega\tau)} \left[1 + \sum_{n=1}^{\infty} \frac{c_n}{(1 - i\omega\tau)^n} \right]. \quad (2.46)$$

This equation needs to be simplified in order to apply it to TRTS spectra. The typical assumption is that carriers only retain velocity after the first collision. Therefore, only $c_1 \neq 0$. As a result we obtain

$$\sigma(\omega) = \frac{\varepsilon_0 \omega_p^2 \tau}{(1 - i\omega\tau)} \left(1 + \frac{c}{1 - i\omega\tau} \right), \quad (2.47)$$

which is the classical Drude-Smith formula. Under this model the mobility should be calculated as

$$\mu = (1 + c) \frac{e\tau}{m^*}. \quad (2.48)$$

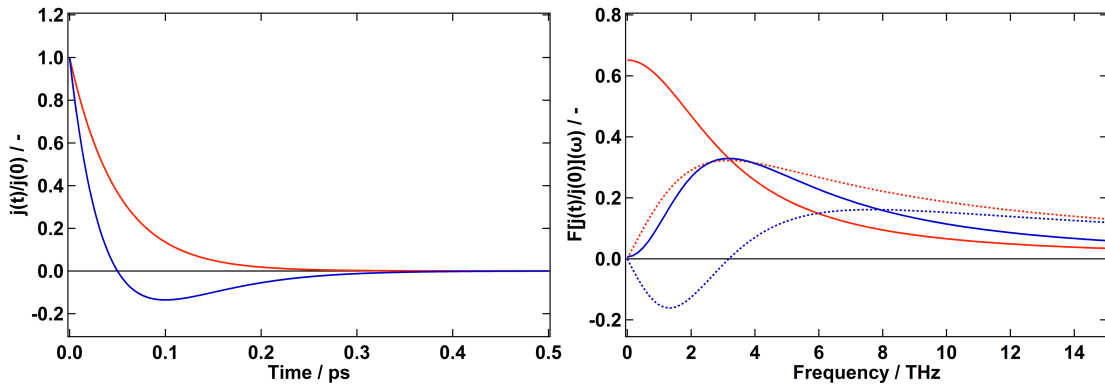


Figure 2.7: Comparison between the Drude ($c = 0$, red) and the Drude-Smith ($c = -1$, blue) impulse-responses (left) and their Fourier transforms (right, equivalent to $\sigma(\omega)$). The imaginary part is given by the dashed traces.

The Drude-Smith model has been applied to different systems such as Si nanocrystals³⁸ or polycrystalline perovskite films³⁹ and many others.^{40–43} It serves as a qualitative explanation for the displaced maximum in $\text{Re}[\sigma(\omega)]$ observed in certain materials. However, the model is often criticized for a) the lack of explanation concerning the approximation that only the first scattering event retains a certain velocity and b) the ambiguous physical meaning of the parameter fits. These problems and possible solutions based on the modification of the model were recently explored by Cocker et al.³⁵

Lorentzian oscillator

THz absorption in solid state materials is not limited to the response of free carriers to an electric field. Resonances such as the ones corresponding to excitonic transitions or

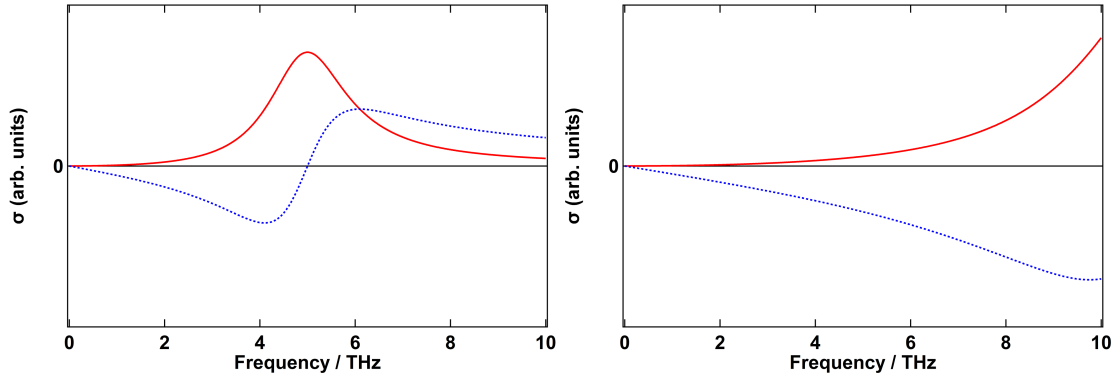


Figure 2.8: Lorentz oscillator simulations for resonances centered (left, $\nu_0 = 5$ and $\gamma = 2$) and outside (right, $\nu_0 = 12$ and $\gamma = 5$) the available spectrum. The imaginary parts are given by the dashed curves.

involving lattice vibrations can also be observed. The simplest way to model a resonance is through a Lorentzian oscillator

$$\sigma(\omega) = \frac{Ai\omega}{\omega^2 - \omega_0^2 + i\gamma\omega}, \quad (2.49)$$

where ω_0 is the resonance frequency, γ is its width and A its amplitude. In a way, the Drude model has a very similar behavior to a Lorentz oscillator, since it corresponds to the case where $\omega_0 = 0$.² An example of a Lorentz oscillator response is shown in Figure 2.8.

All these models are given in angular frequency (ω). However, the data is typically presented in frequency ($\nu = \frac{\omega}{2\pi}$). This has to be taken into account for data fitting (Section B.3, in the Appendix).

2.1.6 Substrates

In order to carry out ultra-broadband TRTS measurements, it is necessary to find a suitable substrate, flatly transparent to the THz pulses, as well as affordable and easy to handle. Typically, what should be avoided are a) free charges, such as in metals or heavily doped semiconductors and b) strong vibrational transitions, especially important in materials presenting polar groups or ions. Polymers are one of the cheapest and easier to obtain materials that can fulfill these conditions and be used as substrates. However,

polar groups, giving a large transition dipole moment, should be avoided. The first polymers to discard are those containing these, such as poly(methyl methacrylate) (PMMA) or poly(ethylene terephthalate) (PET), or even any heteroatom, such as polytetrafluoroethylene (PTFE, Teflon[®]),⁴⁴ since they involve complete or partial absorption of the 1-20 THz spectrum, especially when using millimeter thick substrates. In the Appendix Figure A.3 we show the effects on the transmitted THz of a polystyrene (PS) cuvette and a PTFE film. Thick sheets of PTFE absorb most of the THz frequencies above 5 THz. Therefore, we considered simple polymers, such as polypropylene (PP), polymethylpentene (PMP, TPX[™]), and high-density polyethylene (HDPE). In addition, branching (of a few carbon atoms) will generally lead to higher degrees of freedom and thus more vibrational modes to be excited. Indeed, HDPE, the simplest polymer, was found to be the most transparent up to a frequency of 20 THz and was chosen as the substrate to support the thin films in our experiments. Quartz is the substrate typically chosen for THz spectroscopy below 3 THz. However, it shows strong absorption from phonon modes and is completely opaque over 5 THz. The spectra of the transmitted pulses through the mentioned materials are shown in Figure 2.9. Occasionally, the pulses transmitted through a sheet of material can have a larger amplitude, especially at higher frequencies. This is most probably due to a slight change in the path and, thus, the alignment of the THz beam onto the detector. This is an important issue if the aim is to obtain absorption spectra of bulk materials. Nevertheless, this is not a concern in this work since we are always studying the effects of photoexcitation on thin films. Thus, the path length does not change substantially.

TPX[®] is an interesting material that is transparent both in the THz region, up to 12 THz, and the visible. It can be used for windows such as the one in our detection box.

2.2 Ultrafast transient absorption spectroscopy

Ultrafast transient absorption (TAS) is a spectroscopic technique based on the use of ultra-short optical laser pulses with a FWHM on the order of tens to a few hundreds of fs. In particular, a pump-probe setup usually makes use of a monochromatic pump pulse to excite the sample and a white light continuum (WLC) pulse to probe the changes undergone at different delay times after the pump. Similarly to TRTS, the difference

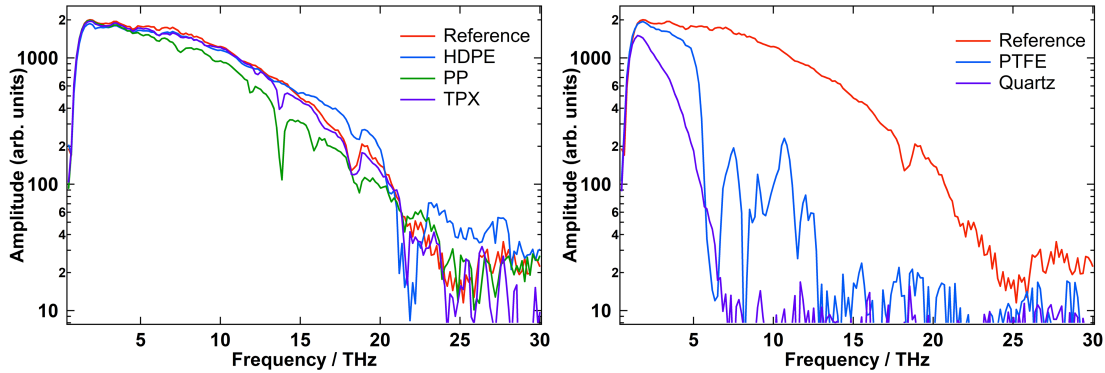


Figure 2.9: THz pulse transmitted through the 3 candidate polymers (left) and through the bad substrates PTFE and Quartz (right), all of which have thickness of 1 mm. HDPE presents the flattest transmission without important vibrational bands, such as the one at 13.7 THz present in both of the other aliphatic polymers. In fact, we can clearly observe the far infrared vibrational bands reported for PP at 7.4 THz (248 cm^{-1}), 9.6 THz (320 cm^{-1}), 11.9 THz (396 cm^{-1}), 13.7 THz (456 cm^{-1}) and 15.8 THz (528 cm^{-1}).⁴⁵ This serves as evidence of the frequency precision of the setup. Clearly, both PTFE and Quartz cannot be used as substrates in an ultra-broadband THz spectrometer, as they are totally or partially opaque to frequencies higher than 5 THz.

in time between pump and probe is achieved through a difference in optical pathlength using a delay stage. The transient increment in absorption signal (ΔA) is obtained through the subtraction of an only-probe to a pump+probe measurement. Therefore, positive signals are interpreted as more absorbance or less probe light coming to the detector and negative signals as more light, from either less absorbance or stimulated emission. In stimulated emission, the excited electron interacts with the electromagnetic field of an incoming probe photon, emitting a coherent photon. Thus, the probe light intensity increases. In addition, a reference beam is used to account for white-light fluctuations. Defining the pump+probe reference (I_p^r) and signal (I_p^s) intensities and the only-probe reference (I_{np}^r) and signal (I_{np}^s) intensities, ΔA is expressed as⁴⁶

$$\Delta A = -\log \left(\frac{I_p^s I_{np}^r}{I_{np}^s I_p^r} \right). \quad (2.50)$$

2.2.1 Setup

The following home-built setup was originally developed by S. Pelet⁴⁷ and later modified by B. Wenger.⁴⁸ Final modifications on the WLC were carried out by J. Teuscher, J. Risse, A. Marchioro and N. Banerji.⁴⁶

A Ti:Sapphire femtosecond laser (CPA-2001, Clark-MXR) was used to deliver pulses centered at 775 nm and having a FWHM of about 120 fs for an average peak power of 1 mJ at 1 kHz repetition rate. The pump pulse could be tuned using a Non-collinear Optical Parametric Amplifier (NOPA-Plus, Clark-MXR) and re-compressed with a pair of SF10 prisms. The pump size and intensity at the sample were measured with a beam profiler (BC 106-Vis, Thorlabs) and an energy meter (Vega, Ophir). This allowed to calculate the fluence. The WLC was obtained by focusing the fundamental 775 nm pulse from the laser onto a CaF₂ crystal. The WLC probe was split into a signal beam, focused on the sample, and a reference beam. Both beams were then detected by two spectrographs (Princeton instruments, SpectraPro 2500i) equipped with 512×58 pixel back-thinned CCD cameras (Hamamatsu S7030-0906) and assembled by Entwicklungsbüro Stresing, Berlin. Calibration of the spectrographs was carried out by placing interference filters in the WLC beam (before splitting). A chopper at 500 Hz in the pump path was used to distinguish between the only-probe and the pump+probe acquisitions. A LabVIEW software (National Instruments) was used for the data acquisition. The software showed in real time the WLC for both cameras and the resulting ΔA helping in the optimization of the system.^a The data obtained with this setup consisted of a matrix of ΔA values for the different time-delays and wavelengths. Therefore, both spectra at different delays and decay dynamics at different wavelengths could be obtained, similar to the 2D frequency-time spectrum mentioned in the THz section.

^aThe above equipment description was mostly taken from J. Risse's thesis

2.3 Broadband fluorescence up-conversion spectroscopy

Broadband fluorescence up-conversion spectroscopy (FLUPS) is an ultrafast time-resolved technique that allows one to obtain photoluminescence spectra with sub-ps resolution. The setup was purchased from LIOP-TEC and installed by Prof. Nikolaus Ernsting from Humboldt University.⁴⁹ The setup is managed by Etienne Socie and a further in-depth description will appear in his thesis. Nonetheless, the following is an overview of how it operates.

2.3.1 Setup

Time-resolved emission measurements were achieved using the same CPA Ti:sapphire laser as for TRTS. Seventy-five percent of the beam was transmitted to a white-light-seeded optical parametric amplifier (OPerA-Solo, Coherent) to generate 110 μ J gate pulses at $\lambda = 1300$ nm. The rest of the original beam was frequency doubled to 400 nm by a type I BBO crystal and set to the magic angle (54.7°) to consider only the population dynamics. A small beam stop and a 400 nm filter was placed after the sample position to block most of the transmitted 400 nm pump light. The horizontally polarized gate beam and vertically polarized fluorescence interacted in the 100 μ m thick BBO crystal (Eksma Optics), which had an optical axis in the horizontal plane. The upconverted signal was generated by type II sum frequency generation since the two inputs had different polarizations. This configuration is suitable for obtaining a broad frequency range without any moving part. The large angle between the fluorescence and the gate beam, here 21° , helped the phase matching requirement and the background-free detection of the signal. The signal was focused onto a fiber by a concave mirror while the frequency-doubled gate beam and the upconverted pump beam were sent away. The fiber transmitted the light to an unfolded Czerny-Turner spectrograph (Triax 320, Jobin Yvon). The incoming signal was separated by wavelength through a UV grating and sent to a CCD detector (Newton 920, Andor). The dynamics of the fluorescence signal were obtained with a computer-controlled delay stage (Physik Instrumente) in the pump path. The time correction for the instrument response function (IRF) was calculated as 190 fs using the cross correlation between the pump and the probe.

2.4 Nanosecond flash photolysis

Nanosecond flash photolysis (NFP) is a time-resolved technique similar in its observable to TAS. However, whereas TAS is an ultrafast technique probing times below 2 ns, NFP probes the transient absorption from tens of ns to ms. Thus, it is a good complement to TAS in order to observe the decay of long-lived remnants that do not evolve in the TAS time-scale. Typically, a pulsed laser with a FWHM of several ns is used to pump the sample and the evolution of the system is probed with a continuous lamp. The incoming light is detected with either a PMT or a photodiode and digitized with an oscilloscope. ΔA is calculated with

$$\Delta A = -\log\left(\frac{I}{I_0}\right), \quad (2.51)$$

where I is the intensity with pumping while I_0 is the original transmitted intensity. A description of the system can be found in numerous publications.⁵⁰

References

- (1) Rostami, A.; Rasooli, H.; Baghban, H., *Terahertz Technology: Fundamentals and Applications*; Lecture Notes in Electrical Engineering; Springer-Verlag: Berlin Heidelberg, 2011.
- (2) Ulbricht, R.; Hendry, E.; Shan, J.; Heinz, T. F.; Bonn, M. Carrier Dynamics in Semiconductors Studied with Time-Resolved Terahertz Spectroscopy. *Rev. Mod. Phys.* **2011**, *83*, 543–586.
- (3) R. Alan Cheville In *Terahertz Spectroscopy Principles and Applications*, Susan L. Dexheimer, Ed.; CRC Press: 2008.
- (4) Dressel, M.; Gruner, G.; Grüner, G., *Electrodynamics of Solids: Optical Properties of Electrons in Matter*; Cambridge University Press: 2002; 490 pp.
- (5) Huber, R.; Tauser, F.; Brodschelm, A.; Bichler, M.; Abstreiter, G.; Leitensdorfer, A. How Many-Particle Interactions Develop After Ultrafast Excitation of an Electron-Hole Plasma. *Nature* **2001**, *414*, 286–289.
- (6) Cook, D. J.; Hochstrasser, R. M. Intense Terahertz Pulses by Four-Wave Rectification in Air. *Opt. Lett.* **2000**, *25*, 1210–1212.
- (7) Paschotta, D. R. Four-wave Mixing., https://www.rp-photonics.com/four_wave_mixing.html (accessed 11/25/2019).
- (8) Kim, K. Y.; Taylor, A. J.; Glowina, J. H.; Rodriguez, G. Coherent Control of Terahertz Supercontinuum Generation in Ultrafast Laser–Gas Interactions. *Nat. Photonics* **2008**, *2*, 605–609.
- (9) Kim, K.-Y.; Glowina, J. H.; Taylor, A. J.; Rodriguez, G. Terahertz Emission from Ultrafast Ionizing Air in Symmetry-Broken Laser Fields. *Opt. Express* **2007**, *15*, 4577–4584.
- (10) Kim, K.-Y.; Glowina, J. H.; Taylor, A. J.; Rodriguez, G. High-Power Broadband Terahertz Generation via Two-Color Photoionization in Gases. *IEEE J. Quantum Electron.* **2012**, *48*, 797–805.
- (11) Minami, Y.; Kurihara, T.; Yamaguchi, K.; Nakajima, M.; Suemoto, T. High-Power THz Wave Generation in Plasma Induced by Polarization Adjusted Two-Color Laser Pulses. *Appl. Phys. Lett.* **2013**, *102*, 041105.

- (12) Oh, T. I.; You, Y. S.; Jhajj, N.; Rosenthal, E. W.; Milchberg, H. M.; Kim, K. Y. Intense Terahertz Generation in Two-Color Laser Filamentation: Energy Scaling with Terawatt Laser Systems. *New J. Phys.* **2013**, *15*, 075002.
- (13) Oh, T. I.; Yoo, Y. J.; You, Y. S.; Kim, K. Y. Generation of Strong Terahertz Fields Exceeding 8 MV/cm at 1 kHz and Real-Time Beam Profiling. *Appl. Phys. Lett.* **2014**, *105*, 041103.
- (14) Oh, T. I.; You, Y. S.; Kim, K. Y. Two-Dimensional Plasma Current and Optimized Terahertz Generation in Two-Color Photoionization. *Opt. Express, OE* **2012**, *20*, 19778–19786.
- (15) Karpowicz, N.; Dai, J.; Lu, X.; Chen, Y.; Yamaguchi, M.; Zhao, H.; Zhang, X.-C.; Zhang, L.; Zhang, C.; Price-Gallagher, M.; Fletcher, C.; Mamer, O.; Lesimple, A.; Johnson, K. Coherent Heterodyne Time-Domain Spectrometry Covering the Entire “Terahertz Gap”. *Appl. Phys. Lett.* **2008**, *92*, 011131.
- (16) Nahata, A.; Heinz, T. F. Detection of Freely Propagating Terahertz Radiation by Use of Optical Second-Harmonic Generation. *Opt. Lett., OL* **1998**, *23*, 67–69.
- (17) Dai, J.; Xie, X.; Zhang, X.-C. Detection of Broadband Terahertz Waves with a Laser-Induced Plasma in Gases. *Phys. Rev. Lett.* **2006**, *97*, 103903.
- (18) Kikuchi, K.; Tada, K. Theory of Electric Field-Induced Optical Second Harmonic Generation in Semiconductors. *Opt. Quant. Electron.* **1980**, *12*, 199–205.
- (19) Lu, X.; Zhang, X.-C. Terahertz Wave Gas Photonics: Sensing with Gases. *J. Infrared Millim. Terahertz Waves* **2011**, *32*, 562–569.
- (20) Lu, X.; Zhang, X.-C. Investigation of Ultra-Broadband Terahertz Time-Domain Spectroscopy with Terahertz Wave Gas Photonics. *Front. Optoelectron.* **2014**, *7*, 121–155.
- (21) Beard, M. C.; Turner, G. M.; Schmuttenmaer, C. A. Transient Photoconductivity in GaAs as Measured by Time-Resolved Terahertz Spectroscopy. *Phys. Rev. B* **2000**, *62*, 15764–15777.
- (22) Nienhuys, H.-K.; Sundström, V. Intrinsic Complications in the Analysis of Optical-Pump, Terahertz Probe Experiments. *Physical Review B* **2005**, *71*, 235110.
- (23) Brauer, J. C. Linear and Time-Resolved THz Spectroscopy of Photonic and Charge Transporting Systems., Ph.D. Thesis, EPFL, 2012.

- (24) Dexheimer, S. L.; Baxter, J. B.; Schmuttenmaer, C. A. In *Terahertz Spectroscopy: Principles and Applications*; CRC Press: 2008.
- (25) Iwaszczuk, K.; Cooke, D. G.; Fujiwara, M.; Hashimoto, H.; Jepsen, P. U. Simultaneous Reference and Differential Waveform Acquisition in Time-Resolved Terahertz Spectroscopy. *Opt. Express, OE* **2009**, *17*, 21969–21976.
- (26) D’Angelo, F.; Parekh, S. H.; Bonn, M.; Turchinovich, D. In *CLEO: 2015, CLEO: Science and Innovations*, OSA: San Jose, California, 2015, STu4H.1.
- (27) Paraecattil, A. A. A Time-Resolved Photophysical Study of Hybrid Organic-Inorganic Perovskite Photovoltaic Materials., Ph.D. Thesis, EPFL, 2017.
- (28) Yan, W.; Burgos-Caminal, A.; Das Gupta, T.; Moser, J.-E.; Sorin, F. Direct Synthesis of Selenium Nanowire Mesh on a Solid Substrate and Insights into Ultrafast Photocarrier Dynamics. *J. Phys. Chem. C* **2018**, *122*, 25134–25141.
- (29) Burgos-Caminal, A.; Moreno-Naranjo, J. M.; Willauer, A. R.; Paraecattil, A. A.; Ajdarzadeh, A.; Moser, J.-E. Hot Carrier Mobility Dynamics Unravel Competing Sub-ps Cooling Processes in Lead Halide Perovskites. *arXiv:1909.04589 [cond-mat, physics:physics]* **2019**.
- (30) Folks, W. R.; Pandey, S. K.; Boreman, G. In *Optical Terahertz Science and Technology*, Optical Terahertz Science and Technology, OSA: Orlando, Florida, 2007, p MD10.
- (31) Drude, P. Zur Elektronentheorie der Metalle. *Ann. Phys.* **1900**, *306*, 566–613.
- (32) Kittel, C., *Introduction to Solid State Physics*, 5th; John Wiley & Sons, Inc.: 1976.
- (33) Dexheimer, S. L.; Kaindl, R. A.; Averitt, R. D. In *Terahertz Spectroscopy: Principles and Applications*; CRC Press: 2008.
- (34) Smith, N. Classical Generalization of the Drude Formula for the Optical Conductivity. *Phys. Rev. B* **2001**, *64*, 155106.
- (35) Cocker, T. L.; Baillie, D.; Buruma, M.; Titova, L. V.; Sydora, R. D.; Marsiglio, F.; Hegmann, F. A. Microscopic Origin of the Drude-Smith Model. *Phys. Rev. B* **2017**, *96*, 205439.
- (36) Hendry, E.; Koeberg, M.; Bonn, M. Exciton and Electron-Hole Plasma Formation Dynamics in ZnO. *Phys. Rev. B* **2007**, *76*, 045214.

- (37) Jeon, T.-I.; Grischkowsky, D. Nature of Conduction in Doped Silicon. *Phys. Rev. Lett.* **1997**, *78*, 1106–1109.
- (38) Cooke, D. G.; MacDonald, A. N.; Hryciw, A.; Wang, J.; Li, Q.; Meldrum, A.; Hegmann, F. A. Transient Terahertz Conductivity in Photoexcited Silicon Nanocrystal Films. *Phys. Rev. B* **2006**, *73*, 193311.
- (39) Yan, H.; An, B.; Fan, Z.; Zhu, X.; Lin, X.; Jin, Z.; Ma, G. Ultrafast Terahertz Probe of Photoexcited Free Charge Carriers in Organometal $\text{CH}_3\text{NH}_3\text{PbI}_3$ Perovskite Thin Film. *Appl. Phys. A* **2016**, *122*, 414.
- (40) Lovrinčić, R.; Pucci, A. Infrared Optical Properties of Chromium Nanoscale Films with a Phase Transition. *Phys. Rev. B* **2009**, *80*, 205404.
- (41) Turner, G. M.; Beard, M. C.; Schmittenmaer, C. A. Carrier Localization and Cooling in Dye-Sensitized Nanocrystalline Titanium Dioxide. *J. Phys. Chem. B* **2002**, *106*, 11716–11719.
- (42) Baxter, J. B.; Schmittenmaer, C. A. Conductivity of ZnO Nanowires, Nanoparticles, and Thin Films Using Time-Resolved Terahertz Spectroscopy. *J. Phys. Chem. B* **2006**, *110*, 25229–25239.
- (43) Phanindra, V. E.; Agarwal, P.; Rana, D. S. Epitaxial Strain Driven Crossover from Drude to Drude-Smith Terahertz Conductivity Dynamics in LaNiO_3 thin Films. *J. Phys.: Condens. Matter* **2017**, *29*, 445604.
- (44) D’Angelo, F.; Mics, Z.; Bonn, M.; Turchinovich, D. Ultra-Broadband THz Time-Domain Spectroscopy of Common Polymers Using THz Air Photonics. *Opt. Express* **2014**, *22*, 12475.
- (45) Erik Andreassen In *Polypropylene - An A-Z reference*, Jozsef Karger-Kocsis, Ed., 1st ed.; Springer Netherlands: 1999.
- (46) Risse, J. Ultrafast Dynamics of Photoinduced Charge Separation in Cyanine-and Polymer-Based Organic Photovoltaic Systems., Ph.D. Thesis, EPFL, 2015.
- (47) Pelet, S. Femtosecond Dynamics of Electron Transfer in the Photosensitization of Wide Band Gap Semiconductors., Ph.D. Thesis, EPFL, 2002.
- (48) Wenger, B. Effect of Electronic and Nuclear Factors on the Dynamics of Dye-to-Semiconductor Electron Transfer., Ph.D. Thesis, EPFL, 2006.

- (49) Gerecke, M.; Bierhance, G.; Gutmann, M.; Ernsting, N. P.; Rosspeintner, A. Femtosecond Broadband Fluorescence Upconversion Spectroscopy: Spectral Coverage Versus Efficiency. *Rev. Sci. Instrum.* **2016**, *87*, 053115.
- (50) Bouduban, M. E. F.; Burgos-Caminal, A.; Ossola, R.; Teuscher, J.; Moser, J.-E. Energy and Charge Transfer Cascade in Methylammonium Lead Bromide Perovskite Nanoparticle Aggregates. *Chem. Sci.* **2017**, *8*, 4371–4380.

Chapter 3

Charge carrier dynamics and mobilities in Se nanowires

This chapter introduces the simplest measurements that can be done with ultra-broadband TRTS in combination with other techniques, comparable to how classical TRTS setups would routinely operate. It is based on the paper *Direct synthesis of selenium nanowire mesh on a solid substrate and insights into ultrafast photocarrier dynamics*,¹ the product of a collaboration with Wei Yan and Tapjyoti Das Gupta, previously in the group of Prof. Fabien Sorin. They were responsible for sample preparation and non-spectroscopic characterization as well as participating in the overall discussion. Here, we will focus on the spectroscopy part carried out as part of this thesis. The photocarrier dynamics and mobility are studied and rationalized with a combination of laser spectroscopy techniques. The dynamics are found to be dictated by trapping, probably on the surface of the nanostructured material.

3.1 Introduction

One-dimensional semiconducting nanowires represent attractive building blocks for electronic and photonic devices^{2,3} such as transistors,⁴ optical devices,⁵ sensors,^{6,7} and metal oxide semiconductor circuits.⁸ Among the various chalcogenide materials, pure Se nanowires form an intriguing system both for fundamental and applied research. Interesting studies have been done based on Se nanowires (Se-NWs) in thermodynamics⁹ as well as crystal nucleation and growth.^{10,11} From an application point of view, Se was one of the first investigated materials for its interesting electronic and optoelectronic properties. It indeed has a very strong absorption in the visible range, and exhibits a good photoconductivity in its trigonal crystalline phase. Crystalline Se also has excellent piezoelectric properties,¹¹ and amorphous Se is being used as a scintillator for X-ray imaging.¹² It is however difficult to grow Se in the right phase and with large and well oriented grains, which has rendered Se-based devices difficult to fabricate. The formation of nanowires, however, is a promising approach to alleviate this difficulty and to control and optimize the microstructure of Se materials. Se-NWs have been investigated for high-speed photodetection,¹³ as efficient catalysts,¹⁴ for solar cells,¹⁵ fiber-based electronics,^{16,17} high-performance lithium-ion batteries^{18,19} and chemical sensors.²⁰

To fully exploit the potential of Se-NW based devices however, significant progress must be carried out in the understanding of their photocarrier dynamics as well as their fabrication. Despite the strong potential little is known concerning their charge carrier dynamics. Indeed, reviving the interest for, and improving the performance of Se-based devices via the growth of NW requires better characterization and understanding of charge carrier lifetime, mobility and recombination mechanisms. Furthermore, there is still plenty of room for improvement in the fabrication of Se-NW in order to obtain functioning optical and optoelectronic devices.

The original paper¹ reports a newly developed solution-based approach for the synthesis of monocrySTALLINE Se-NWs based on a recent method to integrate semiconducting nanowire based optoelectronic devices within functional polymeric fibers.¹³ This method takes knowledge from previous sonochemical methods,¹⁰ which was used to obtain colloidal suspensions. The method developed by W. Yan *et al.* allows one to obtain films

of a NW mesh on any solid substrates even without sonication. Se-NWs are phase-transformed directly from a deposited amorphous Se thin film of controlled thickness. The NWs directly grow when exposed to a solvent (1-propanol) at room temperature without any chemical reaction. In this chapter, we study samples obtained through this method with different laser spectroscopy techniques in order to unravel the charge carrier dynamics and mobilities, shedding new light on the optical and electrical properties of Se nanowires, via the ability to probe carriers on an ultrafast timescale. The nanowires were grown on glass for all measurements except for TRTS, where HDPE was used following the same method.

3.2 Results and analysis

3.2.1 Sample characterization

The samples consist of an array of nanowires in the form of islands at the center of which nucleation started and the nanostructures grew in all directions. Depending on the initial thickness of amorphous Se the resulting islands are more densely packed, forming a continuous film or having spaces in between (Figure 3.1). Due to the varying porosity across the nanowire film it is difficult to define a clear thickness. Thus, samples are described by the original thickness of the amorphous Se from which the nanowires grew. The monocrystalline wires can be assigned to a trigonal phase, from selected-area electron diffraction measurements, that preferentially grow in the [001] direction.

The optical response of the nanowire samples is characterized by the absorption and reflection spectra shown in Figure 3.2. The first thing to notice is a strong absorption and low reflection in the visible region below 670 nm, likely due to an anti-reflection effect from the porous nanowire mesh and light trapping. The onset of absorption agrees with a band gap at around 1.85 eV reported in the literature.^{21,22} The distribution of midgap states, enhanced by the increased surface area, creates a well-known tail of absorption below the band gap.²³ Overall, absorption increases with increasing thickness as expected, and it plateaus at around 90% above 430 nm of initial amorphous Se thickness owing to the 10% of reflectance. This can be seen in the Appendix (Figure A.4), where the transmittance is already negligible at this thickness. The optical properties can be compared to those obtained for single crystals of trigonal selenium.²⁴ For such

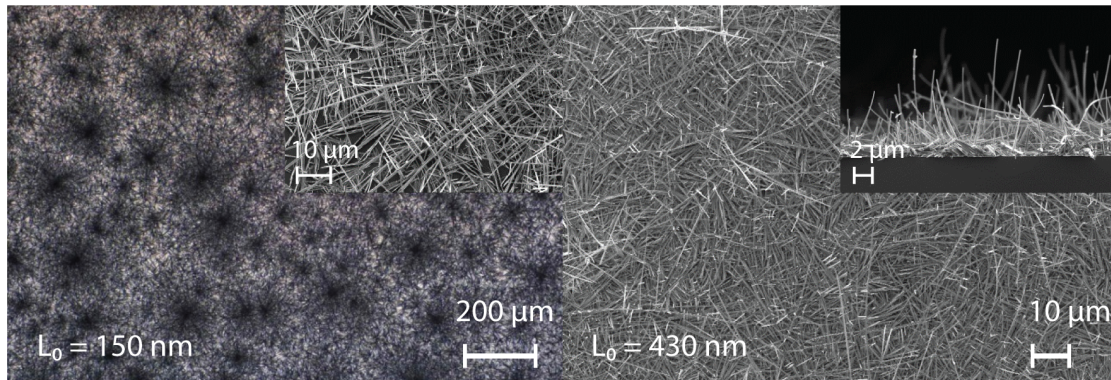


Figure 3.1: SEM pictures of two Se-NW films obtained from amorphous Se films of 150 nm(left) and 430 nm (right) in thickness. The inset on the right corner shows how the amorphous film is completely converted. 430 nm was found to be the limit for total conversion and was used for the TRTS measurements where a thicker film could improve the signal.

macroscopic crystals the reflectance is found to increase from the bandgap energy, due to the uniform reflective surface, reaching a local maximum at 2 eV (620 nm) and rises again after 2.5 eV (500 nm). This contrasts with our measurements where the absorption keeps decreasing at least until 350 nm. Nonetheless, the spectrum is comparable to that obtained for colloidal suspensions of similar nanowires.¹¹

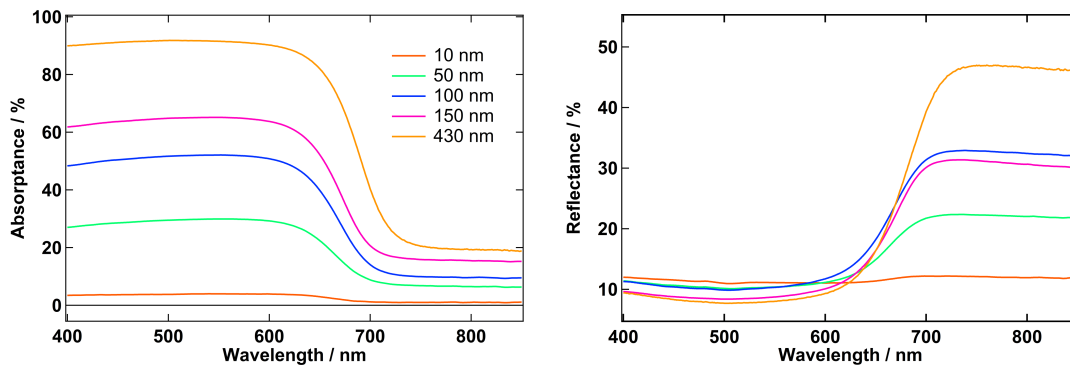


Figure 3.2: Visible and near-infrared absorbance and reflectance spectra of nanowire samples grown from 10, 50, 100, 150 and 430 nm thin films.

3.2.2 Charge carrier dynamics

The charge carrier dynamics of the nanowire network were characterized using a combination of three time-resolved spectroscopy techniques, *i.e.*, time-resolved terahertz spectroscopy (TRTS), ultrafast transient absorption spectroscopy (TAS), and nanosecond flash photolysis (NFP). We first probed the nanowires with ultrafast TRTS and TAS on the picosecond time scale. TRTS relies on the measurement of the change in transmission of the terahertz electric field through the sample, which can be directly related to the photoconductivity.²⁵ In order to improve the signal, the thickness of the nanowire mesh for the TRTS characterization can be controlled to completely absorb the pump pulses (here, $\lambda_{\text{exc}} = 500$ nm), thereby maximizing charge carrier generation without the need to increase the fluence of the pump pulse. Hence, a nanowire sample grown from a 400 nm thin film that exhibits the highest absorption (Figures A.4 and 3.2) was used for this measurement. Alternatively, TAS records the difference of absorption spectra (ΔA) between the excited sample and the sample in the ground state. Thus, the sample must be partially transparent to the probe pulse. In this case, a nanowire sample grown from a 200 nm thin film was used.

As shown in Figure 3.3, a rapid rise in photoconductivity and ΔA in the respective signal, limited by the time resolution of the instrument, is observed after the photoexcitation due to the generation of carriers. A very fast multiexponential decay in the order of a few ps is readily observed after the rise with both methods. The faster part of the signal decay (90% of the TRTS one) can be fitted with a biexponential equation (See Appendix, Equation B.26), obtaining lifetimes in the order of $\tau_1 = 0.5$ ps and $\tau_2 = 3$ ps. These carrier lifetimes are comparable to those of some silicon, GaAs, and GaAs/AlGaAs core-shell nanowires.²⁶ There is a clear differentiation between the signals that can be obtained with the two techniques. In TRTS, unless a major transition corresponding to a low energy vibrational mode is strongly affected, the photoconductivity is responsible for an increased absorption of THz. This photoconductivity arises from the introduction of new charge carriers and depends on their density and mobility.²⁷ Intra-excitonic transitions may also produce THz absorption but these are probably negligible, judging from the absence of a clear excitonic band in the absorption spectrum (Figure 3.2). Thus, a decrease in THz absorption over time can be attributed to carrier recombination or a decrease in mobility, or both. In TAS, any excited-state species that produces a change

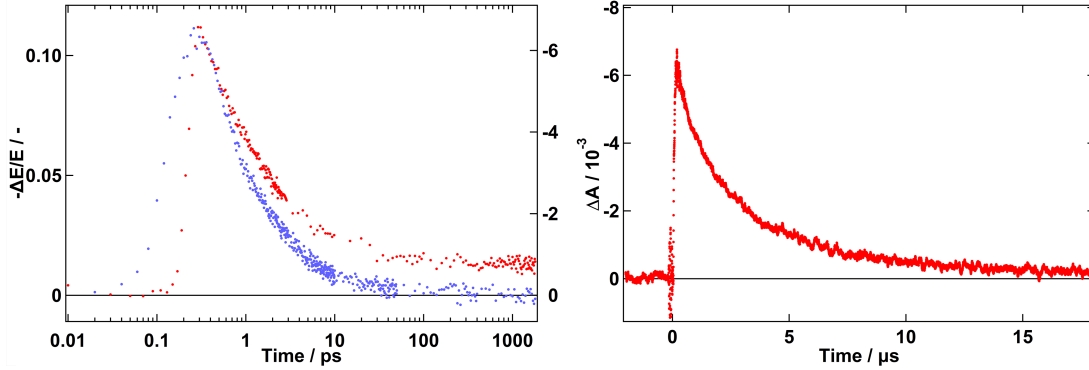


Figure 3.3: Left) Time dependence of the photoconductivity and the difference of absorption (ΔA) measured by the TRTS (blue, $\lambda_{\text{exc}} = 500$ nm, $F = 426 \mu\text{J cm}^{-2}$) and TAS (red, $\lambda_{\text{obs}} = 650$ nm, $\lambda_{\text{exc}} = 520$ nm, $F = 96 \mu\text{J cm}^{-2}$) techniques for the nanowires grown from 400 and 200 nm thin films, respectively. Right) Time dependence of the difference in absorption (ΔA) measured by the long-lived NFP technique ($\lambda_{\text{exc}} = 532$ nm, $F = 211 \text{ mJ cm}^{-2}$) for the nanowires grown from a 200 nm thin film.

in the absorption profile in the visible region can be observed. In fact, the observed TAS signal in Figure 3.3 is a ground state bleaching (GSB, $\Delta A < 0$) near the band gap (650 nm). Any process that depletes the electron population capable of undergoing the transition with the corresponding energy will cause such a bleaching. This includes the formation of free carriers due to band filling²⁸ but also immobilized trapped carriers^{29,30} and excitons.^{31,32} Overall, the observed decay in both measurements is very similar. However, in TRTS we obtain a complete recovery of the initial signal, while in TAS a certain offset bleaching is maintained. If the fundamental difference between the signals obtained with the two experiments is taken into account, it can be concluded that most carriers rapidly return to the ground state, while a small portion stays in a state that gives rise to no or negligible THz absorption but allows a GSB. The same result is obtained for comparable fluences (See Appendix, Figure A.5). Trapped carriers are believed to fit in this description as they exhibit a greatly reduced mobility while maintaining a GSB, as has been reported previously.³³ In order to further explore this possibility, fluence-dependent TRTS measurements were carried out.

The results (Table 3.1) show limited changes in recombination lifetimes when changing

Fluence / $\mu\text{J cm}^{-2}$	τ_1 / ps	τ_2 / ps	τ_3 / ps	A_1 / 10^{-2}	A_2 / 10^{-2}	A_3 / 10^{-3}
71	0.68 ± 0.03	4.67 ± 0.32	1172 ± 124	2.00 ± 0.04	0.81 ± 0.04	2.40 ± 0.10
142	0.70 ± 0.07	5.18 ± 0.67	827 ± 210	2.52 ± 0.11	1.17 ± 0.12	4.10 ± 0.26
227	0.46 ± 0.02	3.03 ± 0.14	241 ± 38	5.32 ± 0.09	2.30 ± 0.09	4.10 ± 0.18
284	0.50 ± 0.02	3.69 ± 0.20	450 ± 128	6.94 ± 0.13	3.03 ± 0.13	4.00 ± 0.28
426	0.44 ± 0.03	2.69 ± 0.25	28 ± 5.3	8.30 ± 0.24	4.45 ± 0.21	8.58 ± 1.3
568	0.42 ± 0.02	2.53 ± 0.20	32 ± 5.4	9.20 ± 0.25	4.96 ± 0.20	9.3 ± 1.1

Table 3.1: Fluence-dependent fits for the TRTS measurements.

the fluence, except at lower fluences. Note that trigonal selenium (t-Se) is an indirect semiconductor^{34,35} that disfavors bimolecular recombination, and the sample is a nanowire mesh that exhibits a significantly enhanced density of midgap states (traps) due to the increased surface to volume ratio. It can therefore be concluded that the main recombination pathway is trap-assisted recombination (Shockley-Read-Hall)³⁶ instead of bimolecular recombination that is highly dependent on the excitation intensity. Indeed, there is some shortening with fluence and, thus, some bimolecular behavior. However, it is not as dominant as what can be found in a predominantly direct semiconductor such as lead halide perovskites. In order to probe the nature of these trapped carriers, we then performed NFP measurements on a microsecond timescale. Figure 3.3 shows that these trapped carriers can last up to tens of microseconds before completely recombining. Biexponential fits yielded lifetimes of $\tau_1 = 0.9 \mu\text{s}$ and $\tau_2 = 4.1 \mu\text{s}$. Fluence dependent NFP measurements, shown in Table 3.2, again indicate that carrier lifetime is not highly dependent on the incident flux, which further confirms the trap-assisted recombination mechanism. The microsecond time scale of these trapped carriers in our trigonal Se-NWs is comparable to that of mobile carriers recently reported in trigonal Se powders measured utilizing the transient microwave conductivity technique.³⁷ The recovery time on the picosecond time scale measured by TRTS can then be attributed to ultrafast trapping of carriers mediated by surface states of each individual nanowire and contacts between nanowires, given the large surface to volume ratio of these randomly arranged samples. Similar dramatic changes in carrier dynamics due to increased surface states have been observed before, *e.g.* in nanoporous²⁹ and microcrystalline³⁸ silicon. Therefore, a clear effect of the enhanced nanowire aspect ratio has been ob-

served, heavily enhancing monomolecular recombination. Note that the dimensions are not small enough to have a strong quantum confinement effect, such as a large exciton binding energy, since the NW thickness is in the order of a few hundred nm and no excitonic band is observed in Figure 3.2. Nevertheless, the trapped carriers in these Se nanowires exhibit such a long lifetime, as measured by NFP, that they can advance and be collected via hopping transport before they annihilate. This is beneficial for the use of Se-NWs in optoelectronic devices and is at the heart of the fiber-integrated device performance W. Yan et al. have demonstrated in a recent work.¹³

Fluence / mJ cm^{-2}	τ_1 / μs	τ_2 / μs
83	1.2 ± 0.04	4.6 ± 0.12
123	0.73 ± 0.02	3.8 ± 0.04
211	0.69 ± 0.01	3.7 ± 0.02

Table 3.2: Fluence-dependent fits for the NFP measurements.

3.2.3 Charge carrier mobility

Next, we studied the carrier mobility of the nanowire network. The TRTS measurements were additionally used to calculate the short-range mobility of charge carriers. Indeed, TRTS probes the intrinsic mobility on a short length scale, typically <100 nm, due to the short duration of the electric field cycle.²⁵ The frequency-averaged photoconductivity $\Delta\sigma$ was obtained using the maximum electric field point of the single-cycle THz pulse following

$$\Delta\sigma = -\frac{(n_{air} + n_{HDPE})\varepsilon_0 c \Delta E}{L E}, \quad (3.1)$$

where n_{air} and n_{HDPE} are the refractive indices of air and the HDPE (completely transparent to our broadband THz pulse) substrate, respectively; ε_0 is the free space permittivity; c is the speed of light; and ΔE is the photoinduced change in the transmitted THz electric field while E is the initial one. Lastly, L is the sample thickness. Here, we consider an effective thickness (L_e) corresponding to a compact film of t-Se nanowires, in order to obtain an average mobility over the probed ensemble. The average mobility can then be calculated with³⁹

$$\mu = \frac{\Delta\sigma}{Ne}, \quad (3.2)$$

where N is the charge carrier density and e the elementary charge. In order to estimate N we assume complete photon to charge carrier conversion obtaining two carriers (electron and hole) per photon at time zero. Since the photoconductivity presents a very fast decay, being non-negligible within the time duration of the pump pulse, the peak signal has to be extracted. A straightforward method is to use the amplitudes of the exponential decays convoluted with Gaussians used for the fit (Section B.4).

Fluence / $\mu\text{J cm}^{-2}$	$f_{abs}N_p / \text{m}^{-2}$	$-\Delta E/E / -$	$\mu / \text{cm}^2 \text{V}^{-1} \text{s}^{-1}$
71	1.77×10^{18}	0.0305	3.60
142	3.31×10^{18}	0.041	2.59
227	5.30×10^{18}	0.0803	3.17
284	6.63×10^{18}	0.104	3.28
426	9.94×10^{18}	0.136	2.88
568	1.33×10^{19}	0.15	2.37

Table 3.3: Fluence-dependent TRTS measurements of carrier mobility.

These amplitudes correspond to the initial signal that would be observed after a delta function excitation pulse. N is calculated as $N = f_{abs}N_p\phi$, where f_{abs} is the absorptance measured with the integrating sphere, subtracting the amount of absorptance obtained at 850 nm to the one at λ_{exc} ; ϕ is the carrier generation yield that we assume to be equal to 2; and N_p is the average photon density on the sample volume (where L_e is present). Therefore, L_e cancels out in the calculation of μ , yielding it irrelevant within the approximations used. Taking advantage of the mobility measurements that do not progressively vary at different fluences we reach a value of $\mu = 2.98 \pm 0.42 \text{ cm}^2 \text{V}^{-1} \text{s}^{-1}$ (Table 3.3). This moderate value agrees with the approximately flat spectrum shown in the Appendix (Figure A.6). The mobility value obtained here for the Se nanowire network is much higher than that of a single Se nanowire synthesized by the hydrothermal technique measured using a contact probe technique.⁴⁰ The latter technique probes the mobility of carriers as they travel between two electrodes over long time scales. Thus, they have time to get trapped and scatter on different defects found along the way. On the contrary, in our TRTS measurements the carriers are probed over small distances before they equilibrate with defect and surface trapping states. The mobility obtained

here can therefore represent an upper limit for the Se nanowire network. Interestingly, the mobility value is higher than that of polycrystalline Se powders,²⁶ while it is lower than that of bulk Se single crystals.⁴¹ It should be noted that the current carrier mobility measured by TRTS is an average value for the Se nanowire network where each individual wire has a random orientation with respect to the electric field of the THz. However, even though experimental uncertainties and approximations can contribute to the differences, we believe that grain boundaries in polycrystalline samples, surface states and interconnections in nanowire samples, and crystal orientation can strongly affect carrier mobility.⁴² Indeed, the mobility must be higher along the helical chains of trigonal selenium than across them. Thus, bulk single crystals without grain boundaries, surface states, or interconnections, probed along the (001) orientation, exhibit the highest mobility. Finding ways to reduce the density of interconnections such as aligning the nanowire mesh via electric forces or thermal gradients would allow an increase in carrier mobility and therefore enhance device performance. This has been demonstrated by the work of W. Yan *et al.*, where engineering the number of defects in the Se nanowire network significantly improves the electronic and optoelectronic performance in terms of photoresponsivity, photosensitivity, and response speed.¹³ Surface passivation could also be exploited to unpin the Fermi level from the conduction band and therefore undermine surface scattering and yield enhanced carrier mobilities approaching bulk values,⁴ while reducing surface recombination.

3.3 Conclusions

In summary, we investigated the charge carrier dynamics and mobility of Se-NWs using a time-resolved contact-free and non-invasive approach, revealing picosecond-long free carrier lifetime and microsecond-long trapped carrier lifetime and a free carrier mobility of *ca.* $3.0 \text{ cm}^2 \text{ V}^{-1} \text{ s}^{-1}$. This mobility was calculated under the simplification of a compact film, knowing that it is a directional average and extrapolating the initial photoconductivity from the exponential fits. In addition, it is an average between electrons and holes. Furthermore, carriers were found to recombine via a trap-assisted recombination mechanism. In spite of a high density of surface states that influence carrier mobility, Se in the form of nanowires exhibits an excellent combination of efficient light absorption, long carrier lifetime, good mobility, easy synthesis, and processability, making them of interest for high-performance electronic and optoelectronic devices.

References

- (1) Yan, W.; Burgos-Caminal, A.; Das Gupta, T.; Moser, J.-E.; Sorin, F. Direct Synthesis of Selenium Nanowire Mesh on a Solid Substrate and Insights into Ultrafast Photocarrier Dynamics. *J. Phys. Chem. C* **2018**, *122*, 25134–25141.
- (2) Gudiksen, M. S.; Lauhon, L. J.; Wang, J.; Smith, D. C.; Lieber, C. M. Growth of Nanowire Superlattice Structures for Nanoscale Photonics and Electronics. *Nature* **2002**, *415*, 617–620.
- (3) Li, Y.; Qian, F.; Xiang, J.; Lieber, C. M. Nanowire Electronic and Optoelectronic Devices. *Mater. Today* **2006**, *9*, 18–27.
- (4) Xiang, J.; Lu, W.; Hu, Y.; Wu, Y.; Yan, H.; Lieber, C. M. Ge/Si Nanowire Heterostructures as High-Performance Field-Effect Transistors. *Nature* **2006**, *441*, 489–493.
- (5) Johnson, J. C.; Choi, H.-J.; Knutsen, K. P.; Schaller, R. D.; Yang, P.; Saykally, R. J. Single Gallium Nitride Nanowire Lasers. *Nat. Mater.* **2002**, *1*, 106–110.
- (6) Peter J. Pauzauskie; Peidong Yang Nanowire photonics. *Mater. Today* **2006**, *9*, 36–45.
- (7) Cui, Y.; Qingqiao Wei; Hongkun Park; Charles M. Lieber Nanowire Nanosensors for Highly Sensitive and Selective Detection of Biological and Chemical Species. *Science* **2001**, *293*, 1289–1292.
- (8) Nam, S.; Jiang, X.; Xiong, Q.; Ham, D.; Lieber, C. M. Vertically Integrated, Three-Dimensional Nanowire Complementary Metal-Oxide-Semiconductor Circuits. *PNAS* **2009**, *106*, 21035–21038.
- (9) Ren, L.; Zhang, H.; Tan, P.; Chen, Y.; Zhang, Z.; Chang, Y.; Xu, J.; Yang, F.; Yu, D. Hexagonal Selenium Nanowires Synthesized via Vapor-Phase Growth. *J. Phys. Chem. B* **2004**, *108*, 4627–4630.
- (10) Mayers, B. T.; Liu, K.; Sunderland, D.; Xia, Y. Sonochemical Synthesis of Trigonal Selenium Nanowires. *Chemistry of Materials* **2003**, *15*, 3852–3858.
- (11) Gates, B.; Mayers, B.; Cattle, B.; Xia, Y. Synthesis and Characterization of Uniform Nanowires of Trigonal Selenium. *Adv. Funct. Mater.* **2002**, *9*.

- (12) Kasap, S.; Frey, J. B.; Belev, G.; Tousignant, O.; Mani, H.; Greenspan, J.; Laperriere, L.; Bubon, O.; Reznik, A.; DeCrescenzo, G.; Karim, K. S.; Rowlands, J. A. Amorphous and Polycrystalline Photoconductors for Direct Conversion Flat Panel X-Ray Image Sensors. *Sensors* **2011**, *11*, 5112–5157.
- (13) Yan, W.; Qu, Y.; Gupta, T. D.; Darga, A.; Nguyễn, D. T.; Page, A. G.; Rossi, M.; Ceriotti, M.; Sorin, F. Semiconducting Nanowire-Based Optoelectronic Fibers. *Adv. Mater.* **2017**, *29*, 1700681.
- (14) Ray, C.; Dutta, S.; Sarkar, S.; Sahoo, R.; Roy, A.; Pal, T. A Facile Synthesis of 1D Nano Structured Selenium and Au Decorated Nano Selenium: Catalysts for the Clock Reaction. *RSC Adv.* **2013**, *3*, 24313.
- (15) Dong, H.; Quintilla, A.; Cemernjak, M.; Popescu, R.; Gerthsen, D.; Ahlswede, E.; Feldmann, C. Colloidally Stable Selenium@Copper Selenide Core@Shell Nanoparticles as Selenium Source for Manufacturing of Copper–Indium–Selenide Solar Cells. *J. Colloid Interface Sci.* **2014**, *415*, 103–110.
- (16) Deng, D. S.; Orf, N. D.; Danto, S.; Abouraddy, A. F.; Joannopoulos, J. D.; Fink, Y. Processing and Properties of Centimeter-Long, in-Fiber, Crystalline-Selenium Filaments. *Appl. Phys. Lett.* **2010**, *96*, 023102.
- (17) Yaman, M.; Khudiyev, T.; Ozgur, E.; Kanik, M.; Aktas, O.; Ozgur, E. O.; Deniz, H.; Korkut, E.; Bayindir, M. Arrays of Indefinitely Long Uniform Nanowires and Nanotubes. *Nat. Mater.* **2011**, *10*, 494–501.
- (18) Wang, C.; Hu, Q.; Wei, Y.; Fang, D.; Xu, W.; Luo, Z. Facile Fabrication of Selenium (Se) Nanowires for Enhanced Lithium Storage in Li-Se Battery. *Ionics* **2017**, *23*, 3571–3579.
- (19) Zhang, J.; Xu, Y.; Fan, L.; Zhu, Y.; Liang, J.; Qian, Y. Graphene–Encapsulated Selenium/Polyaniline Core–Shell Nanowires with Enhanced Electrochemical Performance for Li–Se Batteries. *Nano Energy* **2015**, *13*, 592–600.
- (20) Chaudhary, S.; Umar, A.; Mehta, S. Selenium Nanomaterials: An Overview of Recent Developments in Synthesis, Properties and Potential Applications. *Prog. Mater. Sci.* **2016**, *83*, 270–329.
- (21) Lingelbach, W.; Stuke, J.; Weiser, G.; Treusch, J. Temperature-Dependent Electroabsorption on the Indirect Edge of Trigonal Selenium. *Phys. Rev. B* **1972**, *5*, 243–253.

- (22) Matsui, M. Role of Interchain Interaction in Determining the Band Gap of Trigonal Selenium: A Density Functional Theory Study with a Linear Combination of Bloch Orbitals. *J. Phys. Chem. C* **2014**, *118*, 19294–19307.
- (23) Rai, R. C. Analysis of the Urbach Tails in Absorption Spectra of Undoped ZnO Thin Films. *J. Appl. Phys.* **2013**, *113*, 153508.
- (24) Tutihasi, S.; Chen, I. Optical Properties and Band Structure of Trigonal Selenium. *Phys. Rev.* **1967**, *158*, 623.
- (25) Ulbricht, R.; Hendry, E.; Shan, J.; Heinz, T. F.; Bonn, M. Carrier Dynamics in Semiconductors Studied with Time-Resolved Terahertz Spectroscopy. *Rev. Mod. Phys.* **2011**, *83*, 543–586.
- (26) Joyce, H. J.; Boland, J. L.; Davies, C. L.; Baig, S. A.; Johnston, M. B. A Review of the Electrical Properties of Semiconductor Nanowires: Insights Gained from Terahertz Conductivity Spectroscopy. *Semicond. Sci. Technol.* **2016**, *31*, 103003.
- (27) Johnston, M. B.; Herz, L. M. Hybrid Perovskites for Photovoltaics: Charge-Carrier Recombination, Diffusion, and Radiative Efficiencies. *Acc. Chem. Res.* **2016**, *49*, 146–154.
- (28) Manser, J. S.; Kamat, P. V. Band Filling with Free Charge Carriers in Organometal Halide Perovskites. *Nat. Photonics* **2014**, *8*, 737–743.
- (29) Knab, J. R.; Lu, X.; Vallejo, F. A.; Kumar, G.; Murphy, T. E.; Hayden, L. M. Ultrafast Carrier Dynamics and Optical Properties of Nanoporous Silicon at Terahertz Frequencies. *Opt. Mater. Express, OME* **2014**, *4*, 300–307.
- (30) Zheng, K.; Žídek, K.; Abdellah, M.; Chen, J.; Chábera, P.; Zhang, W.; Al-Marri, M. J.; Pullerits, T. High Excitation Intensity Opens a New Trapping Channel in Organic–Inorganic Hybrid Perovskite Nanoparticles. *ACS Energy Lett.* **2016**, *1*, 1154–1161.
- (31) Bouduban, M. E. F.; Burgos-Caminal, A.; Ossola, R.; Teuscher, J.; Moser, J.-E. Energy and Charge Transfer Cascade in Methylammonium Lead Bromide Perovskite Nanoparticle Aggregates. *Chem. Sci.* **2017**, *8*, 4371–4380.
- (32) Aleithan, S. H.; Livshits, M. Y.; Khadka, S.; Rack, J. J.; Kordesch, M. E.; Stinaff, E. Broadband Femtosecond Transient Absorption Spectroscopy for a CVD MoS₂ Monolayer. *Phys. Rev. B* **2016**, *94*, 035445.

- (33) Lou, Y.; Chen, X.; Samia, A. C.; Burda, C. Femtosecond Spectroscopic Investigation of the Carrier Lifetimes in Digenite Quantum Dots and Discrimination of the Electron and Hole Dynamics via Ultrafast Interfacial Electron Transfer †. *J. Phys. Chem. B* **2003**, *107*, 12431–12437.
- (34) Cooper, W. C., *The Physics of Selenium and Tellurium: Proceedings of the International Symposium Held at Montreal, Canada October 12–13, 1967*; Elsevier: 1969; 391 pp.
- (35) Roberts, G. G.; Tutihasi, S.; Keezer, R. C. Optical Absorption Edge of Trigonal Selenium. *Phys. Rev.* **1968**, *166*, 637–643.
- (36) Shockley, W.; Read Jr, W. T. Statistics of the Recombinations of Holes and Electrons. *Phys. Rev.* **1952**, *87*, 835.
- (37) Bhaskar, P.; Achtstein, A. W.; Diedenhofen, S. L.; Siebbeles, L. D. A. Mobility and Decay Dynamics of Charge Carriers in One-Dimensional Selenium van der Waals Solid. *J. Phys. Chem. C* **2017**, *121*, 18917–18921.
- (38) Uhd Jepsen, P.; Schairer, W.; Libon, I. H.; Lemmer, U.; Hecker, N. E.; Birkholz, M.; Lips, K.; Schall, M. Ultrafast Carrier Trapping in Microcrystalline Silicon Observed in Optical Pump–Terahertz Probe Measurements. *Appl. Phys. Lett.* **2001**, *79*, 1291–1293.
- (39) Wehrenfennig, C.; Liu, M.; J. Snaith, H.; B. Johnston, M.; M. Herz, L. Charge-Carrier Dynamics in Vapour-Deposited Films of the Organolead Halide Perovskite $\text{CH}_3\text{NH}_3\text{PbI}_{3-x}\text{Cl}_x$. *Energy Environ. Sci.* **2014**, *7*, 2269–2275.
- (40) Liao, Z.-M.; Hou, C.; Zhao, Q.; Liu, L.-P.; Yu, D.-P. Gate Tunable Photoconductivity of p-Channel Se Nanowire Field Effect Transistors. *Appl. Phys. Lett.* **2009**, *95*, 093104.
- (41) Mort, J. Transient Photoconductivity in Trigonal Selenium Single Crystals. *J. Appl. Phys.* **1968**, *39*, 3543–3549.
- (42) Baxter, J. B.; Schmuttenmaer, C. A. Conductivity of ZnO Nanowires, Nanoparticles, and Thin Films Using Time-Resolved Terahertz Spectroscopy. *J. Phys. Chem. B* **2006**, *110*, 25229–25239.

Chapter 4

Hot carrier dynamics in bulk lead halide perovskites

In this chapter, the advantages of the TRTS setup begin to be exploited. Short lived dynamics are observed and spectra are taken into account. In addition, a complex kinetic model for the dynamics is developed. It is based on the paper *Hot carrier mobility dynamics unravel competing sub-ps processes in lead halide perovskites*.¹ The contributions from collaborating coauthors is acknowledged. Juan M. Moreno-Naranjo and Aurélien R. Willauer participated as masters students in the preparation of preliminary samples and in several measurements. Arun A. Paraecattil and Ahmad Ajdarzadeh participated in early setup development. In addition, Arun A. Paraecattil and Linfeng Pan obtained SEM pictures. The chapter is centered on the processes happening at the very first ps after excitation with a special focus on carrier cooling and polaron formation. TRTS is applied in order to better understand the carrier nature and evolution in LHPs. The early charge carrier dynamics are explored for bulk perovskites of different compositions. An increase of the carrier mobility is observed that can initially be assigned to carrier cooling. However, fluence and wavelength analysis allows to discern a competition of processes where polaron formation plays an important role.

4.1 Introduction

Lead halide perovskites (LHPs) have attracted much attention in recent years due to the outstanding photovoltaic performances of thin film solar cells based on these materials combined with their facile processability.^{2,3} These advantages have encouraged many groups to seek a detailed understanding of the charge carrier and quasiparticle dynamics that govern the observed performances. Two of the main factors behind the large power conversion efficiencies are generally agreed to be a) slow recombination of photogenerated charge carriers⁴ and b) a relatively large carrier mobility.⁵ In combination, these two properties give rise to long diffusion lengths extending over micrometers⁶ and consequently allow for efficient charge extraction in submicron thin films.

The recombination rates in LHPs are, indeed, up to four orders of magnitude slower than those predicted from Langevin theory for a direct semiconductor.⁷ The reason behind this property is still an active topic of debate. One possibility that is gaining acceptance is that the carriers have a polaronic nature.⁸ The polar character of the lattice screens the Coulomb potential of photogenerated charges, which then experience reduced scattering with other charges and lattice defects.^{8,9} This effect should slow down not only recombination but also charge carrier cooling in comparison to bare charges.¹⁰ Because of two counteracting phenomena, predicting whether the polaron formation produces an increase or a decrease in the observed carrier mobility is difficult. On the one hand, the lattice deformation associated with the polaron should produce a heavier effective mass. On the other hand, the dynamic screening of the Coulomb potential upon the formation of a large polaron will hinder the scattering of charges with lattice defects.⁸ Meanwhile, hot carriers can undergo additional carrier-carrier scattering at high temperature and density, which can be screened upon polaron formation.¹⁰ Therefore, time-resolved mobility measurements, such as those obtained through TRTS, can be a useful way of detecting and defining the effects of polaron formation and scrutinizing the hot carrier dynamics. Several spectroscopic studies of hot photocarriers have recently been reported¹¹⁻¹⁵ along with theoretical studies focusing on the slow rate of this cooling.^{16,17} The time evolution of hot carriers is of particular interest in view of the possibility of realizing photovoltaic cells with conversion efficiencies exceeding the Shockley-Queisser limit. Indeed, several studies have reported long hot carrier lifetimes up to tens of pi-

cooseconds, opening the way to extracting them at selective contacts.¹⁸

When studying early charge carrier dynamics, a good time resolution is essential to reach meaningful conclusions with the application of mathematical models. This time resolution can be achieved in TRTS using an ultra-broadband THz single-cycle pulse generated with a two-color plasma technique.¹⁹ In our case, such a pulse includes frequencies from 1 to 20 THz, allowing for a pulse duration as short as 200 fs instead of the ~ 1 ps pulse typically obtained by optical rectification in solid semiconductors (see the THz spectrum and pulse shape in Figure 2.2). This can help to overcome the artifacts that may appear in classical TRTS on the sub-ps dynamics.¹⁹ The use of ultra-broadband pulses poses, however, the difficulty of finding the right substrate with full transparency. Various approaches have been used in the past, such as employing Si wafers²⁰ and diamond as thin film substrates,²¹ or using single-crystals in reflectance mode.^{22,23} The latter substrates, however, either give rise to strongly modulated absorption spectra and pose an excessive experimental and analytical complexity or are too costly. In addition, it is of interest to study the perovskite response in a state close to that of a working optoelectronic device. Thus, we measured polycrystalline thin films, once again grown on HDPE, in a transmission configuration.

4.2 Results and analysis

4.2.1 Sample

Thin films of LHPs composed of various anions and cations were obtained on 1 mm HDPE sheets through a spin-coating procedure, identical to that generally used on glass or similar supports. When spin-coating solutions to form LHP thin films, one of the key parameters, and the one that mainly varies between HDPE and glass, is the wettability of the surface to the polar solvent (DMSO). HDPE is an apolar material that repels polar solvents, making the spin-coating technique impracticable. Indeed, the spin-coating technique is based on the formation of a thin film of solution when a spinning force is applied. However, if poor interaction occurs between the solvent and the substrate, the solution just slips off. To solve this issue, a surface treatment must be applied to the HDPE surface to endow it with a polar nature. This nature was achieved through an oxidative plasma treatment. Such an approach generates oxidation products on the

surface of the polymer that constitute polar groups, highly increasing the wettability to polar solvents.²⁴ The resulting LHP films are polycrystalline, with grains on the order of 100 nm (see Appendix, Figure A.7), and have photophysical properties similar to the films prepared on other substrates. This can be seen with the absorption and emission spectra shown in Figure 4.1. Furthermore, all ultrafast measurements focus on the first ps, before surface recombination becomes really important.

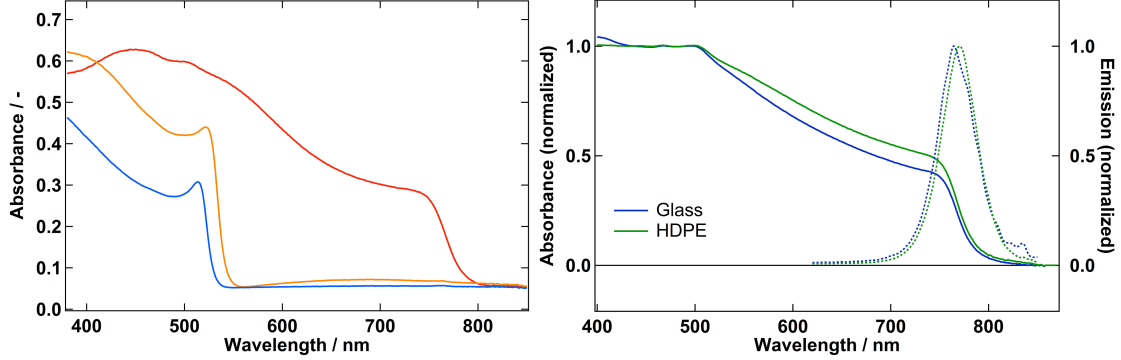


Figure 4.1: Left) Absorbance of the samples of three different compositions on HDPE, namely, $\text{CH}_3\text{NH}_3\text{PbI}_3$ (red), $\text{CH}_3\text{NH}_3\text{PbBr}_3$ (yellow) and CsPbBr_3 (blue). Right) Absorbance (solid line) and emission (dashed line) of $\text{CH}_3\text{NH}_3\text{PbI}_3$ on glass (blue) and on HDPE (green). Both are found to be very similar. The variations are smaller than what can be found for the same substrate.

4.2.2 A slow rise of the TRTS signal

In this chapter, we aim to study the relationship between carrier-lattice interactions and carrier cooling from a mobility perspective using TRTS. Such a study can be achieved by exploiting the sensitivity of THz radiation transmission to the carrier mobility. In an optical pump-THz probe experiment applied to a semiconductor material, the pump generates charge carriers that absorb the incident THz probe pulse. The THz radiation absorbance is generally reported as the negative of the ratio between the change in the modulus of the THz electric field (ΔE) upon transmission through the sample and the modulus of the incident field (E). In the case of thin films, when $\Delta E \ll E$, this ratio can be shown to be proportional to the photoconductivity ($\Delta\sigma$) generated by the photogenerated carriers, which is itself proportional to the carrier density (N) and the

carrier mobility (μ)^{25,26}

$$-\frac{\Delta E}{E} \propto \Delta\sigma = \mu e N. \quad (4.1)$$

An evolution of the THz absorptance of the sample must therefore be associated with a change in either N or μ . With this in mind, we determined the early carrier dynamics of three LHP thin films of various compositions, namely, $\text{CH}_3\text{NH}_3\text{PbI}_3$, $\text{CH}_3\text{NH}_3\text{PbBr}_3$, and CsPbBr_3 , using ultra-broadband TRTS. Figure 4.2 shows the charge carrier photoconductivity dynamics measured during the first picoseconds following photoexcitation at different pump wavelengths of a $\text{CH}_3\text{NH}_3\text{PbI}_3$ thin film deposited on HDPE. At resonant photon energies, a fast rise can be observed while, above resonant energies, a second slower rise becomes increasingly apparent with increasing excitation energy.

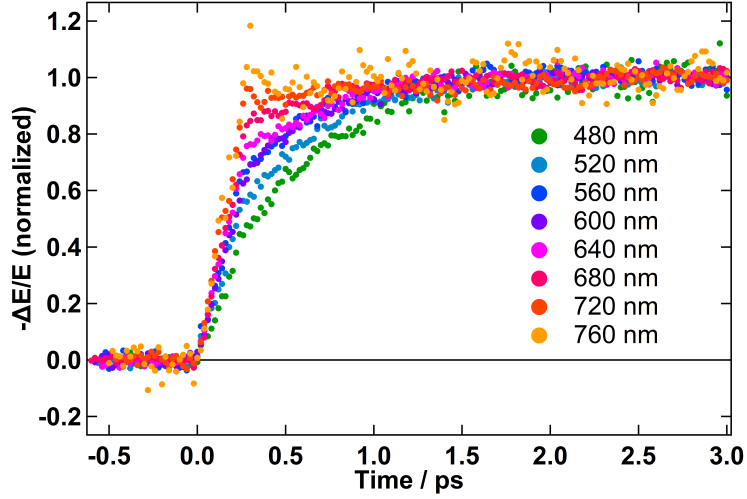


Figure 4.2: Excitation wavelength dependence of the early photoconductivity dynamics in $\text{CH}_3\text{NH}_3\text{PbI}_3$ thin films as probed by ultra-broadband TRTS for carrier densities above 10^{18} cm^{-3} at *ca.* $30 \mu\text{J cm}^{-2}$. The decrease in photon number is compensated by the increased absorption at higher energies (See the absorbance spectrum in Figure 4.1). The terahertz absorptance $-\Delta E/E$ is directly proportional to the photoconductivity $\Delta\sigma$.

It is worth noting that these measurements were carried out focusing on the point of highest electric field of the THz pulse. This approach is valid if the $\Delta E(t)$ waveform is

not phase-shifted with respect to the initial pulse. In order to verify this point, we obtained a 2D map of the different $\Delta E(t)$ waveforms and the corresponding $-\Delta E(\omega)/E(\omega)$ spectra. As seen in Figures A.9 and 4.3, the slower rise is coming mainly from a change in amplitude. However, the spectral response is not trivial and cannot be assigned to a simple model such as Drude or Drude-Smith.²⁷ Nonetheless, the response rises quite uniformly on the 5 to 12 THz range, where most of the THz probe is located. Thus, we can use the frequency-averaged response following the maximum at $t = 0$ in Figure 4.3 (left), as a general probe of the photoconductivity evolution. This allows one to carry out measurements in many different conditions of pump wavelength and fluence without the need to obtain costly 2D maps.

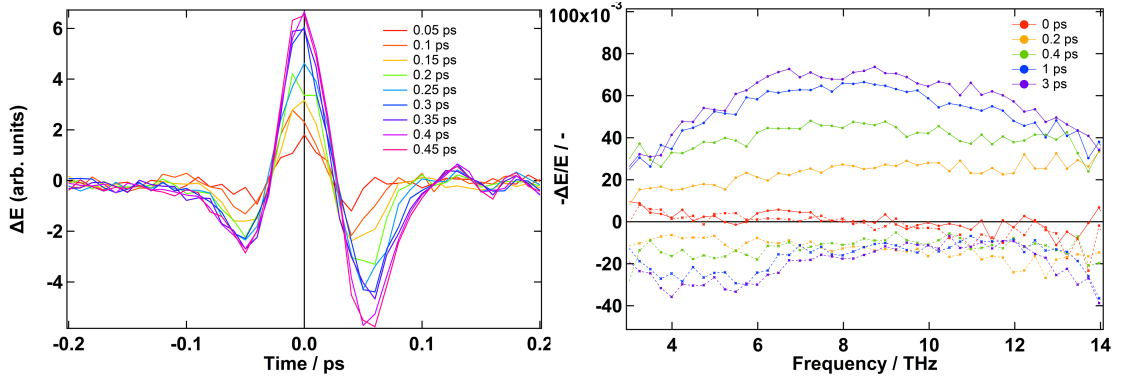


Figure 4.3: Time-resolved $\Delta E(t)$ (left) and $-\Delta E(\omega)/E(\omega)$ (right, Solid lines for Re and dashed for Im) obtained on $\text{CH}_3\text{NH}_3\text{PbI}_3$ at different pump-probe delay times ($\lambda_{\text{exc}} = 510$ nm, $F = 62 \mu\text{J cm}^{-2}$). The changes can be assigned mainly to a change in amplitude and not a change in phase. This allows one to follow the dynamics at this point.

Returning to the results in Figure 4.2, in terms of Equation 4.1, the fast initial rise can be assigned to an increase in the carrier density N upon photoexcitation, mixed with the initial steps of carrier evolution such as thermalization,²⁸ coherence loss,²⁹ the development of many body interactions,²¹ and, perhaps, the initial steps of carrier cooling. Although the time resolution of our setup can be expected to be shorter than this rise we are unable to distinguish between the different processes. In addition, this rise can be well fitted to the convolution of an instantaneous rise with a Gaussian having

a FWHM of 200 fs (See Appendix, Figure A.10). Therefore, hereon the data will be treated as having a time resolution limit of 200 fs. On the other hand, the latter rise can be more easily related to hot carrier evolution affecting the mobility μ . Such behavior of the mobility has been previously reported, *e.g.*, for GaAs³⁰ or perovskites,^{13,31} and is generally associated with the formation of hot charge carriers at different positions of the band structure $\epsilon(k)$ away from the bandgap threshold (Figure 4.4). This behavior is due to the relation between the mobility, effective mass and band curvature. Indeed, the mobility μ inversely depends on the effective mass m^* , while m^* in turn inversely depends on the band curvature ρ .³² In a simplified one-dimensional approximation, the carrier mobility μ is then proportional to the band curvature ρ and the scattering time τ so that

$$\mu = e\tau \frac{1}{m^*} = e\tau \frac{1}{\hbar^2} \frac{\partial^2 \epsilon}{\partial k_j^2} = \frac{e}{\hbar^2} \tau \rho. \quad (4.2)$$

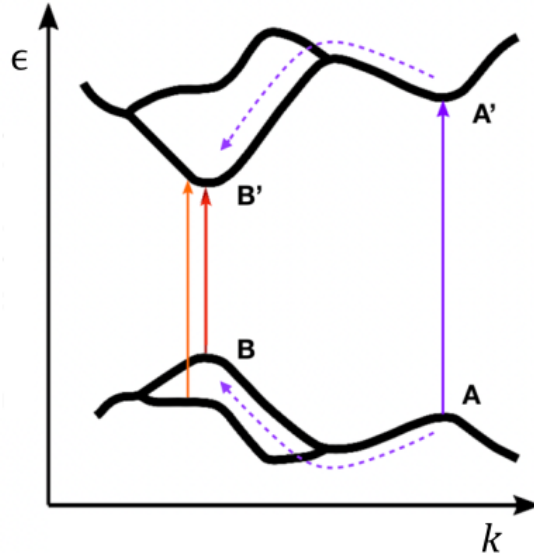


Figure 4.4: Simplified band structure scheme based on ref. [33]. Direct transitions occurring at $\lambda_{\text{exc}} = 800\text{nm}$ (red), $\lambda_{\text{exc}} = 600\text{nm}$ (orange) and $\lambda_{\text{ex}} = 400\text{nm}$ (purple) are represented by vertical arrows. The dashed arrows represent a cooling pathway of photocarriers generated upon excitation at $\lambda_{\text{exc}} = 400\text{nm}$.

Figure 4.4 displays a simplified band structure of $\text{CH}_3\text{NH}_3\text{PbI}_3$, where the spin-orbit

coupling has been omitted for the sake of simplification.³³ In such a situation, carriers photogenerated upon excitation in the blue region experience a significantly lower curvature of both the conduction and valence bands (positions A and A'). Hence, they must be characterized by a larger effective mass (m^*) and a lower mobility (μ) compared to carriers photogenerated upon excitation in the red region (positions B and B'). In addition, calculations suggest that a loss of parabolicity occurs as close as one-third from the minimum point along any direction (Figure 4.4).³³ This loss produces a decrease in mobility for the carriers higher up in the valley.^{34,35} Thus, relatively small excess energies already produce a noticeable decrease in the initial average mobility μ even though no carriers are located in different valleys.

4.2.3 Simple model

From a simple perspective, the observation of the slower rise in the THz absorptance over time can initially be assigned to intravalley relaxation and intervalley scattering of hot carriers with phonons towards the bottom of the valley where the effective mass accounts for the maximum mobility. In order to model such a process, we first consider a simple situation with low mobility hot carrier (N_H) and high mobility cold carrier (N_C) populations. This simplified model (see details in the Appendix, Section B.5) gives rise to a single exponential time profile of the transient photoconductivity signal

$$S(t) = 1 - Be^{-t/\tau}, \quad (4.3)$$

where B is the amplitude and τ is the lifetime. In such a simplified model, carriers can only be either hot or cold. However, a distribution of carriers with different excess energies and, thus, mobilities characterized by a certain temperature exists in reality. In addition, one should consider the possibility of polaron formation. Despite its limitation, fitting this initial simple model can be useful in evaluating the lifetime of the process involved. It can be said that parameter B in Equation 4.3 is a measure of the average mobility of the ensemble with respect to the final situation. A convolution with a Gaussian of FWHM w accounting for the instrument response function (IRF) can be used to fit the data (see Appendix, Equations B.33 and B.34). The results of the data fitting shown in Figure 4.2, with different measurements at different pump wavelengths (λ), are found in Table 4.1. Due to the initial rise previously explained, the value of the FWHM w is also fitted. We repeatedly obtain values of *ca.* 200 fs.

$\lambda_{\text{exc}} / \text{nm}$	$B / -$	τ / ps	w / ps
480	0.78 ± 0.05	0.5 ± 0.02	0.17 ± 0.04
520	0.63 ± 0.02	0.46 ± 0.01	0.2 ± 0.01
560	0.51 ± 0.03	0.39 ± 0.02	0.18 ± 0.01
600	0.48 ± 0.02	0.41 ± 0.01	0.22 ± 0.01
640	0.38 ± 0.02	0.44 ± 0.02	0.19 ± 0.01
680	0.22 ± 0.02	0.45 ± 0.03	0.21 ± 0.01

Table 4.1: Results for the fitting of the simple exponential model at different pump wavelengths (λ_{exc}) for $\text{CH}_3\text{NH}_3\text{PbI}_3$. The fit traces are shown in Figure A.11.

As expected, the amplitude B increases with excess energy owing to the higher initial concentration of hot carriers. Surprisingly, however, the lifetimes from the measurements are fairly constant in the 480-680 nm excitation wavelength range, with values between 400 and 500 fs. Above 680 nm, the rise is almost negligible. The lack of an increase in the lifetime is surprising if we assign it to carrier cooling, as the higher the initial carrier temperature is, the longer cooling down should generally take.¹⁴ If the THz absorption is a direct probe of the average carrier temperature, then this would indeed be the case. However, the exponential fits with a constant lifetime indicate a different process that links high and low mobility carriers. The relaxation of hot charge carriers includes two initial steps: a) thermalization, in which the hot carriers equilibrate towards a Fermi-Dirac distribution, characterized by a certain temperature higher than that of the lattice, and b) cooling, in which the hot carriers interact with the lattice through carrier-phonon inelastic scattering with longitudinal optical (LO) phonons to shed their extra energy.¹⁸ The former step has been reported to occur in the 10 to 100 fs interval,²⁸ below the initial rise, while the latter step can actually be studied with TRTS. LO phonons are considered to be involved not only in the relaxation of hot carriers¹⁴ but also in polaron formation.³⁶ Recently, time-resolved spectroscopy techniques other than TRTS have revealed that the polaron formation time for LHPs is on the order of hundreds of fs.³⁶ In ref. [36], the perovskites under study were $\text{CH}_3\text{NH}_3\text{PbBr}_3$ and CsPbBr_3 . For these materials, we obtained, on average, low mobility lifetimes of 320 and 650 fs, very close to the reported polaron formation times of 290 and 700 fs,

respectively. Note that these lifetimes are subject to a certain variability depending on the sample. Interestingly, for some of the measurements reported in the literature, the observed process did not involve any cooling since a resonant excitation was used.

A recent publication reported a direct observation of polaron formation with TRTS.¹³ Surprisingly, the authors observe a delayed rise of the photoconductivity, which is assigned to polaron formation. A rise that we do not observe on the frequency-averaged photoconductivity at resonant conditions. It is unclear whether this comes from a delayed response at lower frequencies or due to a lower time resolution in optical rectification based TRTS setups. From our 2D maps it does seem that a delayed rise can be observed at frequencies lower than 2.5 THz (See Appendix, Figure A.12) and it coincidentally is of the same order as the reported polaron formation times. Furthermore, broadband TRTS based on gas photonics has recently been used to investigate the early dynamics on single-crystal $\text{CH}_3\text{NH}_3\text{PbI}_3$ samples in reflectivity mode upon resonant pumping.²³ In the latter study, a coherent oscillation is reported in the pump-probe dynamics mixed with a rise in the photoconductivity. It was also observed that this rise becomes longer at lower frequencies. Interestingly, a deeper analysis of the probe frequency dependence of the oscillations allows to relate both phenomena to the formation of polarons. Such polaron formation is found to originate from the coupling to a single LO phonon mode at 3.7 THz. Unfortunately, we are unable to observe such clear oscillations and their dependency on probe frequency. This can be explained by the apparent lower sensitivity of our setup and the nature of our samples. Single crystals with a fixed orientation might enhance this kind of responses. Nonetheless, there is a change in the photoconductivity spectrum occurring in the first hundreds of femtoseconds (See Appendix, Figure A.13). We may tentatively assign it to the formation of polarons because, from a Drude perspective, a change only in effective mass should only change the amplitude of the spectrum. The final spectrum shows a photoconductivity that rises for frequencies higher than *ca.* 3.7 THz. This may be caused by a different absorption of the THz waves above and below the coupled phonon frequency. A further in-depth study of the photoconductivity spectrum would be worth pursuing in the future. More evidence of polaron formation in TRTS was obtained by Cinquanta et al. by looking at the phonon modes below 2 THz on CsPbBr_3 nanocrystals.³⁷

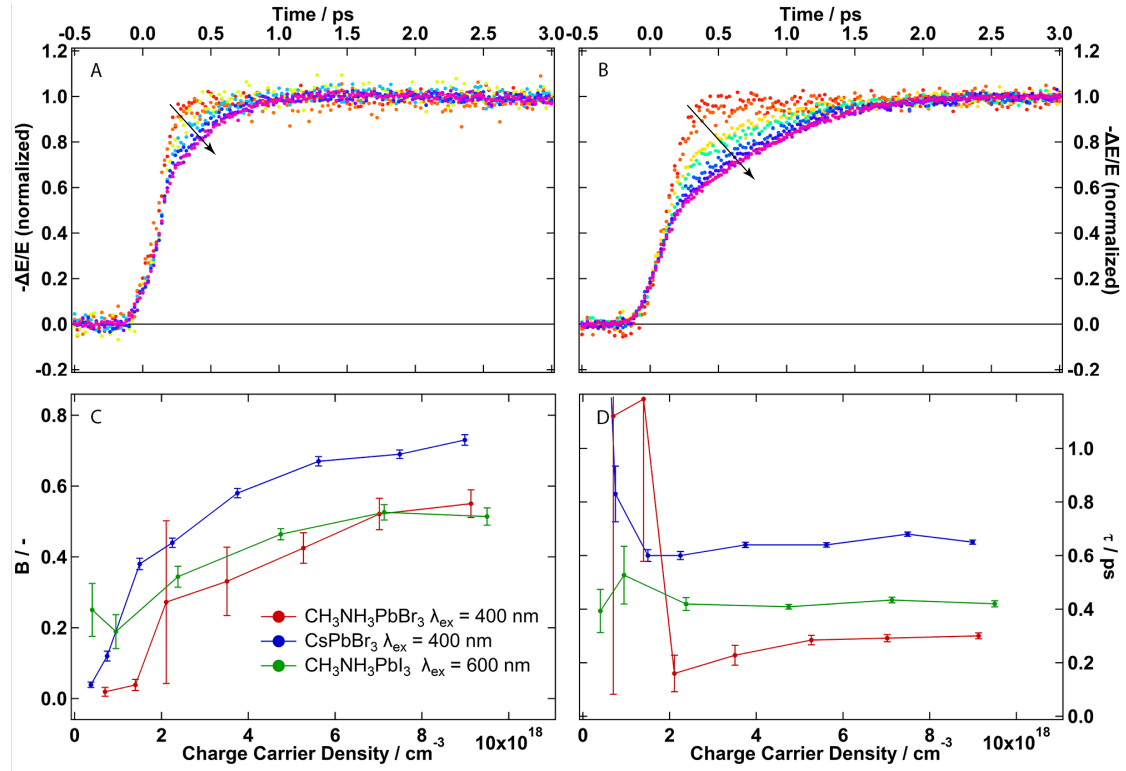


Figure 4.5: Fluence dependence of the rise in photoconductivity for A) $\text{CH}_3\text{NH}_3\text{PbBr}_3$ and B) CsPbBr_3 . Note that both materials present a similar fluence dependence, while the lifetime is noticeably longer in the fully inorganic material. The arrows indicate the rise in fluence. C) The amplitude, B , from the fit is shown to be the main parameter that varies with fluence, while D) the time constant τ saturates earlier. A similar behavior is found for $\text{CH}_3\text{NH}_3\text{PbI}_3$, as seen in C) and D).

4.2.4 Complex model

From the existing experimental evidence, polaron formation in the form of a dynamic screening process has been suggested to be in competition with carrier cooling.¹⁰ Indeed, this dynamic screening process could result in polaron formation with the observed lifetimes. In Figure 4.2, we show measurements for relatively high charge carrier densities, above 10^{18} cm^{-3} . At these densities, a slow cooling process is expected to be observed due to the phonon bottleneck typically observed in these materials.³⁸ Thus, if two competing processes occur, we can hypothesize that, at low densities, carrier cooling to the

lattice temperature is sufficiently fast to occur before polaron formation, while at higher densities, the opposite is true. To test this hypothesis, we perform fluence-dependent measurements, as shown in Figure 4.5.

Indeed, the data show an increase in the magnitude of the mobility rise with increasing fluence. Our data shows, nonetheless, that the formation of polarons does not produce a substantially large change in mobility if the carriers are already cold. When exciting the samples at resonant energies or at low fluences, the slower rise is not observed (Figures 4.2 and 4.5, and Figure A.14 in the Appendix). Thus, the frequency-averaged photoconductivity remains similar, while the spectrum suffers some change as previously mentioned. This result is intriguing because polaron formation should have mobility changes associated with it due to a) an increase in the effective mass while carrying the lattice deformation and b) a decrease in scattering with defects.⁸ These effects may compensate each other for cold carriers, leaving only a minor spectrum change that cancels out in the frequency-averaged dynamics. Moreover, the fact that a rise with the polaron formation lifetime is observed at high fluences over the bandgap indicates that the dynamic screening process does produce a substantial increase in the hot carrier mobility. The dynamic screening may possibly reduce the carrier-carrier scattering present at high carrier temperatures. Thus, the mobility would increase upon hot polaron formation, unlike with cold polaron formation. Furthermore, the hot polarons present a much slower cooling, which prevents us from observing any further dynamics due to the strong Coulomb screening of the lattice.^{10,39,40} We can thus propose the model depicted in Figure 4.6.

According to this model, hot carriers turn into cold ones through phonon emission. This step is considered reversible, introducing a hot phonon bottleneck. The phonons decay at a certain rate such that a phonon population builds up at high hot carrier densities, decreasing the overall rate of carrier cooling. In addition, this cooling process competes with the polaron formation process through dynamic screening. The latter process has a certain lifetime depending on the perovskite composition.

As the initial hot carrier density increases, the cooling process is slowed and hot polaron formation is favored, giving rise to very long hot (polaronic) carrier lifetimes. From our

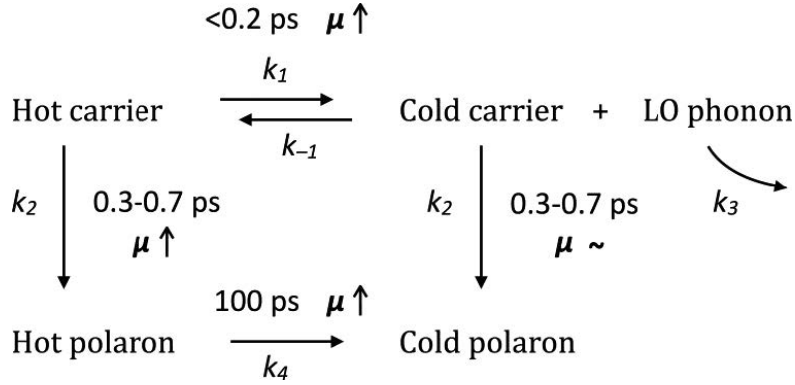


Figure 4.6: Cooling and dynamic screening competition model. The different processes induce a change in the mobility in the direction represented by the arrows next to μ . The carrier cooling and hot polaron formation processes induce a stronger increase in the mobility in the time window analyzed herein. LO phonons should also be produced upon polaron cooling. However, since this process occurs at longer times than the observed window, the model is simplified by ignoring this fact.

observations, we ascribe the strong increase in mobility to bare carrier cooling and hot polaron formation. Once again, we use a simplified model that does not consider carrier and phonon energy distributions with a certain temperature. Nonetheless, this model appreciably follows the excitation fluence and wavelength dependencies that we observe. We justify not using a temperature model¹⁴ by the fact that the function relating temperature and mobility is difficult to obtain and we can hardly assume that it is linear. Moreover, using such a model would overcomplicate the computation.

As shown in Figure 4.7, we can numerically solve the differential equations in the model in order to simulate the signal at different carrier densities (See details in Appendix, Section B.6). These results show the same trends as the measurements in Figure 4.5.A. Furthermore, a global fitting of several datasets can be carried out in which all the parameters are common except for the initial charge carrier concentration, which can be fixed to a value proportional to the relative fluence used. The good quality of the fits supports the general validity of the model, which follows the observed trend with fluence. Unfortunately, the complexity of the model prevents meaningful values from being

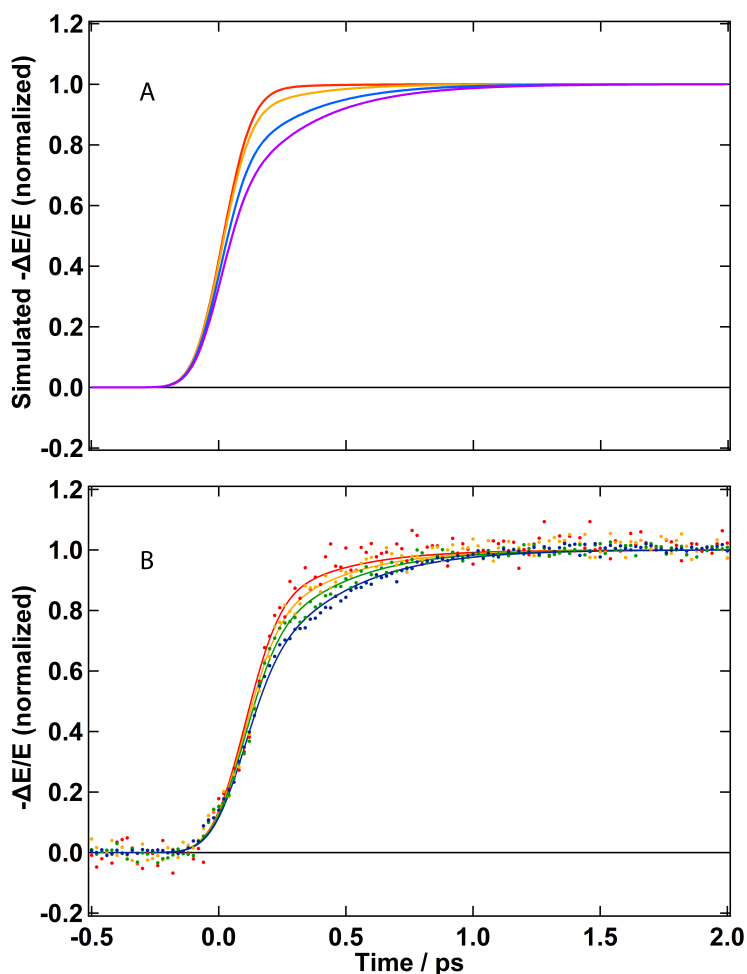


Figure 4.7: A) Simulated signals for $\text{CH}_3\text{NH}_3\text{PbBr}_3$ at different charge carrier densities following the model of Figure 4.6 (See details in Appendix, Section B.6). The slower rise becomes more apparent as the density is increased. B) Model global fittings to $\text{CH}_3\text{NH}_3\text{PbBr}_3$ data at $18 \mu\text{J}/\text{cm}^2$ (red), $31 \mu\text{J}/\text{cm}^2$ (yellow), $46 \mu\text{J}/\text{cm}^2$ (green), and $80 \mu\text{J}/\text{cm}^2$ (blue), where all parameters are common and the initial carrier density is proportional to the fluence multiplied by a common fitted value.

obtained for each parameter in free fits, and many of the parameters have to be prefixed and guessed. Nonetheless, the importance lies in the general behavior and trends with

fluence and wavelength that arise from the competing cooling and dynamic screening processes. The results of the fitting procedure are shown in Table 4.2. We obtain a time constant for polaron formation $1/k_2 = 0.4$ ps. Large values of the kinetic constants k_1 and k_{-1} are guessed, since the equilibrium between hot carriers, on the one hand, and cold carriers and LO phonons, on the other hand, (Figure 4.6) must be reached within the initial rise. The rate constants for phonon decay (k_3) and polaron cooling (k_4) are taken from the literature.^{10,14} The fitted value of the parameter $a = 0$ (See Appendix, Equation B.40) means that hot carriers do not contribute to the transient conductivity signal.

Parameter	Fitted value
a	0 ± 0.08
$N_{hc}(0)$	0.3 ± 0.07 adu
w	0.24 ± 0.005 ps
k_1	200 ps ⁻¹ (guessed)
k_{-1}	100 adu ⁻¹ ps ⁻¹ (guessed)
$k_{-1}N_{hc}(0)$	30 ± 7 ps ⁻¹
k_2	2.5 ± 0.15 ps ⁻¹
k_3	1.67 ps ⁻¹ (literature)
k_4	0.01 ps ⁻¹ (literature)

Table 4.2: Results of the global fitting of the complex model to experimental data as seen in Figure 4.7.B for CH₃NH₃PbBr₃. The parameter w stands for the FWHM of the convoluted Gaussian, a measure of the time resolution of the setup. The initial hot carrier density $N_{hc}(0)$ is given in arbitrary density units (adu). The same units are used in the dimensions of the second order rate constant k_{-1} .

Our results, observing the previously reported polaron formation times³⁶ at higher fluences ($> 10^{18}$ cm⁻³), come into contrast with the idea that polarons are destabilized at densities higher than the Mott density ($\sim 10^{18}$ cm⁻³) due to mutual interaction.¹⁰ The fact that we still observe the characteristic lifetime points to the fact that the process is still occurring. The destabilization may induce a decreased screening, increasing the cooling speed of hot polarons, as found by X. Zhu and co-workers,³⁹ but without

preventing the formation. Nonetheless, this cooling would still take place beyond our observed time window, involve the phonon bottleneck and compete with recombination. Indeed, this would be comparable to the recent observation of persistent excitons above the Mott density in $\text{CH}_3\text{NH}_3\text{PbBr}_3$ as Mahan excitons.⁴¹

4.2.5 Additional measurements

Further information on these materials can be extracted from a comparison between different compositions in terms of cations and anions. One key parameter is affected: the dynamic screening lifetime, upon which both anions and cations have an effect. CsPbBr_3 is the material presenting the longest lifetime, suggesting that the extra degrees of freedom from the organic cations play a role in speeding up the process. Last, low temperature measurements show an increase in the lifetime of the mobility rise accompanied by an increase in the total terahertz absorption (Figure 4.8). The latter phenomenon is known in LHPs, where the polaron mobility is limited by polaron-phonon scattering.²⁰ Thus, at lower temperatures, the mobility is higher due to the lower population of phonons. The former phenomenon indicates a role of the phonon density in the polaron formation process.

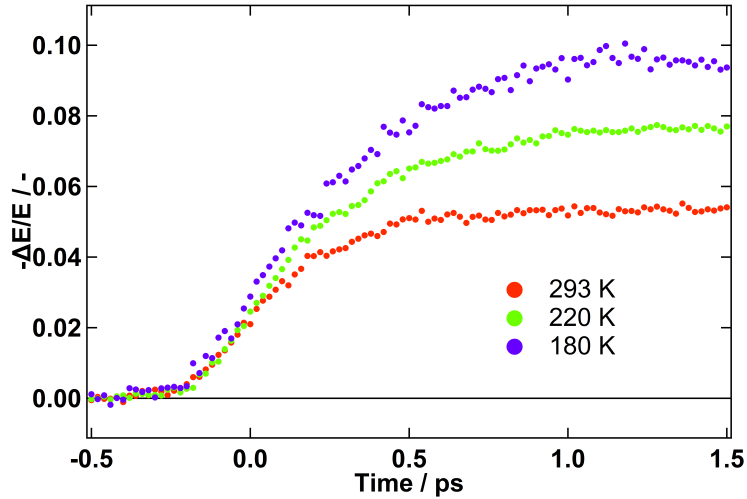


Figure 4.8: Low temperature measurements of the early dynamics of the THz absorptance in $\text{CH}_3\text{NH}_3\text{PbBr}_3$ ($\lambda_{\text{exc}} = 400 \text{ nm}$).

4.3 Conclusions

Hot carrier dynamics of LHPs of different compositions have been analyzed from a THz mobility perspective using ultra-broadband TRTS in transmission mode. This was achieved through the novel use of HDPE substrates treated with an oxidative plasma. The results are compatible with competing cooling and dynamic screening processes. A model was proposed and applied to explain the observed fluence dependence and constant lifetime of the mobility rise. In it, the previously reported phenomena of a phonon bottleneck and polaron formation through a dynamic screening process were unified. Particularly, polaron formation was found to produce a substantial change in mobility specifically for hot carriers. Furthermore, the composition was found to mainly affect the time constant of the dynamic screening process. In this regard, the Cs^+ inorganic cation was found to produce longer dynamic screening than its organic counterparts for a given halide composition. This result is probably due to a decrease in the degrees of freedom that allow for polarization of the lattice in the presence of a charge carrier. The model assumes that either both carriers have a similar mobility and behavior or one dominates. In addition, distributions characterized by a certain temperature are not taken into account due to uncertainties and to simplify the modeling process. Last, low temperature measurements hint at implications of the phonon densities in the dynamic screening process.

References

- (1) Burgos-Caminal, A.; Moreno-Naranjo, J. M.; Willauer, A. R.; Paraecattil, A. A.; Ajdarzadeh, A.; Moser, J.-E. Hot Carrier Mobility Dynamics Unravel Competing Sub-ps Cooling Processes in Lead Halide Perovskites. *arXiv:1909.04589 [cond-mat, physics:physics]* **2019**.
- (2) Correa-Baena, J.-P.; Abate, A.; Saliba, M.; Tress, W.; Jacobsson, T. J.; Grätzel, M.; Hagfeldt, A. The Rapid Evolution of Highly Efficient Perovskite Solar Cells. *Energy Environ. Sci.* **2017**, *10*, 710–727.
- (3) Best Research-Cell Efficiency Chart, Photovoltaic Research, NREL., <https://www.nrel.gov/pv/cell-efficiency.html> (accessed 11/18/2019).
- (4) Bi, Y.; Hutter, E. M.; Fang, Y.; Dong, Q.; Huang, J.; Savenije, T. J. Charge Carrier Lifetimes Exceeding 15 μ s in Methylammonium Lead Iodide Single Crystals. *J. Phys. Chem. Lett.* **2016**, *7*, 923–928.
- (5) Herz, L. M. Charge-Carrier Mobilities in Metal Halide Perovskites: Fundamental Mechanisms and Limits. *ACS Energy Lett.* **2017**, 1539–1548.
- (6) Stranks, S. D.; Eperon, G. E.; Grancini, G.; Menelaou, C.; Alcocer, M. J. P.; Leijtens, T.; Herz, L. M.; Petrozza, A.; Snaith, H. J. Electron-Hole Diffusion Lengths Exceeding 1 Micrometer in an Organometal Trihalide Perovskite Absorber. *Science* **2013**, *342*, 341–344.
- (7) Wehrenfennig, C.; Liu, M.; Snaith, H. J.; Johnston, M. B.; Herz, L. M. Charge-Carrier Dynamics in Vapour-Deposited Films of the Organolead Halide Perovskite $\text{CH}_3\text{NH}_3\text{PbI}_{3-x}\text{Cl}_x$. *Energy Environ. Sci.* **2014**, *7*, 2269–2275.
- (8) Zhu, X.-Y.; Podzorov, V. Charge Carriers in Hybrid Organic–Inorganic Lead Halide Perovskites Might Be Protected as Large Polarons. *J. Phys. Chem. Lett.* **2015**, *6*, 4758–4761.
- (9) Miyata, K.; Atallah, T. L.; Zhu, X.-Y. Lead Halide Perovskites: Crystal-Liquid Duality, Phonon Glass Electron Crystals, and Large Polaron Formation. *Sci. Adv.* **2017**, *3*, e1701469.
- (10) Joshi, P. P.; Maehrlein, S. F.; Zhu, X. Dynamic Screening and Slow Cooling of Hot Carriers in Lead Halide Perovskites. *Adv. Mater.* **2019**, 1803054.

- (11) Hedley, G. J.; Quarti, C.; Harwell, J.; Prezhdo, O. V.; Beljonne, D.; Samuel, I. D. W. Hot-Hole Cooling Controls the Initial Ultrafast Relaxation in Methylammonium Lead Iodide Perovskite. *Sci. Rep.* **2018**, *8*, 8115.
- (12) Price, M. B.; Butkus, J.; Jellicoe, T. C.; Sadhanala, A.; Briane, A.; Halpert, J. E.; Broch, K.; Hodgkiss, J. M.; Friend, R. H.; Deschler, F. Hot-Carrier Cooling and Photoinduced Refractive Index Changes in Organic–Inorganic Lead Halide Perovskites. *Nat. Commun.* **2015**, *6*, 8420.
- (13) Bretschneider, S. A.; Ivanov, I.; Wang, H. I.; Miyata, K.; Zhu, X.; Bonn, M. Quantifying Polaron Formation and Charge Carrier Cooling in Lead-Iodide Perovskites. *Adv. Mater.* **2018**, 1707312.
- (14) Fu, J.; Xu, Q.; Han, G.; Wu, B.; Huan, C. H. A.; Leek, M. L.; Sum, T. C. Hot Carrier Cooling Mechanisms in Halide Perovskites. *Nat. Commun.* **2017**, *8*, 1300.
- (15) Shen, Q.; Ripolles, T. S.; Even, J.; Ogomi, Y.; Nishinaka, K.; Izuishi, T.; Nakazawa, N.; Zhang, Y.; Ding, C.; Liu, F.; Toyoda, T.; Yoshino, K.; Minemoto, T.; Katayama, K.; Hayase, S. Slow Hot Carrier Cooling in Cesium Lead Iodide Perovskites. *Appl. Phys. Lett.* **2017**, *111*, 153903.
- (16) Frost, J. M.; Whalley, L. D.; Walsh, A. Slow Cooling of Hot Polarons in Halide Perovskite Solar Cells. *ACS Energy Lett.* **2017**, *2*, 2647–2652.
- (17) Madjet, M. E.; Berdiyrov, G. R.; El-Mellouhi, F.; Alharbi, F. H.; Akimov, A. V.; Kais, S. Cation Effect on Hot Carrier Cooling in Halide Perovskite Materials. *J. Phys. Chem. Lett.* **2017**, *8*, 4439–4445.
- (18) Li, M.; Fu, J.; Xu, Q.; Sum, T. C. Slow Hot-Carrier Cooling in Halide Perovskites: Prospects for Hot-Carrier Solar Cells. *Adv. Mater.* **2019**, *0*, 1802486.
- (19) Nienhuys, H.-K.; Sundström, V. Intrinsic Complications in the Analysis of Optical-Pump, Terahertz Probe Experiments. *Physical Review B* **2005**, *71*, 235110.
- (20) Karakus, M.; Jensen, S. A.; D’Angelo, F.; Turchinovich, D.; Bonn, M.; Cánovas, E. Phonon–Electron Scattering Limits Free Charge Mobility in Methylammonium Lead Iodide Perovskites. *J. Phys. Chem. Lett.* **2015**, *6*, 4991–4996.
- (21) Huber, R.; Tauser, F.; Brodschelm, A.; Bichler, M.; Abstreiter, G.; Leitenstorfer, A. How Many-Particle Interactions Develop After Ultrafast Excitation of an Electron-Hole Plasma. *Nature* **2001**, *414*, 286–289.

- (22) Valverde-Chávez, D. A.; Ponseca, C. S.; Stoumpos, C. C.; Yartsev, A.; Kanatzidis, M. G.; Sundström, V.; Cooke, D. G. Intrinsic Femtosecond Charge Generation Dynamics in Single Crystal $\text{CH}_3\text{NH}_3\text{Pb}_3$. *Energy Environ. Sci.* **2015**, *8*, 3700–3707.
- (23) Lan, Y.; Dringoli, B. J.; Valverde-Chávez, D. A.; Ponseca, C. S.; Sutton, M.; He, Y.; Kanatzidis, M. G.; Cooke, D. G. Ultrafast Correlated Charge and Lattice Motion in a Hybrid Metal Halide Perovskite. *Sci. Adv.* **2019**, *5*, eaaw5558.
- (24) Chai, J.; Lu, F.; Li, B.; Kwok, D. Y. Wettability Interpretation of Oxygen Plasma Modified Poly(methyl methacrylate). *Langmuir* **2004**, *20*, 10919–10927.
- (25) Dexheimer, S. L.; Baxter, J. B.; Schmuttenmaer, C. A. In *Terahertz Spectroscopy: Principles and Applications*; CRC Press: 2008.
- (26) Dexheimer, S. L.; Kaindl, R. A.; Averitt, R. D. In *Terahertz Spectroscopy: Principles and Applications*; CRC Press: 2008.
- (27) Ulbricht, R.; Hendry, E.; Shan, J.; Heinz, T. F.; Bonn, M. Carrier Dynamics in Semiconductors Studied with Time-Resolved Terahertz Spectroscopy. *Rev. Mod. Phys.* **2011**, *83*, 543–586.
- (28) Richter, J. M.; Branchi, F.; Camargo, F. V. d. A.; Zhao, B.; Friend, R. H.; Cerullo, G.; Deschler, F. Ultrafast Carrier Thermalization in Lead Iodide Perovskite Probed with Two-Dimensional Electronic Spectroscopy. *Nat. Commun.* **2017**, *8*, 376.
- (29) March, S. A.; Riley, D. B.; Clegg, C.; Webber, D.; Liu, X.; Dobrowolska, M.; Furdyna, J. K.; Hill, I. G.; Hall, K. C. Four-Wave Mixing in Perovskite Photovoltaic Materials Reveals Long Dephasing Times and Weaker Many-Body Interactions than GaAs. *ACS Photonics* **2017**, *4*, 1515–1521.
- (30) Beard, M. C.; Turner, G. M.; Schmuttenmaer, C. A. Transient Photoconductivity in GaAs as Measured by Time-Resolved Terahertz Spectroscopy. *Phys. Rev. B* **2000**, *62*, 15764–15777.
- (31) Monti, M.; Tao, S. X.; Staniforth, M.; Crocker, A.; Griffin, E.; Wijesekara, A.; Hatton, R. A.; Lloyd-Hughes, J. Efficient Intraband Hot Carrier Relaxation in the Perovskite Semiconductor $\text{Cs}_{1-x}\text{Rb}_x\text{SnI}_3$ Mediated by Strong Electron–Phonon Coupling. *J. Phys. Chem. C* **2018**, *122*, 20669–20675.

- (32) Kittel, C., *Introduction to Solid State Physics*, 5th; John Wiley & Sons, Inc.: 1976.
- (33) Filip, M. R.; Verdi, C.; Giustino, F. GW Band Structures and Carrier Effective Masses of $\text{CH}_3\text{NH}_3\text{PbI}_3$ and Hypothetical Perovskites of the Type APbI_3 : $\text{A} = \text{NH}_4, \text{PH}_4, \text{AsH}_4, \text{and SbH}_4$. *J. Phys. Chem. C* **2015**, *119*, 25209–25219.
- (34) Even, J.; Pedesseau, L.; Katan, C.; Kepenekian, M.; Lauret, J.-S.; Saponi, D.; Deleporte, E. Solid-State Physics Perspective on Hybrid Perovskite Semiconductors. *J. Phys. Chem. C* **2015**, *119*, 10161–10177.
- (35) Even, J.; Pedesseau, L.; Katan, C. Understanding Quantum Confinement of Charge Carriers in Layered 2D Hybrid Perovskites. *ChemPhysChem* **2014**, *15*, 3733–3741.
- (36) Miyata, K.; Meggiolaro, D.; Trinh, M. T.; Joshi, P. P.; Mosconi, E.; Jones, S. C.; Angelis, F. D.; Zhu, X.-Y. Large Polarons in Lead Halide Perovskites. *Sci. Adv.* **2017**, *3*, e1701217.
- (37) Cinquanta, E.; Meggiolaro, D.; Motti, S. G.; Gandini, M.; Alcocer, M. J. P.; Akkerman, Q. A.; Vozzi, C.; Manna, L.; De Angelis, F.; Petrozza, A.; Stagira, S. Ultrafast THz Probe of Photoinduced Polarons in Lead-Halide Perovskites. *Phys. Rev. Lett.* **2019**, *122*, 166601.
- (38) Yang, Y.; Ostrowski, D. P.; France, R. M.; Zhu, K.; van de Lagemaat, J.; Luther, J. M.; Beard, M. C. Observation of a Hot-Phonon Bottleneck in Lead-Iodide Perovskites. *Nat. Photonics* **2016**, *10*, 53–59.
- (39) Niesner, D.; Zhu, H.; Miyata, K.; Joshi, P. P.; Evans, T. J. S.; Kudisch, B. J.; Trinh, M. T.; Marks, M.; Zhu, X.-Y. Persistent Energetic Electrons in Methylammonium Lead Iodide Perovskite Thin Films. *J. Am. Chem. Soc.* **2016**, *138*, 15717–15726.
- (40) Zhu, H.; Miyata, K.; Fu, Y.; Wang, J.; Joshi, P. P.; Niesner, D.; Williams, K. W.; Jin, S.; Zhu, X.-Y. Screening in Crystalline Liquids Protects Energetic Carriers in Hybrid Perovskites. *Science* **2016**, *353*, 1409–1413.
- (41) Palmieri, T.; Baldini, E.; Steinhoff, A.; Akrap, A.; Kollár, M.; Horváth, E.; Forró, L.; Jahnke, F.; Chergui, M. Mahan Excitons in Room-Temperature Methylammonium Lead Bromide Perovskites. *Nat. Commun.* **2020**, *11*, 1–8.

Chapter 5

Exciton-carrier dynamics in lead halide 2D perovskites

In this last chapter, the intrinsic ultra-broadband TRTS capabilities are fully employed including the acquisition and analysis of 2D time-resolved photoconductivity spectra in combination with fluence dependent frequency-averaged dynamics and the use of complex kinetic models. It is based on a submitted paper under the title *Exciton-carrier dynamics in 2D perovskites*, with the participation of Etienne Socie in the experimental process and Marine Bouduban in the initial planning. It is centered around unraveling the dynamics of charge carriers and excitons in highly confined 2D lead halide perovskite systems. The main aim is to observe the transition from carriers to excitons using ultra-broadband TRTS and FLUPS while determining the importance of exciton-exciton interactions. In addition, a kinetic model is presented that can be used to explain the observations and compare between two different cation compositions.

5.1 Introduction

Lead halide perovskites (LHPs) have become a widely studied and applied family of semiconductors in the field of optoelectronics, especially towards the development of solar cells that can compete with well-established technologies. The current solar-to-energy conversion has been pushed beyond 25%¹ owing to the quick and continued improvements.²⁻⁵ One of the key limitations of this technology has been its stability with respect to ambient conditions such as temperature, light and, especially, humidity. To tackle this problem, one of the proposed solutions is to use 2D perovskites such as those of the Ruddlesden-Popper family to increase the stability with respect to moisture.^{6,7} Mixing compositions of 2D/3D LHPs has been shown to increase the stability while maintaining a good performance.^{8,9} These lower dimensionality perovskites are obtained by introducing larger cations into the precursor mix. In the perovskite structure, characterized by the formula ABX_3 , the A cation is a small cation that can fit in the center of the cube formed by every eight BX_6 octahedra (in this case B is Pb^{2+} and X is I^-). If the A cation is replaced by a large cation, such as phenethylammonium ($C_6H_5C_2H_4NH_3^+$ or PEA), then the 3D crystalline structure can no longer be formed. Instead, a layered structure consisting of PbI_6 octahedra on the same plane surrounded by the large cations is formed. This effectively produces a quantum confinement effect due to the thickness of the layer that greatly affects the electronic properties of the material. Variable stoichiometric proportions of small cations can be added to produce multilayered quasi-2D perovskites. These can be described as quantum wells of quantized thickness, depending on the number of layers. A general formula of $R_2A_{n-1}B_nX_{3n+1}$ can be defined for Ruddlesden-Popper 2D perovskites, where R is the large monovalent cation and n is the number of layers. However, it is of great difficulty to obtain phase-pure samples of multilayered 2D perovskites. Efforts towards this goal have been made for single crystals¹⁰ and thin films.¹¹

In such low-dimensionality systems, there is not only quantum confinement but also dielectric confinement due to the difference in the permittivity between the ionic perovskite layer and the bulky organic cation. These two effects enhance electron-hole correlations, increasing the binding energy (E_b) of excitons from tens of meV in 3D $CH_3NH_3PbI_3$ to hundreds of meV. Furthermore, the variations in E_b with the cation can be attributed

to the dielectric confinement due to the varying permittivity.¹²⁻¹⁴ Given the considerable E_b in 2D perovskites, it is safe to assume that photoexcitations will have a strong excitonic character. Nonetheless, it is possible to obtain solar cells out of at least the $n = 3$ composition.⁶

Charge carriers excited with excess energy are known as hot carriers and follow a characteristic evolution of their relaxation that varies with the material. Typically, upon photoexcitation, charge carriers are generated in a distribution that has to undergo a thermalization process before being described by Fermi-Dirac statistics as a thermal distribution. This process can take less than 85 fs in 3D perovskites.¹⁵ The charge carrier distribution is then characterized by a carrier temperature (T_c) which is higher than that of the lattice (T_l). Therefore, it subsequently cools down through phonon-carrier interactions until both temperatures converge. This initially occurs through optical phonon emission until the temperature reaches the energy of said phonons and, if necessary, then continues with the involvement of acoustic phonons. In LHPs, the longitudinal optical (LO) phonon energy lies below the thermal energy at room temperature. Hence, the involvement of acoustic phonons is negligible.¹⁶ When comparing hot carrier cooling between 2D and bulk perovskites, it has been found that the process occurs considerably faster in the confined perovskite, at least in colloidal suspensions.¹⁷ This was explained by taking into account the decreased Coulomb screening by the lattice due to the dielectric confinement. Indeed, the dielectric constant of the organic cation was recently found to significantly affect the cooling process.¹⁸ On the other hand, carrier cooling was found to be lengthened in perovskite nanoparticles, allowing the extraction of hot carriers.¹⁹ There is still uncertainty regarding the process of hot carrier generation and cooling and exciton formation, as well as whether hot excitons are formed. A direct probe of excitons is extremely useful to completely reveal the early dynamics in these systems. Two techniques that have the potential to selectively probe excitons are time-resolved photoluminescence through fluorescence upconversion spectroscopy (FLUPS) and time-resolved THz spectroscopy (TRTS). While the latter is typically used to selectively study charge carriers, it can also be used to identify excitons. This is achieved through the differentiated spectral responses of the two species.²⁰⁻²⁵ However, the studies carried out in the past on exciton formation using TRTS have been limited to the 0.5-3 THz range. This requires an E_b close to this range to observe distinct signatures, which demands the

use of cryogenic temperatures to stabilize the excitons. Here, we want to not only study the exciton-carrier dynamics of 2D perovskites but also demonstrate the capability of an ultra-broadband TRTS setup (up to 20 THz) to study excitons at room temperature. We combine this technique with FLUPS to further support our findings and observe the effect produced by different cation compositions.

5.2 Results and analysis

5.2.1 Introductory results

To study the carrier-exciton dynamics in 2D perovskites, we need samples that are transparent to the broadband THz pulses in our TRTS setup. We used thin films to facilitate spectroscopy measurements in transmission mode and to be close to the device operating conditions of the material. As showed in the previous chapters, this can be achieved using high-density polyethylene (HDPE) as a substrate. Equally, the samples were prepared through a spin-coating procedure using a precursor solution in DMSO and antisolvent.²⁶ These samples were used for both TRTS and FLUPS to minimize the variations between samples. More information about the samples can be found in the Appendix (Figures A.15 and A.16).

TRTS is especially sensitive to charge carriers. The THz absorption signal ($-\Delta E/E$) is, for a thin film, typically proportional to the photoconductivity ($\Delta\sigma$), which in turn is proportional to the photogenerated carrier density (N) and mobility (μ), following Equation 4.1. This can be used to rationalize the frequency-averaged THz absorption dynamics (measured at the point of highest THz electric field). Nonetheless, this is only valid if the absorption spectrum is flat across different frequencies and does not substantially change over time, such as in the case of exciton formation. Otherwise, it is important to obtain spectra at different time delays to better characterize the system. This will be explored later in this chapter. On the other hand, the fluorescence can be considered proportional to the exciton density. This is due to the large E_b that induces exciton formation upon carrier relaxation before recombination. Since each exciton has a certain probability of recombining and emitting a photon, according to the radiative recombination kinetic constant, the higher the density is, the more photons will be emitted at a given time. Thus, each technique has a different sensitivity.

While the FLUPS signal will be dominated by excitons, free charge carriers will be more important in TRTS. This can be seen in Figure 5.1, where the THz signal decreases as the fluorescence increases. This clearly indicates a depletion of charge carriers through exciton formation. This process occurs during the first ps after excitation until a quasi-equilibrium is reached. After that, exciton recombination dominates the dynamics. The fit is the result of a tentative triexponential global fit where the time constants are linked between the two experiments, resulting in $\tau_1 = 0.35$ ps, $\tau_2 = 7$ ps and $\tau_3 = 60$ ps. A full view of the decays is shown in the Appendix (Figure A.17). *A priori*, τ_1 can be assigned to carrier relaxation and exciton formation, while the other two constants describe a combination of bimolecular and monomolecular decays highly dependent on the pump fluence. More evidence can be found when comparing the TRTS decays for samples excited at 400 nm and 510 nm (Figure 5.1, right). In the former, a higher carrier population is formed that needs to relax and condense to reach equilibrium. This does not occur in the latter since a large population of excitons is formed from the beginning. Figure A.18 shows how the decays are similar after the initial exciton formation decay.

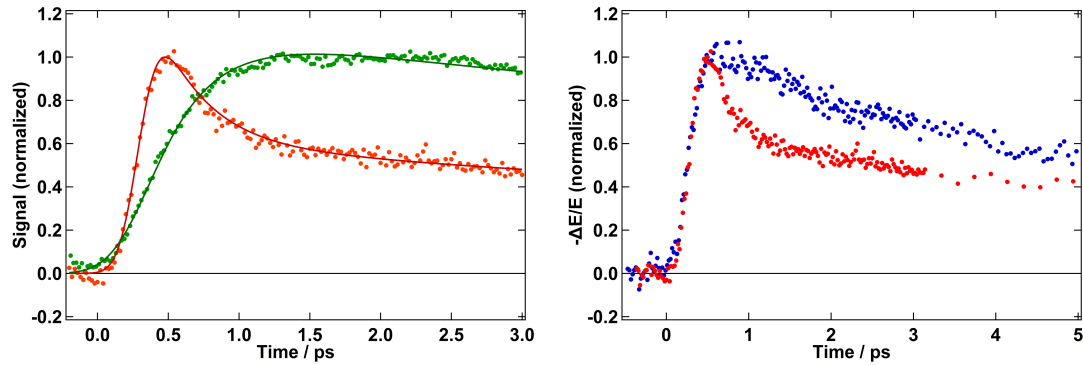


Figure 5.1: Left: Simultaneous rise and decay of the FLUPS (Green, $55 \mu\text{J cm}^{-2}$, $\lambda_{\text{obs}} = 532 - 538$ nm) and TRTS (Red, $56 \mu\text{J cm}^{-2}$) signals at $\lambda_{\text{exc}} = 400$ nm. Right: TRTS decay at $\lambda_{\text{exc}} = 400$ nm (Red, $56 \mu\text{J cm}^{-2}$) and at $\lambda_{\text{exc}} = 510$ nm (Blue, $60 \mu\text{J cm}^{-2}$). The TRTS signal is obtained at the maximum point (See Figure 5.3.E).

5.2.2 Spectral analysis

Let us now focus on the TRTS evolution using the spectral response. The fact that there is a considerable signal rise with the same time resolution for both excitation energies

indicates a noticeable THz absorption coming from the excitons. Otherwise, in the 510 nm case, a certain delay would be required to build up some carrier population. Equally, from a simple thermodynamic point of view, an equilibrium of mostly excitons should be attained after several ps when exciting above the bandgap into the continuum. In fact, we can use the Saha equation to estimate the expected proportion of carriers.²⁷

$$\frac{x^2}{1-x} = \frac{1}{n} \left(\frac{2\pi\mu k_B T}{h^2} \right) e^{\frac{E_b}{k_B T}}, \quad (5.1)$$

where μ is the reduced mass of the exciton ($0.28 m_0$),²⁸ E_b is the exciton binding energy, k_B is the Boltzmann constant, T is the temperature, h is the Planck constant, n is the excitation density and x is the fraction of free carriers. At $T = 300$ K and considering an E_b of 270 meV²⁸ with an excitation density of 10^{18} cm⁻³, the expected carrier fraction is less than 1%. Our experiments can reach excitation densities of 10^{19} cm⁻³ for the highest fluences, further decreasing the free charge carrier fraction. Therefore, the bulk of the signal when excited at 510 nm and at later times should come from excitons according to this analysis. In contrast, at high excitation densities, semiconductors undergo an insulator-to-metal transition or Mott transition, where the screening produced by the carriers effectively reduces the exciton binding energy until the attraction force is lost. The result is an electron-hole plasma. This can be observed with TRTS on Si.²⁹ Recently, it was found that excitons are surprisingly persistent in bulk CH₃NH₃PbBr₃ perovskite above the Mott density, which is attributed to Mahan excitons.³⁰ It is therefore unclear whether an electron-hole plasma is stabilized at densities in the range of $10^{18} - 10^{19}$ cm⁻³ for 2D perovskites. This motivates an analysis of the THz absorption spectra at different time delays to discern the evolution of free carriers into excitons. Both species are expected to show characteristic THz spectra. Charge carriers are typically described using the semiclassical Drude and Drude-Smith models, where the latter is used to describe carriers with an important backscattering component, usually observed in quantum confined systems such as nanoparticles^{31,32} We have introduced these models in Section 2.1.5.2. They consider that charges are accelerated under the THz electric field and are scattered with a time constant τ .³³ This acceleration produces the THz absorption and the result is a frequency dependent photoconductivity ($\Delta\sigma(\omega)$), where $\Delta\sigma(0)$ is defined as the DC photoconductivity or $\Delta\sigma_{DC}$. It has the values $\Delta\sigma_{DC} = \omega_p^2 \epsilon_0 \tau$ and $\Delta\sigma_{DC} = \omega_p^2 \epsilon_0 \tau (1 + c)$ for the Drude and Drude-Smith models, respectively. Therefore, $\Delta\sigma_{DC}$ typically has a nonzero value for charge carriers, unless

$c = -1$. In contrast, excitons do not follow these models in the interaction with THz radiation. In this case, the THz absorption corresponds to intraexcitonic transitions between internal degrees of freedom (1s-np transitions) and between the excitonic and free carrier states (Figure 5.2).²⁰ Such transitions have been studied in the past, *e.g.*, in GaAs quantum wells²⁰⁻²² or bulk lead halide perovskites,³⁴ at low temperatures. Accurate modeling needs to take into account multiple transitions.²⁰ However, considering the high binding energy in our sample, the different 1s-np transitions can be separated and approximated as a Lorentz oscillator.³⁴ In addition, they are expected to peak outside the observed window. The model follows Equation 2.49 explained in Section 2.1.5.2. The Lorentz oscillator model is characterized by a zero $\Delta\sigma_{DC}$. Hence, any $\Delta\sigma_{DC} \neq 0$ can be assigned to free carrier contribution. At low frequencies, an excitonic model predicts a greater imaginary part of $\Delta\sigma(\omega)$, seen as a phase shift of the $\Delta E(t)$ waveform. This is expressed as a measure of the polarizability of excitons and can be followed through the changes in ΔE at the zero-crossing point.³⁵⁻³⁸ However, such a phase-shift (imaginary part) component can also be produced by out-of-phase motion of carriers, such as the backscattering scenario of nanostructured materials modeled with the Drude-Smith model. This is why a full study of the $\Delta\sigma(\omega)$ spectra at different delays is preferable and more selective.

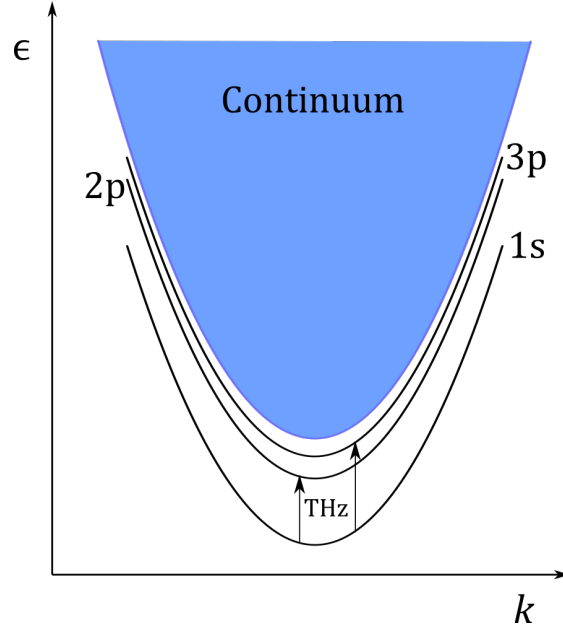


Figure 5.2: Intraexcitonic transitions accessible with THz spectroscopy.

We performed a 2D TRTS scan of our PEA_2PbI_4 sample excited at 400 nm with a fluence of $60 \mu\text{J cm}^{-2}$. The 2D maps are shown in Figure A.19. A selection of the progressive spectral changes can be observed in Figure 5.3.A. No clear resonance is observed in the analyzed frequency range. Resonances, such as those observed for GaAs quantum wells,²⁰ are not expected to be fully observable given the large E_b and the fact that our probe can only reach *ca.* 80 meV. Nonetheless, the response below the peak can still be observed. As the signal evolves, the spectrum changes through a marked decrease in $\Delta\sigma_{DC}$ while $\text{Im}(\Delta\sigma)$ increases and then is maintained at a large value. This can be preliminarily correlated with exciton formation. However, stronger evidence and information are obtained through the analysis using the photoconductivity models previously presented. If we take a linear combination of the Drude-Smith model and a Lorentz oscillator (red and green respectively in Figure 5.3, C and D) we can apply a global fit to all the spectra. The results (Figure 5.3.C) show how the amplitude of the Drude-Smith model (carriers) decreases with the general decay of the signal, while that of the Lorentz oscillator (excitons) increases and stabilizes. This coincides with what we observed in Figure 5.1. Certainly, the global fit is a simplification. Changes affecting τ or γ involving many-body effects are not considered. Nevertheless, the fit

gives a convincing description of the global process. The effects of the spectral changes can be observed in the $\Delta E(t)$ waveform as a gradual phase shift, which should agree with its measurement using the zero-crossing point. However, $\Delta E(0.1 \text{ ps})$ already possesses a considerable signal at the zero crossing, which is probably produced by out-of-phase carriers. The results of the fit show that the excitons are described by a resonance centered at $\omega_0 = 26 \text{ THz}$ with $\gamma = 20 \text{ THz}$, while the carriers are described by the Drude-Smith model with $\tau = 6.7 \text{ fs}$ and $c = -0.7$. While the values cannot be very precise due to the similarities of the two models, the latter describes carriers with a considerably low mobility ($\mu_{DC} = 5.8 \text{ cm}^2 \text{ V}^{-1} \text{ s}^{-1}$, considering an effective mass of $0.605 m_0$ ²⁸) and an important backscattering component. This is not surprising, taking into account the moderate mobility of perovskites³⁹ and the nanostructured nature of the sample.

Interestingly, while the excitonic contribution starts to dominate after a few ps, there is still a noticeable presence of carriers, judging from the value of $\Delta\sigma_{DC}$. Here, we can suggest two hypotheses. On the one hand, Auger heating through exciton-exciton annihilation may produce new hot carriers for every annihilated exciton.^{40,41} On the other hand, the high excitation density used may produce a partial Mott transition. In this case, a portion of the excitons are or remain dissociated as an electron-hole plasma. Nonetheless, it is clear from the spectral analysis that a great proportion of the excitons are undissociated. One way to clarify this observation is by analyzing the emission spectra at different fluences. In Figure 5.4.A, we can see the effect of fluence on the emission spectrum at an early time (1 ps). If we were in a regime where the Mott transition was starting to play a role, then E_b should decrease with fluence as the screening becomes stronger.³⁰ This would translate into a blueshift of the emission peak since the excitons are less stabilized. However, we do not observe any blueshift of the peak with fluence. In contrast, a shoulder on the red side of the peak becomes more important as we increase the fluence. This could be a sign of biexcitons, where the additional stabilization produces a slight redshift of the emission that is observed as a small additional sideband. This was described for colloidal nanoplatelets in a previous work.⁴² In addition, biexcitons have already been reported in 2D perovskites with a binding energy of $44 \pm 5 \text{ meV}$ by F. Thouin et al.⁴³ Indeed, a qualitative agreement can be found through a multi-peak fit (Figure 5.4, B and C). The biexciton picture

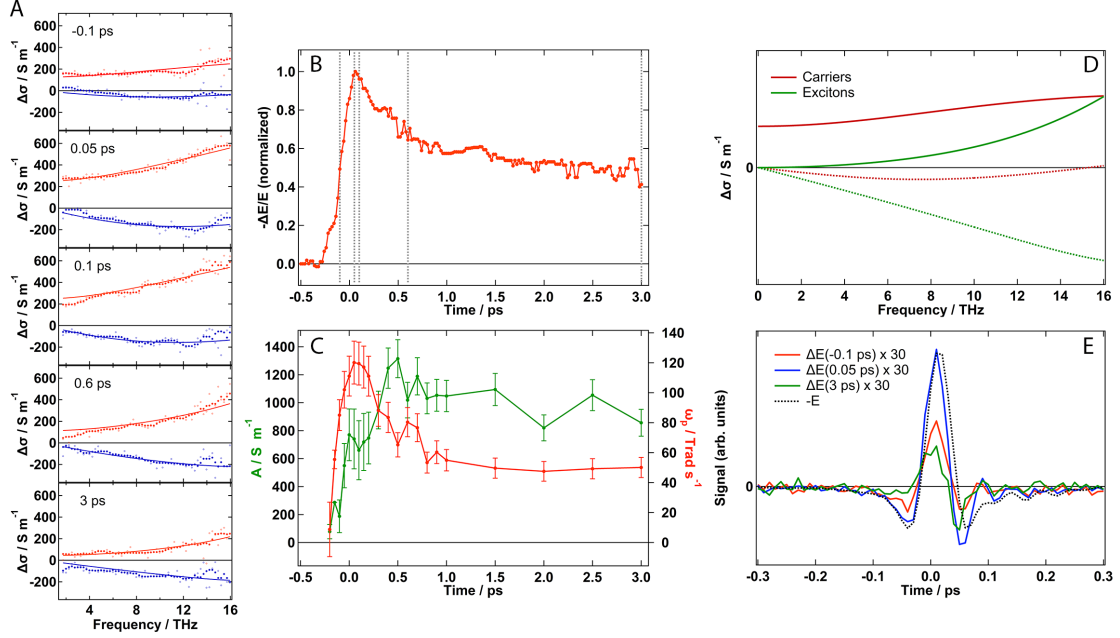


Figure 5.3: A) Real (red) and imaginary (blue) parts of the $\Delta\sigma(\omega)$ spectra at different time delays after excitation. The solid lines are the results of the global fit. B) $-\Delta E/E$ evolution as a function of pump-probe delay. The dashed lines indicate the times corresponding to the spectra in A. C) Result of the global fit on the spectra at all times. ω_p and A are taken as a measure of the amplitude of the signals emanating from carriers and excitons, respectively, in order to follow their evolution. D) Simulated spectra from the Drude-Smith (red) and the Lorentz oscillator (green) models as a result of the global fit. E) $\Delta E(t)$ (solid) and $-E(t)$ (dashed) THz waveforms. The plot shows the changes in the waveforms that produce the spectral changes shown in A. The measurements are taken at $\lambda_{\text{exc}} = 400$ nm and $F = 60 \mu\text{J cm}^{-2}$ on PEA_2PbI_4 . On A and B, median filters are applied to clean up the traces.

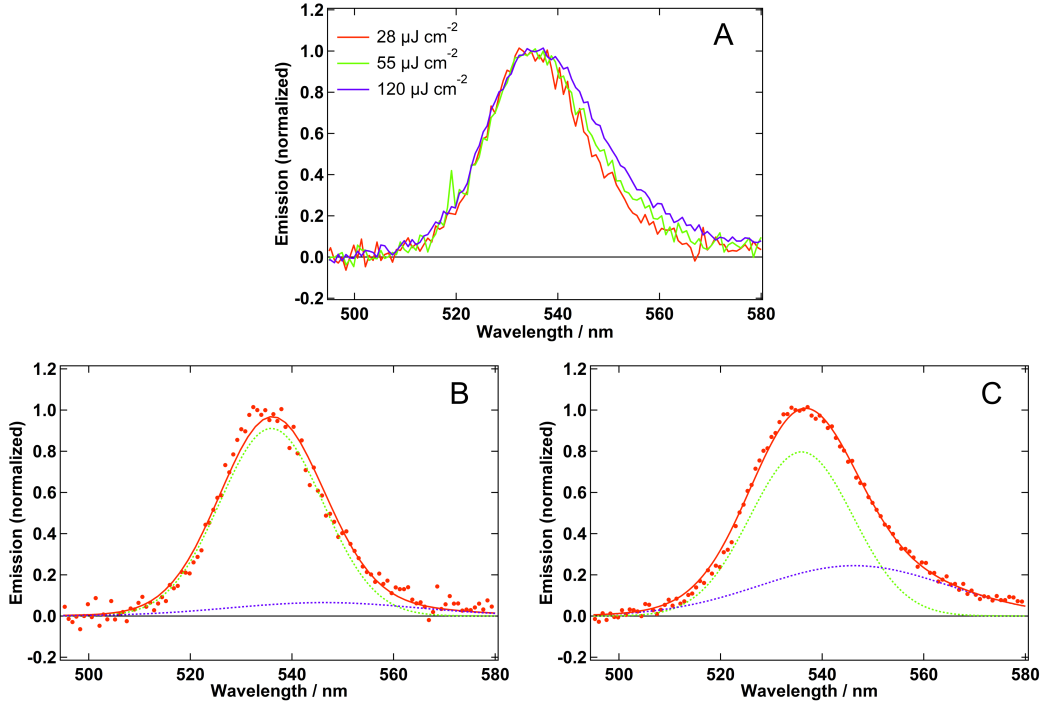


Figure 5.4: A) Normalized emission obtained from averaging the 0.96-1.04 ps range for different fluences. At higher fluences, additional contributions are only seen on the low energy side of the band. B-C) Multipeak fit of the emission at 1 ps for 28 $\mu\text{J cm}^{-2}$ (B) and 120 $\mu\text{J cm}^{-2}$ (C). The main peak is centered at 536 nm while the second peak is the result of a red-shift of 44 meV. The second peak is clearly more important at a higher fluence. The widths and positions are equal for the two fits.

reinforces the idea of important exciton-exciton interactions being the source of new carriers through an Auger process. Interestingly, a shift or broadening towards the blue can be observed during the first 10 ps that is not fluence dependent (Figure A.20). A possible explanation is that it may be produced by reabsorption on the blue side of the emission by the excitonic absorption peak. This would be due to the geometry of the measurement, where the emitted light is collected from the back. As the excitons diffuse across the sample less light is reabsorbed and a blue-shift is observed.

5.2.3 Fluence dependence and kinetic modelling

To gain more insights into the kinetics of the processes involved, it is useful to carry out fluence-dependent measurements, where the higher order kinetics will be highlighted. When exciting with excess energy ($\lambda_{\text{exc}} = 400$ nm, Figure 5.5, left), the increased fluence mainly affects the end of the initial decay and the long-term decay in opposite ways. However, the relative amplitude of the initial decay is surprisingly little affected by a tenfold increase in fluence. If a simple equilibrium between carriers and excitons was established, then, it would be expected that the greatest initial decay would occur at higher fluences, due to the facilitation of nongeminate exciton formation at higher densities. This is not the case, and the reason may lie in the impossibility of hot exciton formation. In fact, we do not observe hot exciton emission in the way that it was observed for nanoplatelets and nanoparticles.⁴² This initial decay may therefore be limited by cooling, which can be lengthened at higher fluences due to phonon bottleneck effects,⁴⁴ Auger heating^{45,46} and polaron screening.^{47–49} Afterwards, a carrier-exciton equilibrium is formed, and the decay dynamics are dominated by exciton recombination. At higher fluences, bimolecular exciton-exciton annihilation⁴¹ becomes increasingly important, shortening the decay of both carriers and excitons. These two phenomena can be observed with a triexponential fit as a minimal increase in the first time constant and a decrease in the other two (Table 5.1).

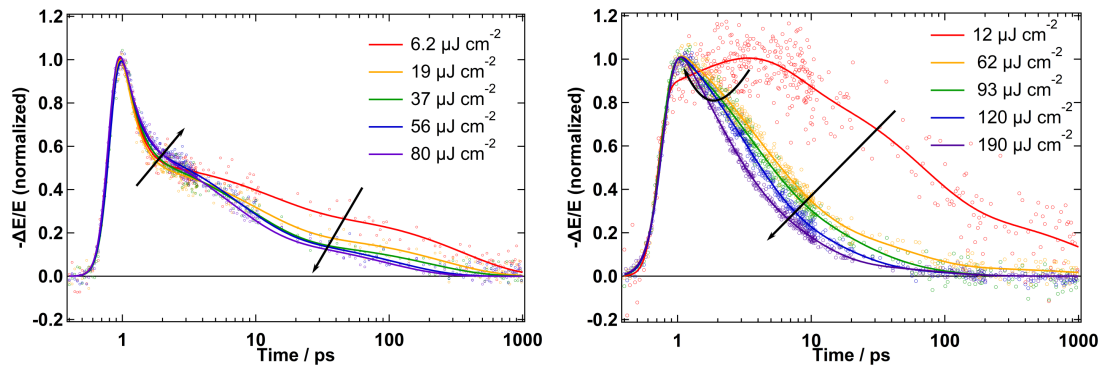


Figure 5.5: Fluence dependence of the decay dynamics at $\lambda_{\text{exc}} = 400$ nm (left) and at $\lambda_{\text{exc}} = 510$ nm (right). The arrows indicate the effect of the increasing excitation density. A 3 exponential fit is used for the $\lambda_{\text{exc}} = 400$ nm data (See results in Table 5.1) while a 4 exponential is used for $\lambda_{\text{exc}} = 510$ nm to take into account the slower rise.

Fluence / $\mu\text{J cm}^{-2}$	τ_1 / ps	τ_2 / ps	τ_3 / ps
6.2	0.293 ± 0.025	12.5 ± 2.2	360 ± 35
19	0.286 ± 0.022	9.75 ± 1.1	248 ± 36
37	0.313 ± 0.023	8.52 ± 0.76	198 ± 35
56	0.288 ± 0.021	7.10 ± 0.64	111 ± 21
80	0.331 ± 0.021	6.06 ± 0.54	91.8 ± 16

Table 5.1: Fluence dependence of the triexponential fit for the $-\Delta E/E$ decay at $\lambda_{\text{exc}} = 400$ nm. The first time constant can be related to carrier cooling and exciton formation while the latter two can be assigned to recombination.

Alternatively, when exciting at resonant conditions ($\lambda_{\text{exc}} = 510$ nm, Figure 5.5, right), there are two observable effects of the fluence: an expected decrease in the general decay lifetime and the appearance of a slower rise at the lowest fluence used. This rise could be assigned to the formation of charge carriers, from the initial excitons to when equilibrium is reached. However, taking into account that the exciton binding energy is on the order of 270 meV,²⁸ much higher than the thermal energy ($k_B T = 25.6$ meV at 25°C), it is difficult to assume that excitons can spontaneously split into carriers only due to thermal energy. Once again, Auger heating through exciton-exciton annihilation can be used to explain the rise. To do so, we can define three fluence regimes: a) a low fluence regime, where no such processes occur, b) an intermediate fluence regime, where such processes occur and can be observed as a slow buildup of the carrier population, and c) a high fluence regime, where bimolecular decay processes are so important that any rise in the signal is buried. The data we have been able to collect mostly belong to the latter regime, while the lowest fluence we show, $12 \mu\text{J cm}^{-2}$, belongs to the intermediate regime.

We can propose a model that includes Auger heating through exciton-exciton annihilation as well as sequential carrier cooling, exciton formation and recombination. The proposed model is described by the scheme in Figure 5.6.A and the differential equations can be found in the Appendix (Section B.7). The model considers three different populations, namely, excitons, hot carriers and cold carriers. It considers two possible excitation sources generating either hot carriers ($\lambda_{\text{exc}} = 400$ nm) or excitons ($\lambda_{\text{exc}} = 510$ nm). Excitons can monomolecularly recombine, either through emission of photons or

interaction with traps, with a kinetic rate constant k_{er} . In addition, they can undergo a process of exciton-exciton annihilation where Auger heating is produced (k_a). Two excitons produce two hot carriers from one of them, while the other, having transferred its energy, recombines. As a simplification, hot carriers are monomolecularly cooled with a rate constant k_c . Finally, cold carriers condense into excitons (k_{ef}), but the latter can also split into cold carriers (k_{ed}). However, this process is disfavored due to the large E_b . Indeed, several approximations are required to obtain a model we can work with. First, all processes occurring in the first hundreds of fs, defining the rise of the signal, are included in a generation term G with the form of a Gaussian. These processes can include coherence loss,⁵⁰ thermalization (not cooling)¹⁵ and the development of many-body interactions,⁵¹ perhaps including polaron formation.^{47–49,52,53} This explains why the rise is characterized by a Gaussian of FWHM = 300 fs, longer than the time resolution expected for this experiment (~ 50 fs). Next, hot and cold carriers are considered as two distinct particles and not as a distribution of particles characterized by a certain temperature. In addition, phonon populations are not considered.⁴⁵ Possible phonon bottleneck effects are considered as a change in k_c . Finally, processes affecting the actual density of carriers, such as diffusion⁵⁴ or even trap saturation are not included.

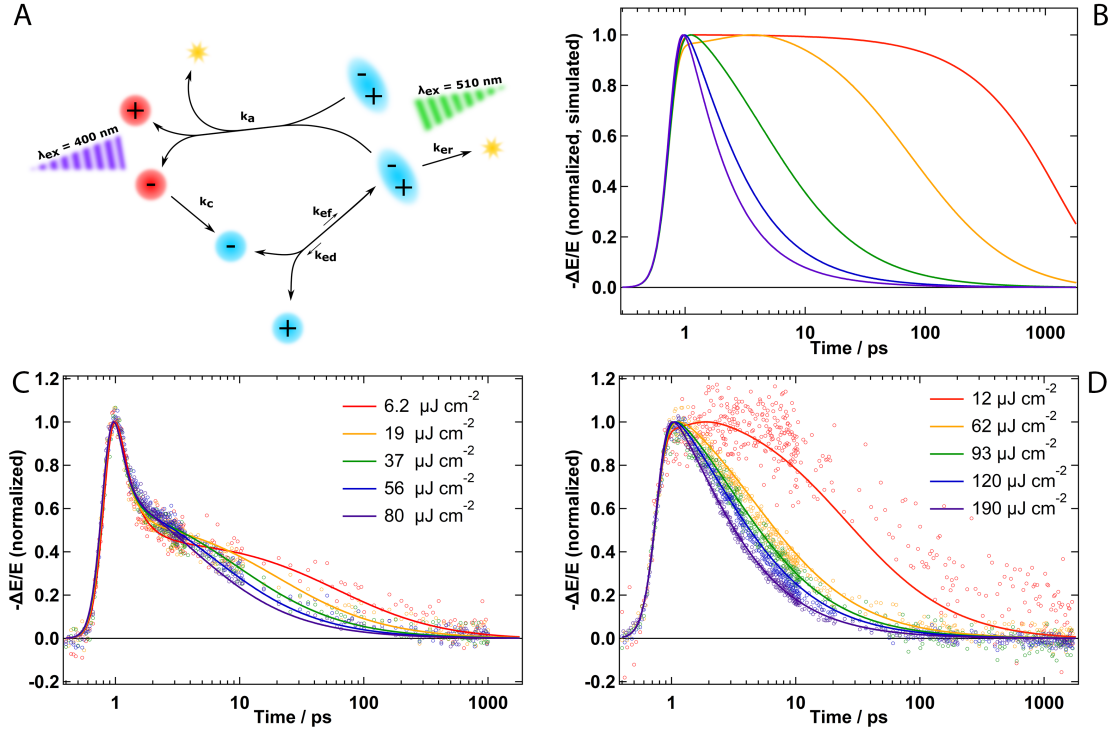


Figure 5.6: A) Kinetic model relating hot carriers (red), cold carriers (blue) and excitons, generated with the two wavelengths used in the presented experiments. B) Simulations obtained from the model at $\lambda_{exc} = 510 \text{ nm}$ and a large variety of fluences. 1) At high densities, the signal can decay with a strong bimolecular behavior (purple, blue and green). 2) At a low density, it can have a slow exciton recombination decay (red). 3) Under an intermediate regime, it presents a slight rise of the signal due to the generation of carriers under Auger heating, followed by recombination (orange). C and D) TRTS data and the results of the global fit for $\lambda_{exc} = 400 \text{ nm}$ and $\lambda_{exc} = 510 \text{ nm}$, respectively.

Employing numerical methods, we can use this model to simulate the signal obtained from a combination of the densities of the three particles multiplied by a proportionality constant (Figure 5.6.B and Section B.7, in the Appendix). Clearly, this model can reproduce the two regimes observed at high and moderate fluences as well as be used to extrapolate what the signal would look like at a very low fluence. Moreover, we can use

the model to globally fit all the data across the two different wavelengths. The results show general agreement with both the fluence and wavelength trends seen in Figure 5.5, showing that this three-particle picture is sufficient for explaining the observed behavior. The strength of the global fit lies in the fact that all kinetic parameters are shared for all traces and the density is fixed to a value proportional to the fluence used (See more details in the Appendix). Certainly, this, in addition to the approximations and possible uncertainties, explains the small deviations. Indeed, perfect agreement could be obtained from independent fits, as for any complex model, but the results would be meaningless. The numerical results are shown in the Appendix (Table 5.2). These should not be taken at face value since different combinations can give acceptable fits, especially for the bimolecular constants. The importance lies in the global behavior and how the model explains the trends. Furthermore, the signal contributions from excitons and carriers according to the fitted model (Figure 5.7) show qualitative agreement with the spectral evolution (Figure 5.3.C).

Parameter	Fitted value
k_{er} / ps^{-1}	$8.58 \cdot 10^{-4} \pm 9.82 \cdot 10^{-6}$
$k_{ef} / \text{ps}^{-1} \text{ adu}^{-1}$	$1.14 \pm 1.79 \cdot 10^{-2}$
$k_a / \text{ps}^{-1} \text{ adu}^{-1}$	$8.84 \cdot 10^{-3} \pm 9.98 \cdot 10^{-5}$
k_c / ps^{-1}	5.26 ± 0.16
$a_{400\text{nm}} / \text{adu}$	7.47 ± 0.22
$a_{510\text{nm}} / \text{adu}$	9.02 ± 0.09
$c_{ex} / -$	0.48 ± 0.02
$c_{hc} / -$	0.57 ± 0.03

Table 5.2: Results of the global fit with their corresponding fit error, where “adu” stands for arbitrary density unit.

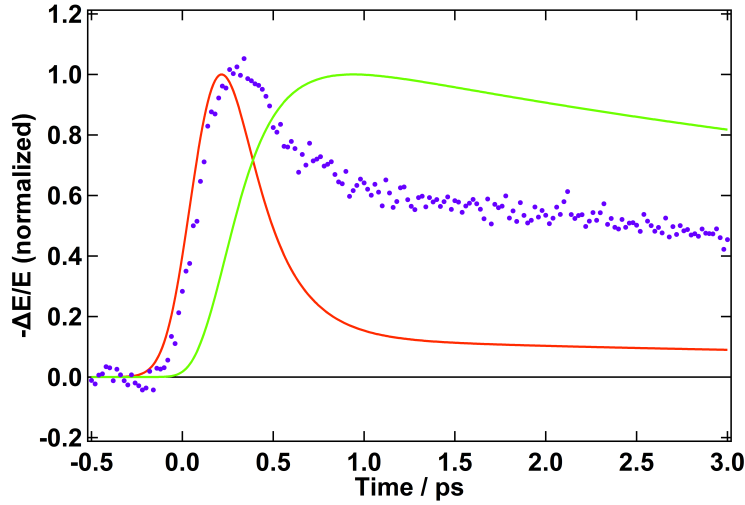


Figure 5.7: Exciton (green) and carrier (red) evolution according to the global fit on the kinetic model. Excitons show a delayed rise and a certain concentration of carriers is maintained due to auger heating.

5.2.4 Influence of the cation

Once we have explained the observed signal through both spectral analysis and decay modeling, we can compare the obtained results with those for a different composition. To achieve this aim, we investigated the TRTS dynamics upon $\lambda_{\text{exc}} = 400$ nm excitation of a sample of BuA_2PbI_4 , where BuA stands for butylammonium. Judging from the steady state spectra (Figure A.15), the two samples are not very different in terms of E_b . Regarding the TRTS dynamics, the main difference is observed in the first decay, which appears to lengthen with increasing fluence (Figure 5.8). We know that this decay corresponds to the formation of excitons from the initially high population of carriers. In part, this is limited by the cooling of hot carriers. Indeed, from the previous fit, we have obtained that the exciton formation has a lifetime for the lowest fluence ($\tau_{ef} = 1/(k_{efa})$) of 0.12 ps (0.009 ps for the highest) while τ_c is 0.19 ps. Therefore, a lengthening of this decay can be associated with a longer cooling. As opposed to the PEA_2PbI_4 case (Figure 5.6.C), the data cannot be fitted with only one k_c shared among all traces (Figure A.21, left, in the Appendix). Thus, we proceeded to fit both the PEA_2PbI_4 and BuA_2PbI_4 data with separate k_c values for each trace. The results are shown in Figures A.21 and 5.8, as well as in Table 5.3.

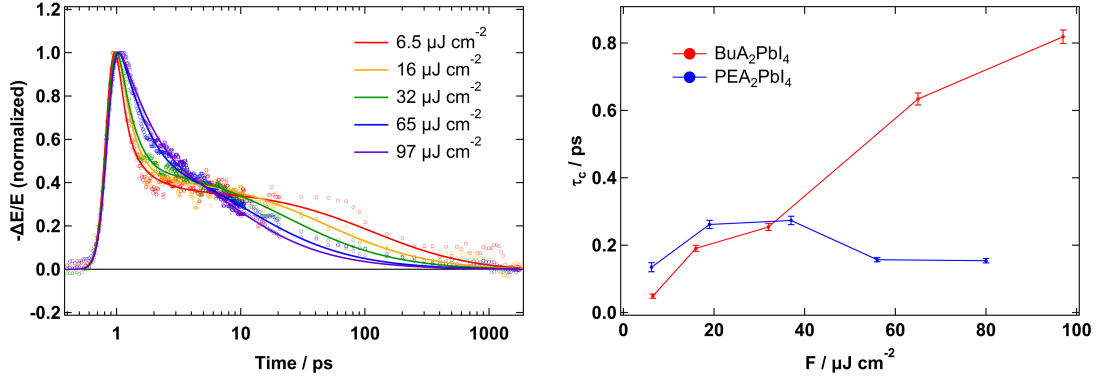


Figure 5.8: TRTS decay dynamics of BuA₂PbI₄ with the result of the global fit using independent k_c values for each trace. Right) τ_c , or $1/k_c$, values for the two different compositions at different fluences.

	BuA ₂ PbI ₄	PEA ₂ PbI ₄
k_{er} / ps^{-1}	$1.22 \cdot 10^{-3} \pm 2.49 \cdot 10^{-5}$	$9.85 \cdot 10^{-4} \pm 1.61 \cdot 10^{-5}$
$k_{ef} / \text{ps}^{-1} \text{ adu}^{-1}$	$1.65 \pm 7.19 \cdot 10^{-2}$	$1.68 \pm 5.39 \cdot 10^{-2}$
$k_a / \text{ps}^{-1} \text{ adu}^{-1}$	$7.10 \cdot 10^{-3} \pm 1.39 \cdot 10^{-4}$	$7.57 \cdot 10^{-3} \pm 1.31 \cdot 10^{-4}$
k_{c1} / ps^{-1}	20.5 ± 2.65	$7.44 \pm 7.48 \cdot 10^{-1}$
k_{c2} / ps^{-1}	$5.24 \pm 2.46 \cdot 10^{-1}$	$3.82 \pm 1.76 \cdot 10^{-1}$
k_{c3} / ps^{-1}	$3.94 \pm 1.60 \cdot 10^{-1}$	$3.66 \pm 1.66 \cdot 10^{-1}$
k_{c4} / ps^{-1}	$1.58 \pm 4.43 \cdot 10^{-2}$	$6.37 \pm 2.51 \cdot 10^{-1}$
k_{c5} / ps^{-1}	$1.22 \pm 3.00 \cdot 10^{-2}$	$6.49 \pm 2.73 \cdot 10^{-1}$
$a_{400\text{nm}} / \text{adu}$	$4.68 \pm 6.38 \cdot 10^{-2}$	$7.22 \pm 1.42 \cdot 10^{-1}$
$c_{ex} / -$	$35 \pm 6.10 \cdot 10^{-3}$	$0.59 \pm 2.55 \cdot 10^{-2}$
$c_{hc} / -$	$0.45 \pm 9.23 \cdot 10^{-3}$	$0.78 \pm 4.41 \cdot 10^{-2}$

Table 5.3: Results for the global fit with independent k_c for each trace.

While PEA₂PbI₄ does not show a clear trend, in BuA₂PbI₄ the cooling time clearly increases with fluence. This could be caused by a phonon bottleneck effect similar to that found in bulk lead halide perovskites.^{45,55,56} Interestingly, an enhanced phonon bottleneck was observed on quasi-2D ($n > 1$) perovskites containing BuA.⁴⁴ On the other

hand, nanocrystals tend to show lengthened cooling, even allowing the extraction of hot carriers.¹⁹ Recently, it was shown that PEA_2PbI_4 presents faster cooling kinetics (220 fs, very similar to our value of 190 fs) than 2D perovskites containing large permittivity cations ($\text{HOC}_2\text{H}_4\text{NH}_2^+$, 720 fs, and $\text{HOC}_3\text{H}_6\text{NH}_2^+$, 640 fs).¹⁸ Although bottleneck effects were not explored, the difference was explained, with the help of *ab initio* simulations, as a combination of 1) a difference in screening due to the permittivity of the cations; 2) different nonadiabatic couplings between conduction bands; 3) different electron-phonon couplings; and 4) suppressed rotation of the spacers. While the first factor is not applicable to our cations, the rest may produce the difference in cooling we observe. Future work should address this question. Lastly, we were unable to obtain 2D TRTS maps or FLUPS spectra of BuA_2PbI_4 . We did find that this 2D perovskite was much less stable under illumination, especially in the presence of air. We show the effects of this degradation on the recorded FLUPS spectra in Figure 5.9. Nonetheless, the BuA_2PbI_4 sample was stable for long enough to obtain the dynamics shown in Figure 5.8, owing to the inert atmosphere used in TRTS. However, 2D maps require a considerable fluence for more than 24 h, which produced a certain degree of degradation. In summary, for applications where both stability and fast carrier cooling are critical PEA_2PbI_4 is the better option.

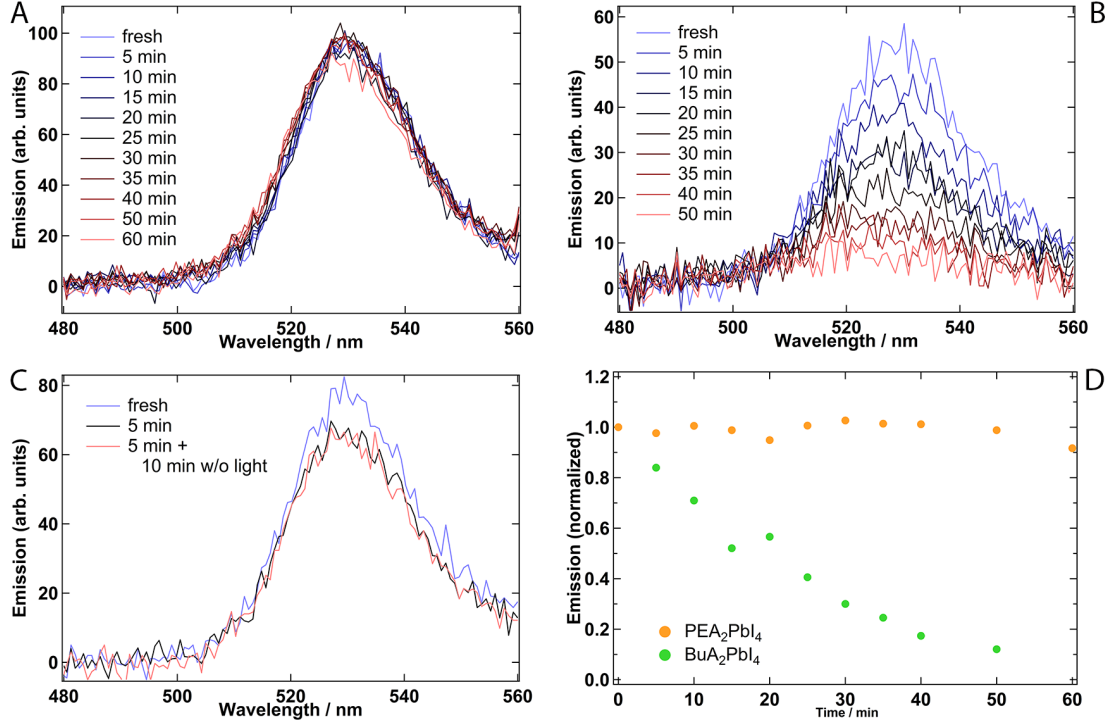


Figure 5.9: Stability comparison by following the FLUPS emission spectra between A) PEA₂PbI₄ and B) BuA₂PbI₄ under laser light illumination. Indeed, C) shows that only under laser light the signal decays. D) In a few minutes the degradation is substantial for BuA₂PbI₄, rendering the FLUPS measurements impossible.

5.3 Conclusions

We have studied in detail the evolution of carriers and excitons in 2D perovskites using a combination of sensitive spectroscopic techniques. Indeed, we have shown the potential of using ultra-broadband TRTS to study the evolution of carriers into excitons with a large binding energy at room temperature by following the spectral changes. In combination with fluorescence upconversion spectroscopy, we have demonstrated sequential cooling and exciton formation where exciton-exciton interactions play an important role. These are the source of a longer-lived population of carriers despite the large correlation induced by the quantum and dielectric confinements. We have presented and applied a kinetic model that can explain our data through the use of global fits. Once again, the model

assumes that electrons and holes behave similarly and no distributions are used. Finally, we have used the previously presented work to explore the influence of the organic cation. We find that although the changes in the steady-state photophysics are small, the choice of the cation is crucial for both stability and hot carrier cooling, strongly affecting phonon bottleneck effects, which is a phenomenon to be considered for future applications.

References

- (1) Best Research-Cell Efficiency Chart, Photovoltaic Research, NREL., <https://www.nrel.gov/pv/cell-efficiency.html> (accessed 11/18/2019).
- (2) Kojima, A.; Teshima, K.; Shirai, Y.; Miyasaka, T. Organometal Halide Perovskites as Visible-Light Sensitizers for Photovoltaic Cells. *J. Am. Chem. Soc.* **2009**, *131*, 6050–6051.
- (3) Lee, M. M.; Teuscher, J.; Miyasaka, T.; Murakami, T. N.; Snaith, H. J. Efficient Hybrid Solar Cells Based on Meso-Superstructured Organometal Halide Perovskites. *Science* **2012**, *338*, 640–643.
- (4) Jeon, N. J.; Noh, J. H.; Kim, Y. C.; Yang, W. S.; Ryu, S.; Seok, S. I. Solvent Engineering for High-Performance Inorganic–Organic Hybrid Perovskite Solar Cells. *Nat. Mater.* **2014**, *13*, 897–903.
- (5) Jena, A. K.; Kulkarni, A.; Miyasaka, T. Halide Perovskite Photovoltaics: Background, Status, and Future Prospects. *Chem. Rev.* **2019**, *119*, 3036–3103.
- (6) Smith, I. C.; Hoke, E. T.; Solis-Ibarra, D.; McGehee, M. D.; Karunadasa, H. I. A Layered Hybrid Perovskite Solar-Cell Absorber with Enhanced Moisture Stability. *Angew. Chem.* **2014**, *126*, 11414–11417.
- (7) Gangadharan, D. T.; Ma, D. Searching for Stability at Lower Dimensions: Current Trends and Future Prospects of Layered Perovskite Solar Cells. *Energy Environ. Sci.* **2019**, *12*, 2860–2889.
- (8) Lu, J.; Jiang, L.; Li, W.; Li, F.; Pai, N. K.; Scully, A. D.; Tsai, C.-M.; Bach, U.; Simonov, A. N.; Cheng, Y.-B.; Spiccia, L. Diammonium and Monoammonium Mixed-Organic-Cation Perovskites for High Performance Solar Cells with Improved Stability. *Adv. Energy Mater.* **2017**, *7*, 1700444.
- (9) Ye, J.; Zheng, H.; Zhu, L.; Liu, G.; Zhang, X.; Hayat, T.; Pan, X.; Dai, S. Enhanced Moisture Stability of Perovskite Solar Cells With Mixed-Dimensional and Mixed-Compositional Light-Absorbing Materials. *Solar RRL* **2017**, *1*, 1700125.
- (10) Stoumpos, C. C.; Cao, D. H.; Clark, D. J.; Young, J.; Rondinelli, J. M.; Jang, J. I.; Hupp, J. T.; Kanatzidis, M. G. Ruddlesden–Popper Hybrid Lead Iodide Perovskite 2D Homologous Semiconductors. *Chem. Mater.* **2016**, *28*, 2852–2867.

- (11) Hu, Y.; Spies, L. M.; Alonso-Álvarez, D.; Mocherla, P.; Jones, H.; Hanisch, J.; Bein, T.; Barnes, P. R. F.; Docampo, P. Identifying and Controlling Phase Purity in 2D Hybrid Perovskite Thin Films. *J. Mater. Chem. A* **2018**, *6*, 22215–22225.
- (12) Hong, X.; Ishihara, T.; Nurmikko, A. V. Dielectric Confinement Effect on Excitons in Pbi₄-Based Layered Semiconductors. *Phys. Rev. B* **1992**, *45*, 6961–6964.
- (13) Chernikov, A.; Berkelbach, T. C.; Hill, H. M.; Rigosi, A.; Li, Y.; Aslan, O. B.; Reichman, D. R.; Hybertsen, M. S.; Heinz, T. F. Exciton Binding Energy and Nonhydrogenic Rydberg Series in Monolayer WS₂. *Phys. Rev. Lett.* **2014**, *113*, 076802.
- (14) Chen, P.; Bai, Y.; Lyu, M.; Yun, J.-H.; Hao, M.; Wang, L. Progress and Perspective in Low-Dimensional Metal Halide Perovskites for Optoelectronic Applications. *Solar RRL* **2018**, *2*, 1700186.
- (15) Richter, J. M.; Branchi, F.; Camargo, F. V. d. A.; Zhao, B.; Friend, R. H.; Cerullo, G.; Deschler, F. Ultrafast Carrier Thermalization in Lead Iodide Perovskite Probed with Two-Dimensional Electronic Spectroscopy. *Nat. Commun.* **2017**, *8*, 376.
- (16) Wright, A. D.; Verdi, C.; Milot, R. L.; Eperon, G. E.; Pérez-Osorio, M. A.; Snaith, H. J.; Giustino, F.; Johnston, M. B.; Herz, L. M. Electron–Phonon Coupling in Hybrid Lead Halide Perovskites. *Nat. Commun.* **2016**, *7*, 11755.
- (17) Hintermayr, V. A.; Polavarapu, L.; Urban, A. S.; Feldmann, J. Accelerated Carrier Relaxation through Reduced Coulomb Screening in Two-Dimensional Halide Perovskite Nanoplatelets. *ACS Nano* **2018**, *12*, 10151–10158.
- (18) Yin, J.; Maity, P.; Naphade, R.; Cheng, B.; He, J.-H.; Bakr, O. M.; Brédas, J.-L.; Mohammed, O. F. Tuning Hot Carrier Cooling Dynamics by Dielectric Confinement in Two-Dimensional Hybrid Perovskite Crystals. *ACS Nano* **2019**, *13*, 12621–12629.
- (19) Li, M.; Bhaumik, S.; Goh, T. W.; Kumar, M. S.; Yantara, N.; Grätzel, M.; Mhaisalkar, S.; Mathews, N.; Sum, T. C. Slow Cooling and Highly Efficient Extraction of Hot Carriers in Colloidal Perovskite Nanocrystals. *Nat. Commun.* **2017**, *8*, 14350.

- (20) Kaindl, R. A.; Haegele, D.; Carnahan, M. A.; Chemla, D. S. Transient Terahertz Spectroscopy of Excitons and Unbound Carriers in Quasi Two-Dimensional Electron-Hole Gases. *Physical Review B* **2009**, *79*.
- (21) Kira, M.; Hoyer, W.; Koch, S. Terahertz Signatures of the Exciton Formation Dynamics in Non-Resonantly Excited Semiconductors. *Solid State Commun.* **2004**, *129*, 733–736.
- (22) Kaindl, R. A.; Carnahan, M. A.; Hägele, D.; Lövenich, R.; Chemla, D. S. Ultrafast Terahertz Probes of Transient Conducting and Insulating Phases in an Electron–Hole Gas. *Nature* **2003**, *423*, 734–738.
- (23) Huber, R.; Kaindl, R. A.; Schmid, B. A.; Chemla, D. S. Broadband Terahertz Study of Excitonic Resonances in the High-Density Regime in GaAs/Al_xGa_{1-x}As Quantum Wells. *Phys. Rev. B* **2005**, *72*, 161314.
- (24) Docherty, C. J.; Parkinson, P.; Joyce, H. J.; Chiu, M.-H.; Chen, C.-H.; Lee, M.-Y.; Li, L.-J.; Herz, L. M.; Johnston, M. B. Ultrafast Transient Terahertz Conductivity of Monolayer MoS₂ and WSe₂ Grown by Chemical Vapor Deposition. *ACS Nano* **2014**, *8*, 11147–11153.
- (25) Hendry, E.; Koeberg, M.; Bonn, M. Exciton and Electron-Hole Plasma Formation Dynamics in ZnO. *Phys. Rev. B* **2007**, *76*, 045214.
- (26) Jung, J. W.; Williams, S. T.; Jen, A. K.-Y. Low-Temperature Processed High-Performance Flexible Perovskite Solar Cells Via Rationally Optimized Solvent Washing Treatments. *RSC Adv.* **2014**, *4*, 62971–62977.
- (27) Gélvez-Rueda, M. C.; Hutter, E. M.; Cao, D. H.; Renaud, N.; Stoumpos, C. C.; Hupp, J. T.; Savenije, T. J.; Kanatzidis, M. G.; Grozema, F. C. Interconversion between Free Charges and Bound Excitons in 2D Hybrid Lead Halide Perovskites. *J. Phys. Chem. C* **2017**, *121*, 26566–26574.
- (28) Zhao, Y.-Q.; Ma, Q.-R.; Liu, B.; Yu, Z.-L.; Yang, J.; Cai, M.-Q. Layer-Dependent Transport and Optoelectronic Property in Two-Dimensional Perovskite: (PEA)₂PbI₄. *Nanoscale* **2018**, *10*, 8677–8688.
- (29) Suzuki, T.; Shimano, R. Exciton Mott Transition in Si Revealed by Terahertz Spectroscopy. *Phys. Rev. Lett.* **2012**, *109*, 046402.

- (30) Palmieri, T.; Baldini, E.; Steinhoff, A.; Akrap, A.; Kollár, M.; Horváth, E.; Forró, L.; Jahnke, F.; Chergui, M. Mahan Excitons in Room-Temperature Methylammonium Lead Bromide Perovskites. *Nat. Commun.* **2020**, *11*, 1–8.
- (31) Smith, N. Classical Generalization of the Drude Formula for the Optical Conductivity. *Phys. Rev. B* **2001**, *64*, 155106.
- (32) Ulbricht, R.; Hendry, E.; Shan, J.; Heinz, T. F.; Bonn, M. Carrier Dynamics in Semiconductors Studied with Time-Resolved Terahertz Spectroscopy. *Rev. Mod. Phys.* **2011**, *83*, 543–586.
- (33) Dexheimer, S. L., *Terahertz Spectroscopy: Principles and Applications*; CRC Press: 2008.
- (34) Luo, L.; Men, L.; Liu, Z.; Mudryk, Y.; Zhao, X.; Yao, Y.; Park, J. M.; Shinar, R.; Shinar, J.; Ho, K.-M.; Perakis, I. E.; Vela, J.; Wang, J. Ultrafast Terahertz Snapshots of Excitonic Rydberg States and Electronic Coherence in an Organometal Halide Perovskite. *Nat. Commun.* **2017**, *8*, 15565.
- (35) Kumar, A.; Solanki, A.; Manjappa, M.; Ramesh, S.; Srivastava, Y. K.; Agarwal, P.; Sum, T. C.; Singh, R. Excitons in 2D Perovskites for Ultrafast Terahertz Photonic Devices. *Sci. Adv.* **2020**, *6*, eaax8821.
- (36) He, C.; Zhu, L.; Zhao, Q.; Huang, Y.; Yao, Z.; Du, W.; He, Y.; Zhang, S.; Xu, X. Competition between Free Carriers and Excitons Mediated by Defects Observed in Layered WSe₂ Crystal with Time-Resolved Terahertz Spectroscopy. *Adv. Opt. Mater.* **2018**, *6*, 1800290.
- (37) Jensen, S. A.; Ulbricht, R.; Narita, A.; Feng, X.; Müllen, K.; Hertel, T.; Turchinovich, D.; Bonn, M. Ultrafast Photoconductivity of Graphene Nanoribbons and Carbon Nanotubes. *Nano Lett.* **2013**, *13*, 5925–5930.
- (38) Wang, F.; Shan, J.; Islam, M. A.; Herman, I. P.; Bonn, M.; Heinz, T. F. Exciton Polarizability in Semiconductor Nanocrystals. *Nat. Mater.* **2006**, *5*, 861–864.
- (39) Herz, L. M. Charge-Carrier Mobilities in Metal Halide Perovskites: Fundamental Mechanisms and Limits. *ACS Energy Lett.* **2017**, 1539–1548.
- (40) Chmeliov, J.; Narkeliunas, J.; Graham, M. W.; Fleming, G. R.; Valkunas, L. Exciton-Exciton Annihilation and Relaxation Pathways in Semiconducting Carbon Nanotubes. *Nanoscale* **2016**, *8*, 1618–1626.

- (41) Delport, G.; Chehade, G.; Lédée, F.; Diab, H.; Milesi-Brault, C.; Trippé-Allard, G.; Even, J.; Lauret, J.-S.; Deleporte, E.; Garrot, D. Exciton-Exciton Annihilation in Two-Dimensional Halide Perovskites at Room Temperature. *J. Phys. Chem. Lett.* **2019**, *10*, 5153–5159.
- (42) Vale, B. R. C.; Socie, E.; Burgos-Caminal, A.; Bettini, J.; Schiavon, M. A.; Moser, J.-E. Exciton, Biexciton, and Hot Exciton Dynamics in CsPbBr₃ Colloidal Nanoplatelets. *J. Phys. Chem. Lett.* **2020**, *11*, 387–394.
- (43) Thouin, F.; Neutzner, S.; Cortecchia, D.; Dragomir, V. A.; Soci, C.; Salim, T.; Lam, Y. M.; Leonelli, R.; Petrozza, A.; Kandada, A. R. S.; Silva, C. Stable Biexcitons in Two-Dimensional Metal-Halide Perovskites with Strong Dynamic Lattice Disorder. *Phys. Rev. Mater.* **2018**, *2*, 034001.
- (44) Jia, X.; Jiang, J.; Zhang, Y.; Qiu, J.; Wang, S.; Chen, Z.; Yuan, N.; Ding, J. Observation of Enhanced Hot Phonon Bottleneck Effect in 2D Perovskites. *Applied Physics Letters* **2018**, *112*, 143903.
- (45) Fu, J.; Xu, Q.; Han, G.; Wu, B.; Huan, C. H. A.; Leek, M. L.; Sum, T. C. Hot Carrier Cooling Mechanisms in Halide Perovskites. *Nat. Commun.* **2017**, *8*, 1300.
- (46) Achermann, M.; Bartko, A. P.; Hollingsworth, J. A.; Klimov, V. I. The Effect of Auger Heating on Intraband Carrier Relaxation in Semiconductor Quantum Rods. *Nat. Phys.* **2006**, *2*, 557–561.
- (47) Burgos-Caminal, A.; Moreno-Naranjo, J. M.; Willauer, A. R.; Paraecattil, A. A.; Ajdarzadeh, A.; Moser, J.-E. Hot Carrier Mobility Dynamics Unravel Competing Sub-ps Cooling Processes in Lead Halide Perovskites. *arXiv:1909.04589 [cond-mat, physics:physics]* **2019**.
- (48) Joshi, P. P.; Maehrlein, S. F.; Zhu, X. Dynamic Screening and Slow Cooling of Hot Carriers in Lead Halide Perovskites. *Adv. Mater.* **2019**, 1803054.
- (49) Thouin, F.; Valverde-Chávez, D. A.; Quarti, C.; Cortecchia, D.; Bargigia, I.; Beljonne, D.; Petrozza, A.; Silva, C.; Srimath Kandada, A. R. Phonon Coherences Reveal the Polaronic Character of Excitons in Two-Dimensional Lead Halide Perovskites. *Nat. Mater.* **2019**, *18*, 349–356.

- (50) March, S. A.; Riley, D. B.; Clegg, C.; Webber, D.; Liu, X.; Dobrowolska, M.; Furdyna, J. K.; Hill, I. G.; Hall, K. C. Four-Wave Mixing in Perovskite Photovoltaic Materials Reveals Long Dephasing Times and Weaker Many-Body Interactions than GaAs. *ACS Photonics* **2017**, *4*, 1515–1521.
- (51) Huber, R.; Tauser, F.; Brodschelm, A.; Bichler, M.; Abstreiter, G.; Leitenstorfer, A. How Many-Particle Interactions Develop After Ultrafast Excitation of an Electron-Hole Plasma. *Nature* **2001**, *414*, 286–289.
- (52) Miyata, K.; Meggiolaro, D.; Trinh, M. T.; Joshi, P. P.; Mosconi, E.; Jones, S. C.; Angelis, F. D.; Zhu, X.-Y. Large Polarons in Lead Halide Perovskites. *Sci. Adv.* **2017**, *3*, e1701217.
- (53) Bretschneider, S. A.; Ivanov, I.; Wang, H. I.; Miyata, K.; Zhu, X.; Bonn, M. Quantifying Polaron Formation and Charge Carrier Cooling in Lead-Iodide Perovskites. *Adv. Mater.* **2018**, 1707312.
- (54) Deng, S.; Shi, E.; Yuan, L.; Jin, L.; Dou, L.; Huang, L. Long-Range Exciton Transport and Slow Annihilation in Two-Dimensional Hybrid Perovskites. *Nat. Commun.* **2020**, *11*, 1–8.
- (55) Hopper, T. R.; Gorodetsky, A.; Frost, J. M.; Müller, C.; Lovrincic, R.; Bakulin, A. A. Ultrafast Intraband Spectroscopy of Hot-Carrier Cooling in Lead-Halide Perovskites. *ACS Energy Lett.* **2018**, *3*, 2199–2205.
- (56) Yang, Y.; Ostrowski, D. P.; France, R. M.; Zhu, K.; van de Lagemaat, J.; Luther, J. M.; Beard, M. C. Observation of a Hot-Phonon Bottleneck in Lead-Iodide Perovskites. *Nat. Photonics* **2016**, *10*, 53–59.

Conclusions and outlook

The results of this work have been heavily influenced by the development of an ultra-broadband TRTS setup. While the principles are known from the existing literature, many details have to be rediscovered and tested in order to obtain a functioning setup. Home-made components had to be built and different configurations and alignments had to be tested. The result is a rather exclusive setup that has plenty of potential applications in the study of optoelectronic materials and beyond, as well as a gratifying experience. During this thesis, the setup was used for the characterization of a poorly studied nanomaterial and to shed light on key questions in LHP research.

In chapter 3, Se nanowires produced through a new, simple and direct solution-based approach were characterized with a combination of time-resolved spectroscopic techniques. The charge carrier dynamics were found to be dominated by trapping. This served as a clear example of the decrease in mobility through trapping, where the TRTS signal disappeared while some of the visible ground state bleaching remained. Furthermore, a short range mobility of $3.0 \text{ cm}^2 \text{ V}^{-1} \text{ s}^{-1}$ for free carriers was obtained. Although this considerable mobility is quickly lost, the long lived trapped carriers are believed to move through a hopping type of mechanism. This explains the usefulness of the material in optoelectronic applications. Future research should address the effects of nanowire orientation in both mobility and trapping.

Chapter 4 focused on lead halide perovskites, a family of materials that has gathered much interest both in the photovoltaic research and the ultrafast spectroscopy communities. We studied the rise in photoconductivity that is observed in the first picosecond after photoexcitation taking advantage of the improved time-resolution of ultra-broadband TRTS. The results were compatible with a competition between the previously proposed phenomena of carrier cooling limited by a phonon bottleneck and polaron formation.

From the observation of fluence and wavelength dependencies, a competition model was proposed. The rise time, which was found to be fairly constant across wavelengths and excitation densities, mainly followed the polaron formation time and was sensitive to the nature of the cation. This meant that polaron formation increased the mobility of hot carriers while it remained similar for cold ones.

In chapter 5, 2D perovskites were studied using a combination of ultra-broadband TRTS and FLUPS for the first time. This allowed us to identify the time-scale of carrier cooling and exciton formation in these systems through the analysis of TRTS 2D spectra and the comparison between the two techniques. In addition, the effects of fluence were studied, discarding a Mott transition at the typical ultrafast laser spectroscopy excitation densities. Instead, heavy exciton-exciton interactions, with the continued formation of hot carriers through Auger heating and biexciton formation, were observed. Kinetic modelling through the use of numerical models was again highly useful to test the hypothesis, much like in the previous chapter. In addition, PEA and BuA were compared as cations for 2D perovskites and their prospective applications. The former was found to be both more stable and less prone to a phonon bottleneck effect.

The work carried out in this thesis opens the door for many other experiments and research studies. Here is a selection of what could be done in the near future to either complete or go beyond the presented studies.

First, a deeper study of the TRTS spectra at early times for bulk LHPs should be carried out in order to fully validate the competition between cooling and polaron formation. In addition, it could help understand how these processes affect the mobility.

The work in chapter 5 opens the door for similar analysis in other confined systems such as LHP nanoparticles or transition metal dichalcogenides. It would be especially interesting to study a material where E_b is low enough to observe transitions in the 20 THz window while being high enough to stabilize excitons at room temperature. This would allow one to study such optoelectronic materials closer to device operating conditions. One such material could be ZnO, with an E_b of 60 meV (14.5 THz).

Lastly, another type of experiment that could have been explored is the visible-pump near-IR-push THz-probe configuration for TRTS, thanks to the two available OPAs. Time limitations as well as the need to first understand the pump-probe experiments excluded these from this work. Indeed, pump-push-probe could help in the understanding of carrier cooling, polaron formation, carrier trapping/detrapping and exciton formation as well as multiple other phenomena.

Acknowledgments

First of all, I would like to thank Prof. Jacques-E. Moser for the opportunity to carry out my PhD in his group. I have always felt very welcome in his group and I appreciate all the support that I received. I could always pursue my own ideas as well as receive advice when I needed.

I would also like to thank Prof. Enrique Cánovas, Prof. Thomas Feurer and Prof. Majed Chergui for reading this work and participating in the oral exam as well as giving detailed suggestions and corrections. Likewise, I would like to thank Prof. Anders Hagfeldt for being the president of the jury.

To my old generation of labmates, who made the group a nice place to stay for a full PhD. Arun, we had our fun with our pointless discussions. Marine, always eager to discuss sciency stuff, I have learnt much in the field from you. I will always miss the coffee breaks with you two. Ahmad, who worked with me on the ultra-broadband TRTS setup and who taught me much on laser maintenance and alignment. Joël, always there to help on any technical or programming problem. Heewon, who was always a friendly presence in the lab, sorry the THz measurements on TiO_2 did not really work out. Mahsa, very positive and friendly, I think there are still people coming to sell optical components from time to time.

During a PhD, it is common to be for some time both the newcomer and the senior. This means that you have to say good bye to old colleagues and welcome new ones. I have to say that the new generation brought a very positive revitalization to the lab, which was starting to get empty. George, with his good humor and positive spirit. You gave us a lot of fun times with the prank wars. I hope you take good care of the THz setup. Etienne, always friendly and happy to collaborate, your measurements are a key

part of the last chapter. I wish we could have continued this THz-FLUPS dynamic for another year. Brener, aka B-Dog, probably the biggest source of fun in the group but at the same time someone you can have a nice science discussion or everyday conversation. It was really a pity you had to leave after barely a year. Vincent, my new office-mate, always nice and interesting to talk to. Luckily, you were not always at EPFL, otherwise we would not have got much work done. Juanma, who started as a project student and became one more in our group of friends. You made me feel short for a change.

I also thank my students Juanma, Aurélien and Quentin, for their hard work and motivation. I hope we learnt some things together.

To Wei and Tapa for proposing a very nice collaboration. I really enjoyed our work together. Also, to Arun and Linfeng for providing SEM pictures.

To Madeleine and Fara, who have to endure our administrative ignorance and forgetfulness. Thank you for everything you do.

Additional thanks to Jacques and George for reviewing this thesis.

A mis padres por darme todo lo que he necesitado para llegar hasta aquí. Por despertar mi curiosidad desde pequeño y por su apoyo todos estos años.

A Sandra por su apoyo, cariño y paciencia estos largos años de vuelos cada fin de semana.

Appendices

Appendix A

Supplementary figures and tables

A.1 THz setup

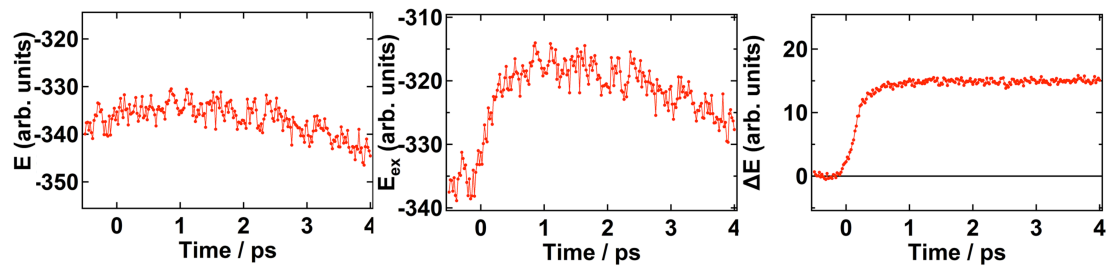


Figure A.1: Noise cancellation with the simultaneous acquisition of E and E_{ex} to obtain ΔE .

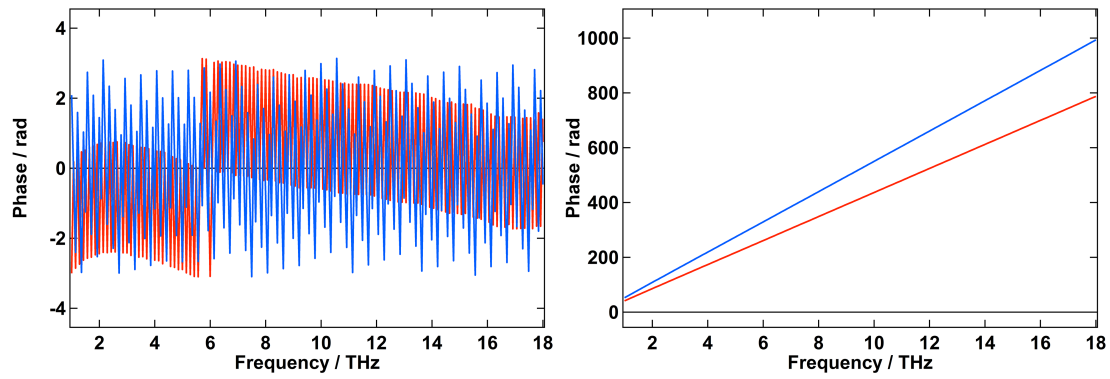


Figure A.2: Phase before (left) and after (right) correcting for the discontinuities.

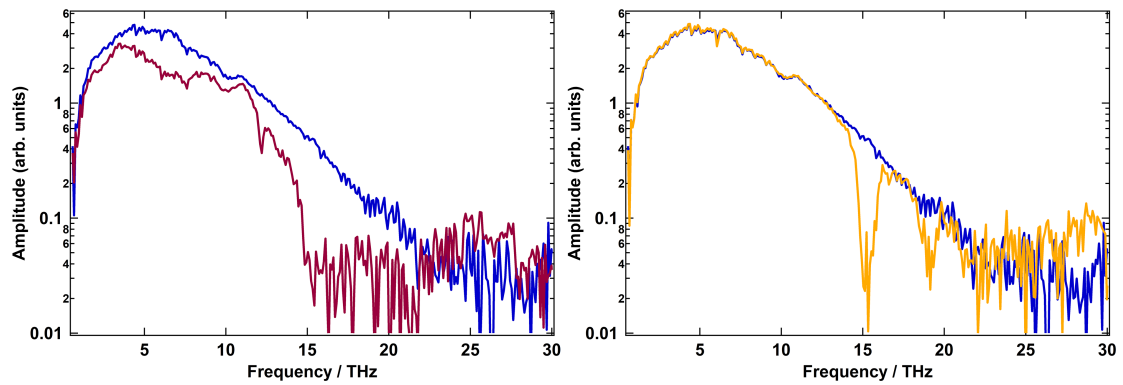


Figure A.3: THz transmission through a PS cuvette (left) and a PTFE film (right). In the PTFE data clear vibrational transitions are observable.

A.2 Charge carrier dynamics and mobilities in Se nanowires

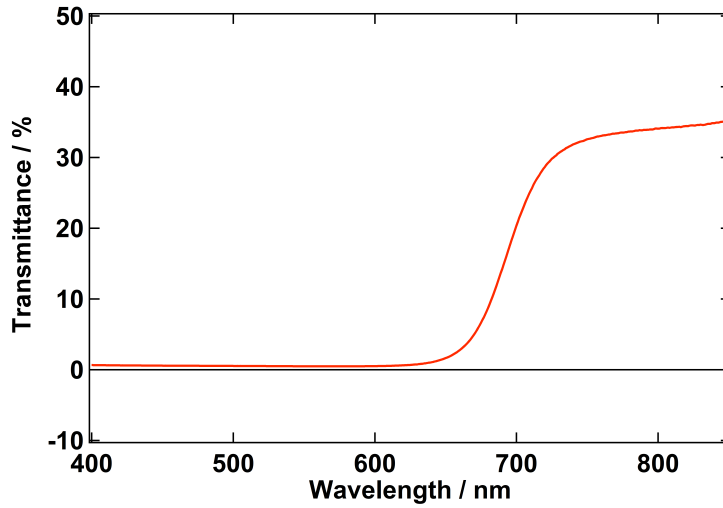


Figure A.4: Transmittance spectrum of the 430 nm film, corresponding to the absorbance shown in Figure 3.2. The absorption is practically saturated above the bandgap with the transmitted light very close to zero.

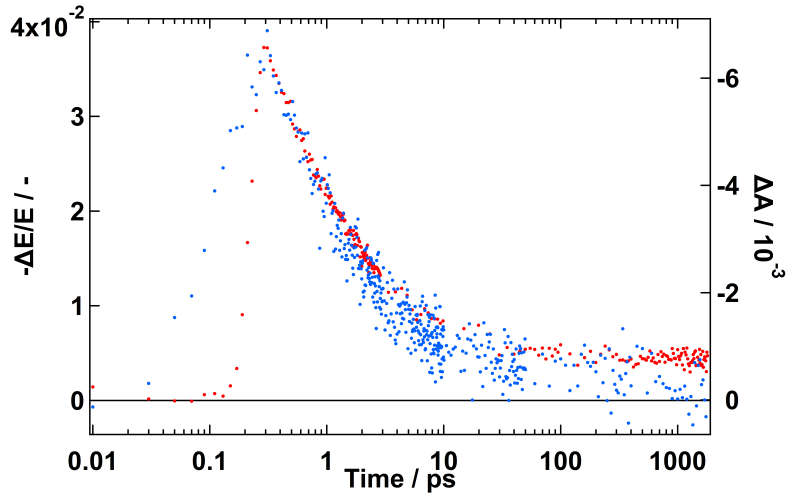


Figure A.5: TAS results compared to the TRTS results at a lower fluence ($F = 142 \mu\text{J cm}^{-2}$). The same conclusions can be drawn as the TRTS signal equally decreases to zero.

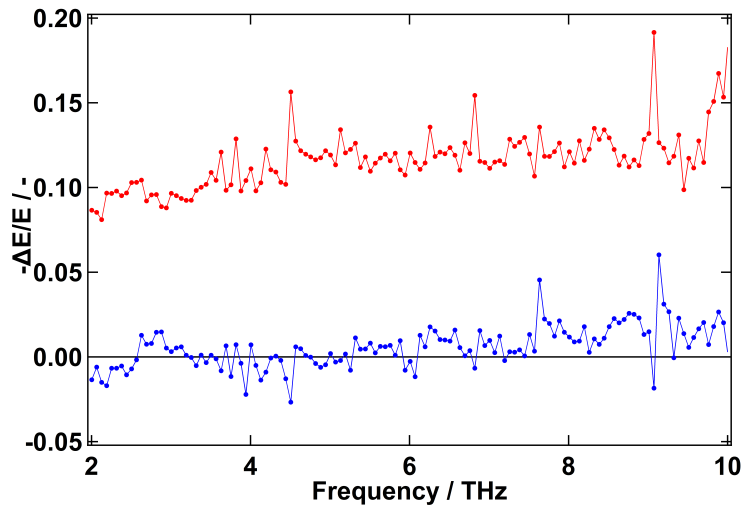


Figure A.6: The real (red) and imaginary (blue) parts of the photoconductivity spectrum are approximately flat, which agrees with a moderately low mobility. In addition, it justifies following the frequency-averaged dynamics on the maximum E point.

A.3 Hot carrier dynamics in bulk lead halide perovskites

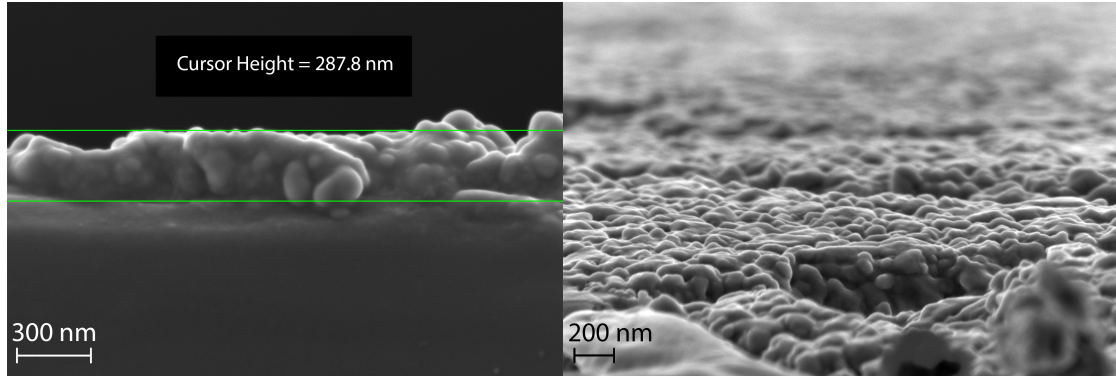


Figure A.7: SEM cross-section (left) and surface (right) pictures of the $\text{CH}_3\text{NH}_3\text{PbI}_3$ film sample. The thickness of the perovskite layers is between 250 and 300 nm. The film is polycrystalline with grains close to 100 nm in diameter. The grains are slightly blurred due to a carbon coating treatment.

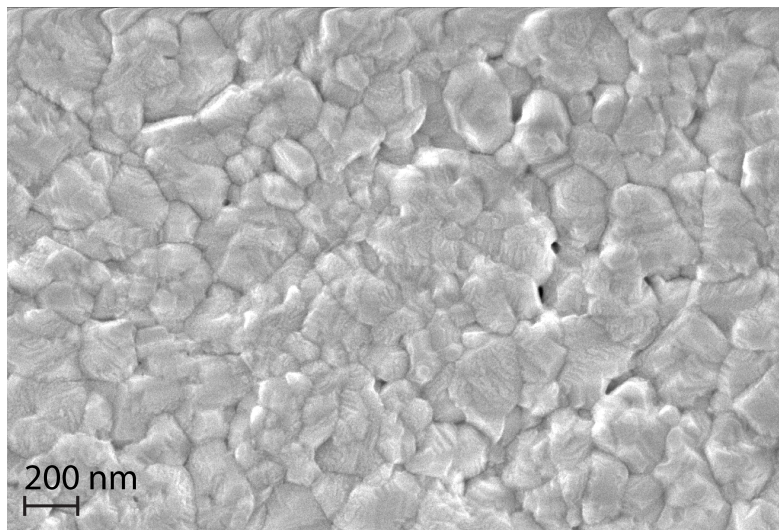


Figure A.8: Top SEM view of a $\text{CH}_3\text{NH}_3\text{PbI}_3$ sample where the crystals of more than 100 nm are more clearly observed without coating treatment.

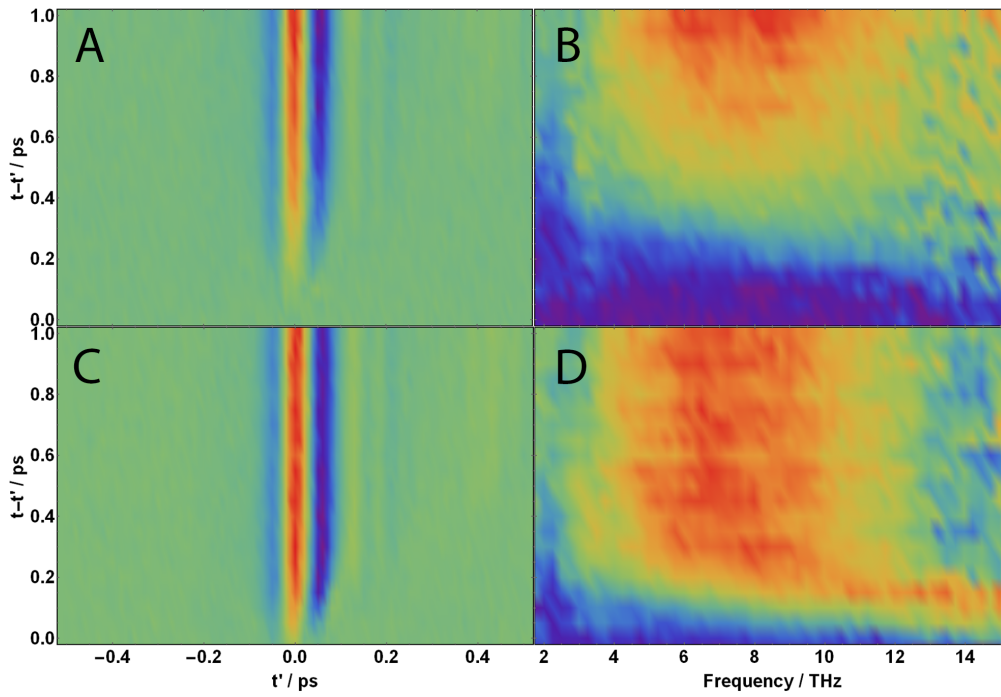


Figure A.9: 2D maps of the first ps after photoexcitation at $\lambda_{\text{exc}} = 510$ nm (A,B) and $\lambda_{\text{exc}} = 740$ nm (C,D). A and C show the $\Delta E(t)$ waveform while B and D show the corresponding magnitude of the complex $-\Delta E(\omega)/E(\omega)$ spectra.

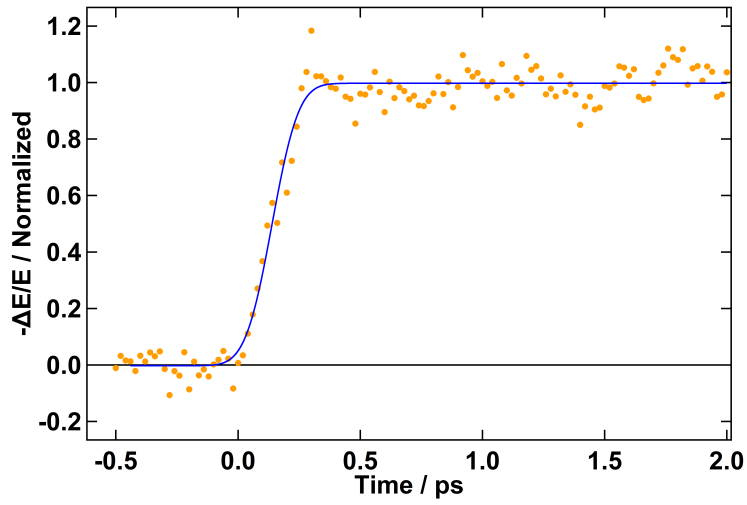


Figure A.10: The rise of the photoconductivity on $\text{CH}_3\text{NH}_3\text{PbI}_3$ ($\lambda_{\text{exc}} = 760 \text{ nm}$) can be well fitted to a very quick rise convoluted with a Gaussian having a FWHM of 200 fs.

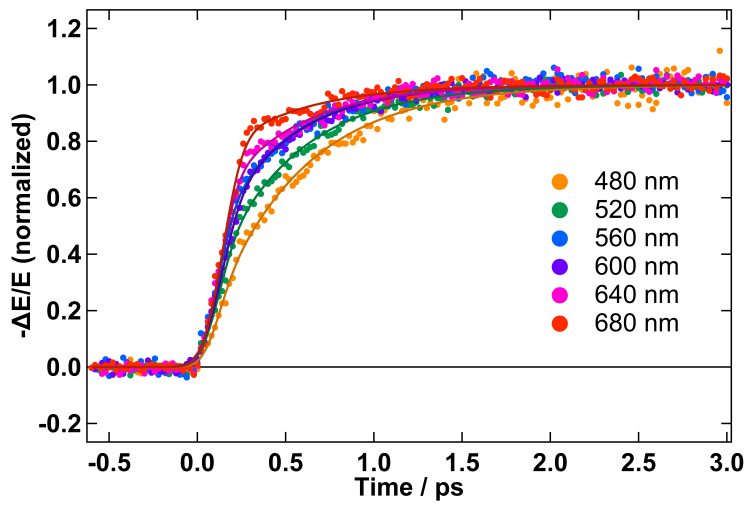


Figure A.11: Fits resulting from the application of the simple model on the data shown in Figure 4.2.

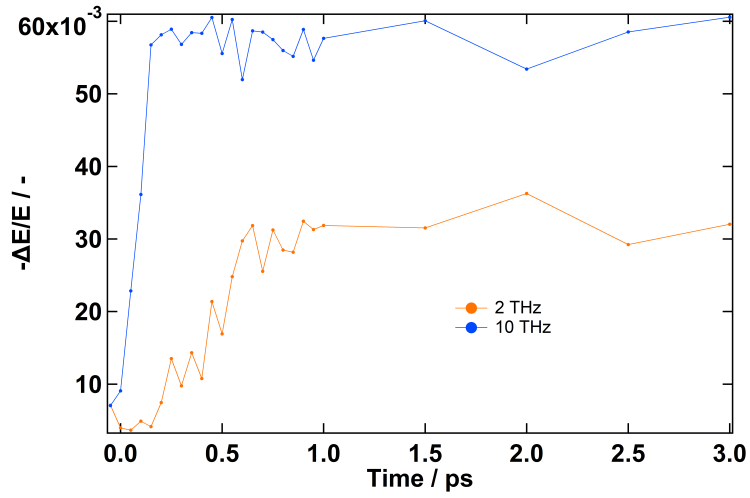


Figure A.12: Delayed rise of the photoconductivity at 2 THz compared to that at 10 THz on $\text{CH}_3\text{NH}_3\text{PbI}_3$ ($\lambda_{\text{exc}} = 740$ nm).

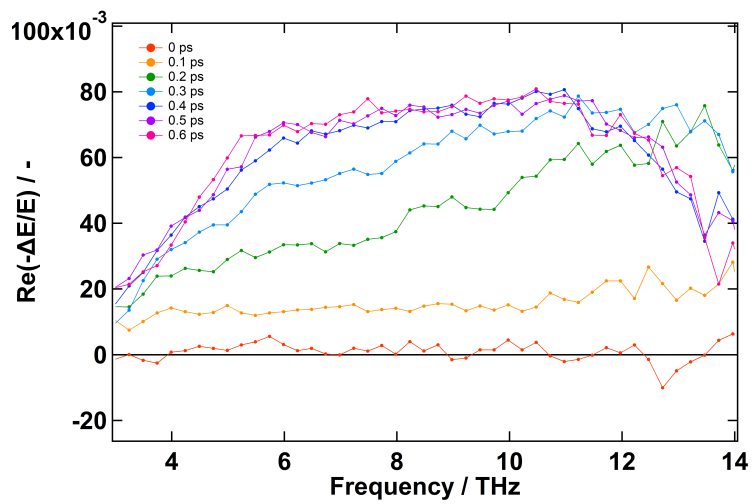


Figure A.13: Change of the photoconductivity spectrum in the first hundred femtoseconds on $\text{CH}_3\text{NH}_3\text{PbI}_3$ ($\lambda_{\text{exc}} = 740$ nm).

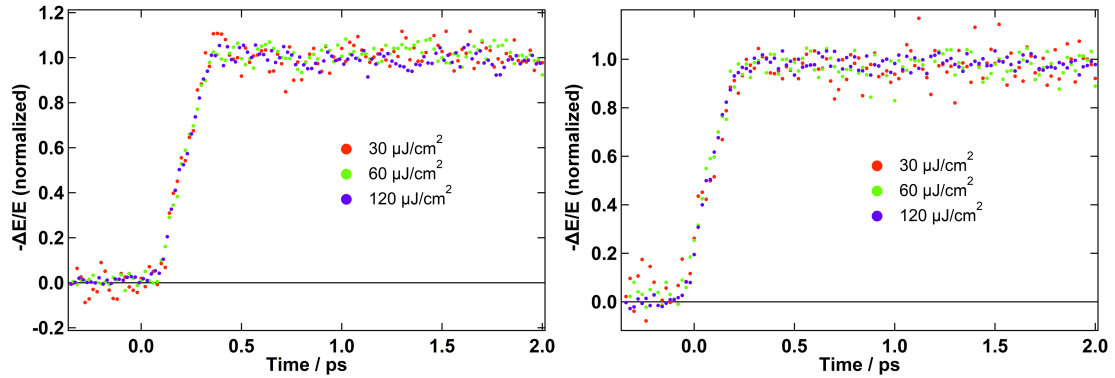


Figure A.14: Fluence dependence of the THz absorptance signal at resonant excitation for $\text{CH}_3\text{NH}_3\text{PbBr}_3$ ($\lambda_{\text{exc}} = 520$ nm, left) and CsPbBr_3 ($\lambda_{\text{exc}} = 510$ nm, right). No dependence of the time evolution is observed.

A.4 Exciton-carrier dynamics in lead halide 2D perovskites

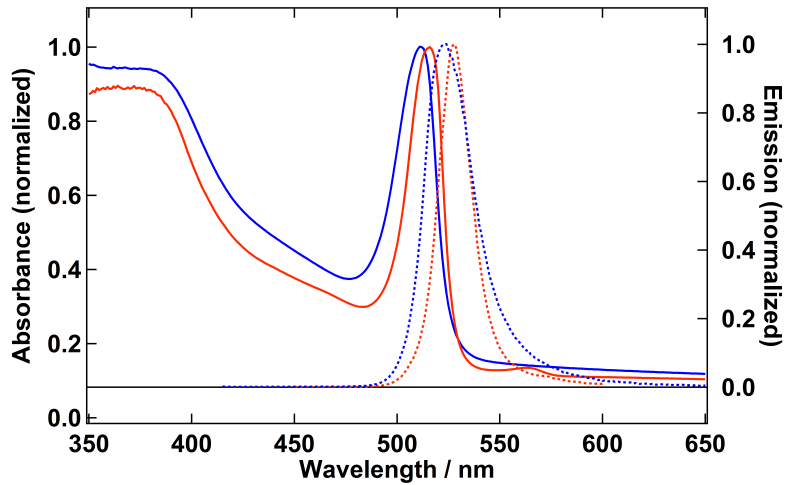


Figure A.15: Absorption (solid) and Emission (dashed) spectra of PEA_2PbI_4 (red) and BuA_2PbI_4 (blue).

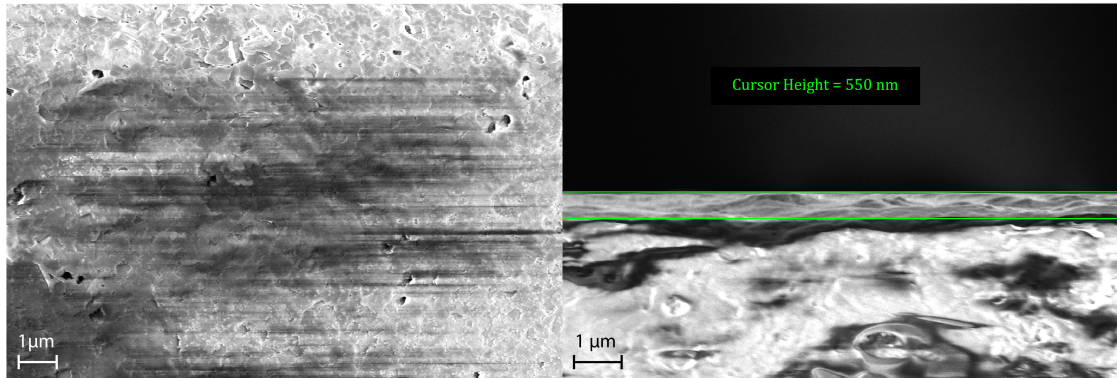


Figure A.16: Left) SEM picture of PEA_2PbI_4 . The flat microscopic crystals appear to lay horizontal to the surface. Right) Cross-sectional SEM showing a thickness of 550 nm for the PEA_2PbI_4 film.

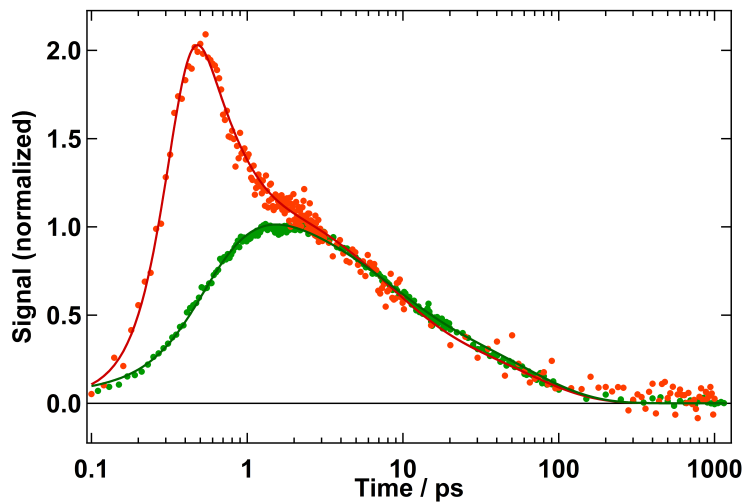


Figure A.17: Full view of the decay in Figure 5.1, left, with a different normalization to highlight the coinciding decays.

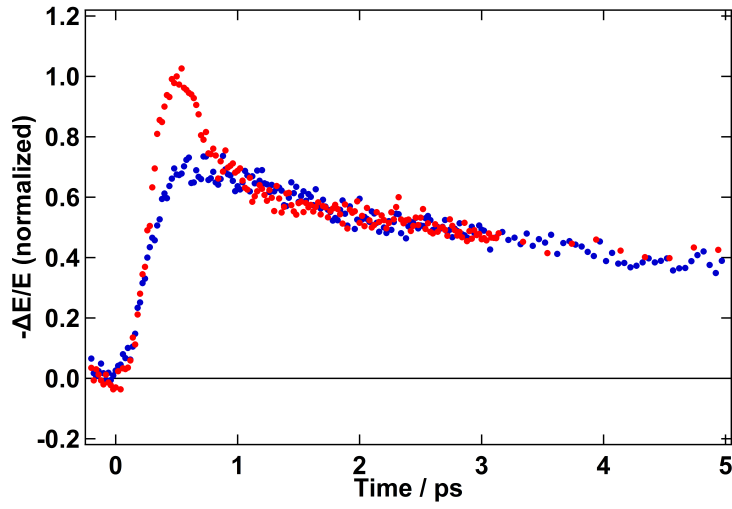


Figure A.18: Figure 5.1, right, with a different normalization to highlight that the main difference lies in the initial decay.

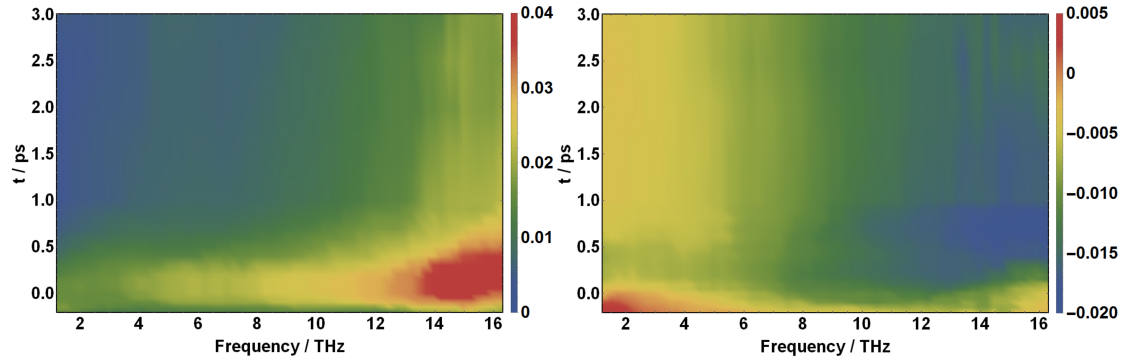


Figure A.19: 2D maps of the real (left) and imaginary (right) parts of $-\Delta E/E$ corresponding to the data in Figure 2. The maps have been cleaned with a median filter.

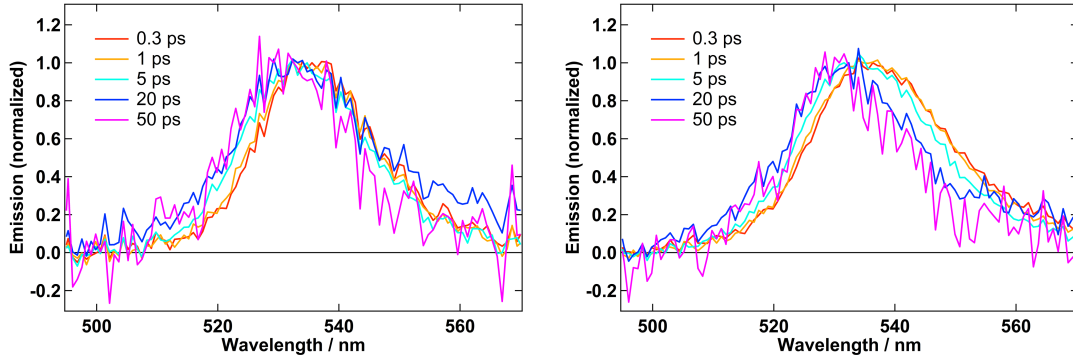


Figure A.20: Normalized emission at $28 \mu\text{J cm}^{-2}$ (left) and $120 \mu\text{J cm}^{-2}$ (right) for different time delays. There is an appreciable blue-shift that is not fluence dependent. The biexcitonic contribution on the red side is clearly dependent on the fluence and follows different kinetics.

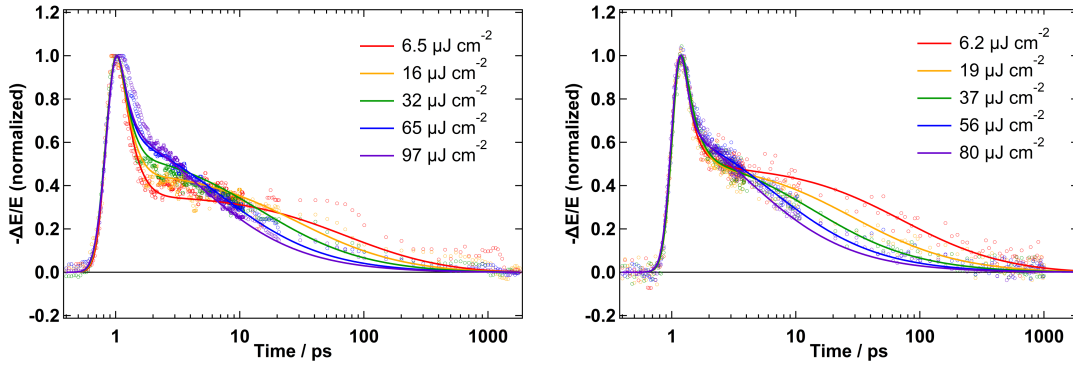


Figure A.21: BuA_2PbI_4 TRTS dynamics globally fitted using a single value for k_c . Clearly, there is a deviation between the fit and the data at early times. Right) PEA_2PbI_4 TRTS dynamics globally fitted using different values for k_c . The results do not vary substantially from the results with only one k_c , unlike BuA_2PbI_4 (Figure 5.6.C and Figure 5.8).

Appendix B

Additional derivations

B.1 Current density from Maxwell's equations

Let us consider a thin film sample on a substrate where a passing linearly polarized THz pulse $E_{in}(z, t)$ produces a current density $J(t)$ in the x direction. The geometry is given by Figure B.1.

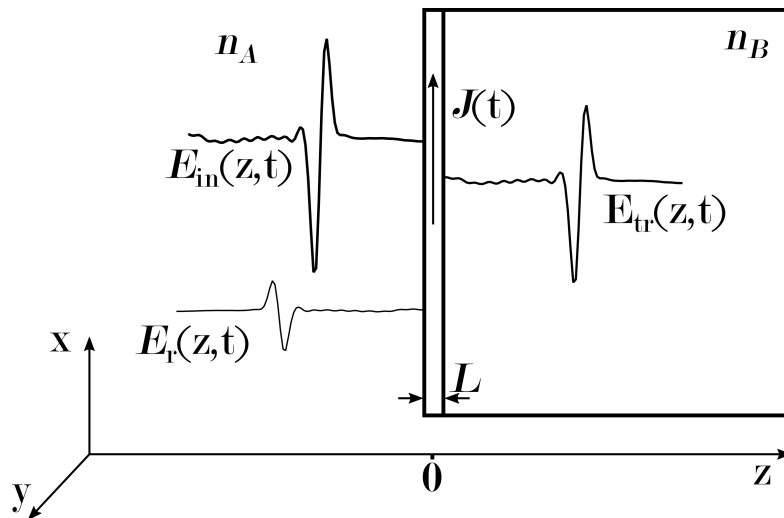


Figure B.1: Geometry of simple linearly polarized THz pulse producing a current on a thin film.

We can obtain an expression for the current density as a function of electric field through

Maxwell's equations

$$\nabla \times E + \frac{\partial B}{\partial t} = 0, \quad (\text{B.1})$$

$$\nabla \times H - \frac{\partial D}{\partial t} = J. \quad (\text{B.2})$$

Where, respectively, E and H are the electric and magnetic fields, B is the magnetic flux and D is the electric displacement. The latter can be expressed as $B = \mu H$ and $D = \varepsilon E$, where μ is the magnetic permeability and ε is the electric permittivity. Finally, J is the previously mentioned current density. According to the simplified case represented in Figure B.1, E is only present in the x direction while H (and therefore B) is consequently in the y . Both are a function of time, t , and z . Therefore,

$$\nabla \times E = \left(\frac{\partial E_z}{\partial y} - \frac{\partial E_y}{\partial z}, \frac{\partial E_x}{\partial z} - \frac{\partial E_z}{\partial x}, \frac{\partial E_y}{\partial x} - \frac{\partial E_x}{\partial y} \right) = \left(0, \frac{\partial E_x}{\partial z}, 0 \right), \quad (\text{B.3})$$

$$\frac{\partial E_x}{\partial z} = -\frac{\partial B_y}{\partial t}. \quad (\text{B.4})$$

Similarly, we find that

$$\nabla \times H = \frac{1}{\mu} \nabla \times B = \left(-\frac{1}{\mu} \frac{\partial B_y}{\partial z}, 0, 0 \right). \quad (\text{B.5})$$

We can change E_x and B_y to $E(z, t)$ and $B(z, t)$ and forget about the specific directions. Since $D = \varepsilon E$ we can obtain the new Maxwell's equations for this geometry where

$$\frac{\partial E(z, t)}{\partial z} = -\frac{\partial B(z, t)}{\partial t}, \quad (\text{B.6})$$

$$-\frac{1}{\mu} \frac{\partial B(z, t)}{\partial z} - \varepsilon \frac{\partial E(z, t)}{\partial t} = J(z, t). \quad (\text{B.7})$$

In order to substitute we need to differentiate both equations so that

$$\frac{\partial^2 E(z, t)}{\partial z^2} = -\frac{\partial^2 B(z, t)}{\partial t \partial z}, \quad (\text{B.8})$$

$$-\frac{1}{\mu} \frac{\partial^2 B(z, t)}{\partial t \partial z} - \varepsilon \frac{\partial^2 E(z, t)}{\partial t^2} = \frac{\partial J(z, t)}{\partial t}. \quad (\text{B.9})$$

After some rearrangement, knowing that $\mu = 1/c^2 \varepsilon_0^2$, we obtain that

$$-\varepsilon_r \frac{\partial^2 E(z, t)}{\partial t^2} + c^2 \frac{\partial^2 E(z, t)}{\partial z^2} = \frac{1}{\varepsilon_0} \frac{\partial J(z, t)}{\partial t}. \quad (\text{B.10})$$

This equation constitutes the basis to obtain Equation 2.22. If we assume that we have a thin sample where all the current appears at $z \approx 0$, we can simplify $J(z, t)$ so that

$$J(z, t) = LJ(t)\delta(z), \quad (\text{B.11})$$

where L is the sample thickness. Another key assumption is that the sample has a negligible absorption. Therefore, the THz pulses can be considered as propagating wave packets with two distinct regimes. For $z < 0$ we have an incident pulse $E_{in}(z, t) = A_{in}(t - zn_A/c)$ and a reflected pulse $E_r(z, t) = A_r(t + zn_A/c)$, while at $z > 0$ we have the transmitted pulse $E_{tr}(z, t) = A_{tr}(t - zn_B/c)$, where the A determines the pulse shape. We can write

$$E(z, t) = \begin{cases} A_{in}(t - zn_A/c) + A_r(t + zn_A/c) & \text{for } z < 0 \\ A_{tr}(t - zn_B/c) & \text{for } z > 0 \end{cases}. \quad (\text{B.12})$$

We have the boundary condition that E is continuous at $z = 0$ and thus $A_{in}(t) + A_r(t) = A_{tr}(t)$, meaning that we can substitute and

$$E(z, t) = \begin{cases} A_{in}(t - zn_A/c) + A_r(t + zn_A/c) & \text{for } z < 0 \\ A_{in}(t - zn_B/c) + A_r(t - zn_B/c) & \text{for } z > 0 \end{cases}. \quad (\text{B.13})$$

Let's focus first on the derivative with respect to z . The first derivative is straightforward.

$$\frac{\partial E(z, t)}{\partial z} = \begin{cases} -\frac{n_A}{c} A'_{in}(t - zn_A/c) + \frac{n_A}{c} A'_r(t + zn_A/c) & \text{for } z < 0 \\ -\frac{n_B}{c} A'_{in}(t - zn_B/c) + -\frac{n_B}{c} A'_r(t - zn_B/c) & \text{for } z > 0 \end{cases}. \quad (\text{B.14})$$

Now, for the second derivative, it is slightly more complex. $\frac{\partial E(z, t)}{\partial z}$ is not continuous anymore, it has different values above and below $z = 0$, as can be seen by the coefficients in Equation B.14. We are only interested in $z = 0$. Given a discontinuous function f , the derivative can be expressed as a function of a δ such that $\partial f(z = 0)/\partial z = (f(+0) - f(-0))\delta(z)$. Thus

$$\frac{\partial^2 E(z, t)}{\partial z^2} = \left(\left(-\frac{n_A}{c} A'_{in}(t) + \frac{n_A}{c} A'_r(t) \right) - \left(-\frac{n_B}{c} A'_{in}(t) + -\frac{n_B}{c} A'_r(t) \right) \right) \delta(z) \text{ at } z=0. \quad (\text{B.15})$$

Going back to Equation B.10, a sum where one of the two terms contains a δ (an infinite value) can be simplified dropping the value without δ . Thus, it is unnecessary to determine $\frac{\partial^2 E(z, t)}{\partial t^2}$, and

$$c^2 \frac{\partial^2 E(z, t)}{\partial z^2} = \frac{1}{\varepsilon_0} \frac{\partial J(z, t)}{\partial t}. \quad (\text{B.16})$$

Equations B.11, B.15 and B.16 can be combined with $A'_r(t) = A'_{tr}(t) - A'_{in}(t)$ to give

$$\frac{L}{c\varepsilon_0}J'(t) = 2n_A A'_{in}(t) - (n_A + n_B)A'_{tr}(t). \quad (\text{B.17})$$

Then, assuming that $J(-\infty) = 0 = A(-\infty)$, if both derivatives are the same and they have the same value at a certain t we can directly say that

$$\frac{L}{c\varepsilon_0}J(t) = 2n_A A_{in}(t) - (n_A + n_B)A_{tr}(t). \quad (\text{B.18})$$

Finally, we are interested to know the current difference upon photoexcitation, where the transmitted field will be different. We can define $J(t)$ and $J_0(t)$ as well as $A_{tr}(t)$ and $A_{tr0}(t)$ for the photoexcited and non-photoexcited cases ($A_{in}(t)$ will not change). If we assume that initially the generated current is $J_0(t) = 0$, then we obtain that

$$J(t) = -\frac{\varepsilon_0 c(n_A + n_B)}{L}(A_{tr}(t) - A_{tr0}(t)), \quad (\text{B.19})$$

which is none other than Equation 2.22.

B.2 Refractive index

From the definition of the refractive index, we can easily derive an equation to obtain the refractive index by comparing it to a known medium (such as air) and obtaining the time-shift.

$$\begin{aligned} n &= \frac{c}{v} \\ n - n_r &= \frac{c}{v} - \frac{c}{v_r} \\ n - n_r &= \frac{c}{\frac{L}{t-t_0}} - \frac{c}{\frac{L}{t_r-t_0}} \\ n - n_r &= \frac{c}{L}(t - t_0 - (t_r - t_0)) \\ n - n_r &= \frac{c}{L}\Delta t \\ n &= \frac{c}{L}\Delta t + n_r \end{aligned} \quad (\text{B.20})$$

B.3 Models in frequency

The different models obtained from a Fourier transform like the one in Equation 2.39 are given in angular frequency (ω). Simple conversions are given next to obtain the frequency (ν) dependent functions.

Drude

$$\begin{aligned}\sigma(\omega) &= \frac{\varepsilon_0 \omega_p^2 \tau}{1 - i\omega\tau} \\ \sigma(\nu) &= \frac{\varepsilon_0 \omega_p^2 \tau}{1 - i2\pi\nu\tau}\end{aligned}\tag{B.21}$$

Drude-Smith

$$\begin{aligned}\sigma(\omega) &= \frac{\varepsilon_0 \omega_p^2 \tau}{(1 - i\omega\tau)} \left(1 + \frac{c}{1 - i\omega\tau} \right) \\ \sigma(\nu) &= \frac{\varepsilon_0 \omega_p^2 \tau}{(1 - i2\pi\nu\tau)} \left(1 + \frac{c}{1 - i2\pi\nu\tau} \right)\end{aligned}\tag{B.22}$$

Lorentzian oscillator

Defining a new Amplitude A_ν and converting the other constants to frequency (ν_0 and γ_ν) we obtain an identical expression for $\sigma(\nu)$.

$$\begin{aligned}\sigma(\omega) &= \frac{Ai\omega}{\omega^2 - \omega_0^2 + i\gamma\omega}, \\ \sigma(\nu) &= \frac{Ai2\pi\nu}{4\pi^2\nu^2 - 4\pi^2\nu_0^2 + i4\pi^2\gamma_\nu\nu}, \\ \sigma(\nu) &= \frac{Ai\nu}{2\pi\nu^2 - 2\pi\nu_0^2 + i2\pi\gamma_\nu\nu}, \\ \sigma(\nu) &= \frac{A}{2\pi} \frac{i\nu}{\nu^2 - \nu_0^2 + i\gamma_\nu\nu}, \\ \sigma(\nu) &= \frac{A_\nu i\nu}{\nu^2 - \nu_0^2 + i\gamma_\nu\nu}.\end{aligned}\tag{B.23}$$

B.4 Exponential equations

Sometimes, it is enough to model a system with generalized exponential equations, such as in the Se nanowire chapter. A simple exponential decay has the form

$$S(t) = Ae^{-\frac{t-t_0}{\tau}},\tag{B.24}$$

where τ is the lifetime, t_0 is the time zero and A is the amplitude. In order to fit data limited by a certain time-resolution we can use the convolution of Equation B.24 with a

Gaussian of the form

$$g(t) = \frac{1}{\sigma\sqrt{2\pi}} e^{-\frac{(t-t_0)^2}{2\sigma^2}}, \quad (\text{B.25})$$

to give

$$S(t) = A \frac{1}{2} \exp\left(\frac{\sigma^2}{2\tau^2} - \frac{t-t_0}{\tau}\right) \left(1 + \operatorname{erf}\left(\frac{t-t_0}{\sqrt{2}\sigma} - \frac{\sigma}{\sqrt{2}\tau}\right)\right), \quad (\text{B.26})$$

where σ is the standard deviation of the Gaussian. Linear combinations of Equation B.26 can be used to model multi-exponential behavior. When analyzing data it is important to take into account that linear combinations of 3 or more exponentials can give good fits for traces that are actually following complex non-exponential kinetics. It should be considered carefully before assigning 3 lifetimes to 3 different processes. Indeed, a bimolecular process may equally be well fitted with 3 exponentials but the fitted constants are not really related to the actual kinetic constants of the process.

B.5 Simple carrier cooling model

As a first attempt, we can consider a simple model taking into account only hot and cold carriers, whose populations N_H and N_C , respectively, evolve according to

$$\frac{dN_H}{dt} = -\frac{1}{\tau} N_H(t), \quad (\text{B.27})$$

$$\frac{dN_C}{dt} = \frac{1}{\tau} N_C(t). \quad (\text{B.28})$$

With the initial conditions $N_H(0) = N_H^0$ and $N_C(0) = 1 - N_H^0$, we obtain

$$N_H(t) = N_H^0 e^{-\frac{t}{\tau}}, \quad (\text{B.29})$$

$$N_C(t) = 1 - N_H^0 e^{-\frac{t}{\tau}}. \quad (\text{B.30})$$

The assumption that both hot and cold carriers will give a signal, albeit proportionally different to the concentration due to the different mobilities, is reasonable. Thus, for a normalized dataset, we can define the model for the sample conductivity

$$S(t) = 1 - N_H^0 e^{-\frac{t}{\tau}} + b N_H^0 e^{-\frac{t}{\tau}}, \quad (\text{B.31})$$

where b is a proportionality constant due to the different mobilities. However, b and N_H^0 are mutually dependent and cannot be determined through a fit. Thus, further simplification of the model with the substitution $B = (1-b)N_H^0$ is necessary, yielding a single exponential

$$S(t) = 1 - B e^{-\frac{t}{\tau}}. \quad (\text{B.32})$$

If b or N_H^0 can be determined from a separate method, then the other parameter can be calculated. After convoluting the exponential equation (Equation B.32) with a Gaussian function of the form

$$g(t) = \frac{2}{w} \sqrt{\frac{\ln(2)}{\pi}} e^{-\frac{4\ln(2)t^2}{w^2}}, \quad (\text{B.33})$$

representing the cross-correlation between the pump and the THz probe pulses, and where w is the FWHM, we obtain the equation to be fitted to the observed dynamics

$$S(t) = \frac{1}{2} \left(1 + \operatorname{erf} \left[2(t - t_0) \sqrt{\frac{\ln(2)}{w^2}} \right] - B \exp \left[\frac{w^2 \left(1 - \frac{16(t-t_0)\tau \ln(2)}{w^2} \right)}{16\tau^2 \ln(2)} \right] \operatorname{erfc} \left[\frac{1 - \frac{8(t-t_0)\tau \ln(2)}{w^2}}{4\tau \sqrt{\frac{\ln(2)}{w^2}}} \right] \right). \quad (\text{B.34})$$

B.6 Competition model

The competition model is obtained by numerically solving the system of five differential equations (Equations B.35 to B.39), where N_{hc} , N_{cc} , N_{loph} , N_{hp} , and N_{cp} correspond to the populations of the hot carriers, cold carriers, LO phonons, hot polarons, and cold polarons, respectively. The rate constants k_1 , k_{-1} , k_2 , k_3 , and k_4 characterize the processes depicted in Figure 4.6.

$$\frac{dN_{hc}(t)}{dt} = -k_1 N_{hc}(t) + k_{-1} N_{cc}(t) N_{loph}(t) - k_2 N_{hc}(t), \quad (\text{B.35})$$

$$\frac{dN_{cc}(t)}{dt} = k_1 N_{hc}(t) - k_{-1} N_{cc}(t) N_{loph}(t) - k_2 N_{hc}(t), \quad (\text{B.36})$$

$$\frac{dN_{loph}(t)}{dt} = k_1 N_{hc}(t) - k_{-1} N_{cc}(t) N_{loph}(t) - k_3 N_{loph}(t), \quad (\text{B.37})$$

$$\frac{dN_{hp}(t)}{dt} = k_2 N_{hc}(t) - k_4 N_{hp}(t), \quad (\text{B.38})$$

$$\frac{dN_{cp}(t)}{dt} = k_2 N_{cc}(t) - k_4 N_{hp}(t). \quad (\text{B.39})$$

The conductivity signal $S(t)$ is finally approximated by considering that hot polarons, cold carriers, and cold polarons have the same mobility:

$$S(t) = N_{hp}(t) + a N_{hc}(t) + N_{cp}(t) + N_{cc}(t). \quad (\text{B.40})$$

The data were fitted to the model using Wolfram Mathematica software. The differential equations were written following the model depicted in Figure 4.6 and numerically solved

for an interval covering the data. The signal was simulated as a normalized and weighted sum of the different carrier densities with the condition that it equals zero for times earlier than t_0 . The result was numerically convoluted with a Gaussian function to account for the IRF. An interpolation function was fitted to the results to calculate the value at any times inside the calculated interval. A small time step of 0.005 ps was used for the calculation, which was shown to be sufficient to obtain results identical to those with simpler functions for which an analytical solution is possible. The function was programmed such that once the interpolation function had been obtained, for a given set of parameters, it could be called to obtain the values at different times. Therefore, the resulting overall function could be used not only to simulate the signal but also to fit the data.

B.7 Kinetic model for 2D perovskites

The kinetic model presented in Chapter 5 is based on following the densities of excitons (N_{ex}), hot carriers (N_{hc}) and cold carriers (N_{cc}) over time (t). Thus, we define three rate equations

$$\frac{dN_{ex}(t)}{dt} = a(G(t))_{510 \text{ nm}} + k_{ef}N_{cc}(t)^2 - k_{er}N_{ex}(t) - k_aN_{ex}(t)^2 - k_{ed}N_{ex}(t), \quad (\text{B.41})$$

$$\frac{dN_{hc}(t)}{dt} = a(G(t))_{400 \text{ nm}} + k_aN_{ex}(t)^2 - k_cN_{hc}(t), \quad (\text{B.42})$$

$$\frac{dN_{cc}(t)}{dt} = -2k_{ef}N_{cc}(t)^2 + k_cN_{hc}(t) + 2k_{ed}N_{ex}(t), \quad (\text{B.43})$$

where k_{ef} , k_{er} , k_a , k_{ed} and k_c are the kinetic constants for exciton formation, exciton recombination, exciton-exciton annihilation, exciton dissociation and carrier cooling, respectively. In addition, $G(t)$ is the generation term and it is defined as

$$G(t) = \sqrt{\frac{4 \log(2)}{\pi w^2}} \exp\left(-\frac{4 \log(2)(t - t_0)^2}{w^2}\right), \quad (\text{B.44})$$

where w is the FWHM of the Gaussian. A term “2” is used to indicate that two carriers are taken or generated when one exciton is formed or dissociated. Alternatively, no such term is used for the auger process since two excitons turn into two hot carriers. Furthermore, k_{ed} is considered to be effectively zero, due to the large E_b (270 meV). We can approximately consider that $k_{ed} = k_{ef} / \exp(-\frac{E_b}{k_B T}) = k_{ef} / 4.4 \cdot 10^4 \approx 0$.

The signal is expressed as $S = N_{cc} + c_{hc}N_{hc} + c_{ex}N_{ex}$, where c_{ex} and c_{hc} are the proportionality coefficients for excitons and hot carriers, respectively. a is the amplitude coefficient in density units. It serves as a measure of the fluence. During the global fit, only one value of a is fitted for each wavelength. The different values for each fluence are obtained multiplying that value by a coefficient $b = F_i/F_0$ where F_i is the fluence used in that particular trace and F_0 is the lowest fluence used.

The equations are solved numerically and fitted using home-written code in Wolfram Mathematica.

Appendix C

List of symbols and abbreviations

- a Relative hot carrier signal strength parameter (Bulk perovskites)
- a_{400nm} Fitted amplitude for the 400 nm data (2D perovskites)
- a_{510nm} Fitted amplitude for the 510 nm data (2D perovskites)
- A Absorbance / Amplitude
- A Small monovalent cation
- ABCD Air biased coherent detection
- b Relative fluence coefficient (2D perovskites)
- B Amplitude for the simple exponential rise model
- B Magnetic flux
- B Divalent cation (lead)
- BBO Beta barium borate crystal
- BuA Butylammonium
- c Speed of light / Drude-Smith back-scattering fraction parameter
- c_{ex} Relative exciton signal strength parameter (2D perovskites)
- c_{hc} Relative hot carrier signal strength parameter (2D perovskites)
- CBM Conduction band minimum
- CCD Charge coupled device (detector)
- CIGS Copper indium gallium selenide solar cell
- CPA Chirped-pulse amplified
- d Distance
- D Electric displacement
- DAST 4-N,N-dimethylamino-4'-N-methylstilbazolium tosylate
- DC Direct current

DMSO	Dimethyl sulfoxide
DSSC	Dye-sensitized solar cell
DJ	Dion-Jacobson phase
DWP	Ultra-thin dual wavelength waveplate
e	Electron charge
E	Electric field / Transmitted THz electric field under dark conditions
E_b	Exciton binding energy
E_{ex}	Transmitted THz electric field under photoexcitation
EFISHG	Electric field induced second harmonic generation
E_g	Band gap energy
F	Fourier transform / Fluence
f_{abs}	Absorptance
FFT	Fast Fourier transform
FLUPS	Fluorescence up-conversion spectroscopy
FWHM	Full width at half maximum
FWM	Four-wave mixing
G	Generation term
GSB	Ground state bleaching
H	Magnetic field
\hbar	Reduced Planck constant
HDPE	High density polyethylene
HOIP	Hybrid organic-inorganic perovskite
HTM	Hole transporting material
I	Intensity
IRF	Instrument response function
J	Current
k	Wavevector / Rate constant
k_1	Hot carrier cooling rate constant (Bulk perovskites)
k_{-1}	Cold carrier heating rate constant (Bulk perovskites)
k_2	Polaron formation rate constant (Bulk perovskites)
k_3	Phonon decay rate constant (Bulk perovskites)
k_4	Hot polaron cooling rate constant (Bulk perovskites)
k_a	Exciton-exciton annihilation rate constant (2D perovskites)

k_B	Boltzmann constant
k_c	Cooling rate constant (2D perovskites)
k_{ed}	Exciton dissociation rate constant (2D perovskites)
k_{ef}	Exciton formation rate constant (2D perovskites)
k_{er}	Exciton recombination rate constant (2D perovskites)
L	Thickness
L_e	Effective thickness
LA	Longitudinal acoustical
LHP	Lead halide perovskite
LO	Longitudinal optical
m	Particle mass
m_e	Electron mass
m^*	Effective mass
m_b	Effective mass before electron-phonon coupling
n	Particle occupancy / Refractive index / number of layers
N	Charge carrier density
N_e	Electron density
NFP	Nanosecond flash photolysis
N_h	Hole density
NOPA	Non-collinear optical parametric amplifier
N_p	Photon density
NW	Nanowire
OPA	Optical parametric amplifier
P	Dielectric polarization / Power
PCE	Power conversion efficiency
PEA	Phenethylammonium
PET	Polyethylene terephthalate
PMMA	Poly(methyl methacrylate)
PMT	Photomultiplier tube
PP	Polypropylene
PS	Polystyrene
PSC	Perovskite solar cell
PTFE	Polytetrafluoroethylene

QW	Quantum well
R	Large monovalent spacer cation
R_b	Bohr radius
RP	Ruddlesden-Popper phase
SEM	Scanning electron microscopy
SHE	Standard hydrogen electrode
SHG	Second harmonic generation
SRH	Shockley-Read-Hall recombination mechanism
t	Time / Goldschmidt tolerance factor
T	Temperature
TA	Transverse acoustical
TAS	Ultrafast transient absorption spectroscopy
T_c	Carrier temperature
TDS	Time-domain spectroscopy
TFISHG	THz field induced second harmonic generation
T_l	Lattice temperature
TO	Transverse optical
TPX [™]	Trademark for polymethylpentene
TRTS	Time-resolved THz spectroscopy
VBM	Valence band maximum
v	Electron velocity
v_e	Electron net velocity
v_d	Electron drift velocity
w	Width parameter (FWHM)
WL	White light
WLC	White light continuum
X	Halide
x	Carrier fraction
α	Fröhlich coupling constant / Absorption coefficient
γ	Resonance width
$\delta(t)$	Dirac delta function
$\Delta\sigma$	Photoconductivity

$\Delta\sigma_{DC}$	DC photoconductivity
ΔA	Change in Absorbance
ΔE	Photoexcited change in the transmitted THz electric field
ϵ	Energy
ϵ_F	Fermi level
ϵ	Permittivity
ϵ_0	Vacuum permittivity / Static permittivity
ϵ_{inf}	Electronic or high frequency permittivity
ϵ_r	Relative permittivity
θ	Phase shift
$\Theta(t)$	Unit step function
λ	Wavelength
λ_{exc}	Excitation wavelength
λ_{obs}	Probing wavelength
μ	Mobility / Exciton reduced mass / Magnetic permeability
μ_{DC}	DC mobility
μ_e	Electron mobility
μ_{Fp}	Fröhlich polaron mobility
μ_h	Hole mobility
μ_{sp}	Small polaron mobility
ν	Frequency
σ	Conductivity
σ_{DC}	DC conductivity
τ	Scattering time constant / Time delay / Fitted time constant
τ_c	Hot carrier cooling time constant (2D perovskites)
τ_{ef}	Exciton formation time constant (2D perovskites)
ϕ	Phase / Carrier generation yield
χ_e	Electric susceptibility
ω	Angular frequency
Ω	Phonon angular frequency
ω_{LO}	LO phonon angular frequency
ω_p	Plasma frequency
ω_0	Resonance frequency



ANDRÉS BURGOS CAMINAL

PERSONAL INFORMATION

andres.burgos.caminal@gmail.com
(+41) 78 808 08 31
(+34) 664 363 454

Nyon, Switzerland
Barcelona, Spain

Born: December 11th, 1992. Barcelona

SKILLS

Problem solving
Ability to work independently
Team work
Scientific writing
Research

Mathematica ●●●●○
Matlab ●●●●○
Visual Basic ●●●○○
Python ●●●○○
LabVIEW ●●○○○

LANGUAGES

Spanish ●●●●●
Catalan ●●●●●
English ●●●●●
French ●●●●○

PROFILE

I am a physical chemist specialized in laser spectroscopy. My main interests lie in the study of photoexcited dynamics at ultrafast timescales in relevant materials for solar energy conversion. I have used many time-resolved techniques to study different systems such as photovoltaic semiconductors, nanomaterials or photosensitizing proteins. In particular, my PhD research mainly focused on perovskite materials, unraveling the early dynamics, through the study and modeling of complex kinetics. In addition, I am interested in the development of optical systems such as the ultra-broadband time-resolved THz spectroscopy setup I built during my PhD. I also enjoy programming both to improve my research and as part of setup development.

WORK EXPERIENCE

PhD Researcher Assistant 2016 - 2020
EPFL (École Polytechnique Fédérale de Lausanne, Switzerland)

Ultrafast spectroscopy on optoelectronic materials, with a special interest on PV materials. I built an ultra-broadband THz spectroscopy setup based on gas photonics which I then used to carry out my research.

○ **Safety Coordinator (COSEC)** 2018 - 2020
In charge of coordinating my lab unit with the safety department. I took care of safety related issues, such as assigning lab tasks, introducing new safety regulations and scheduling lab safety visits.

○ **Teaching Assistant** 2016 - 2019
General and organic chemistry exercises. Practical work supervision in general chemistry. Exam proofing and grading. Semester project supervision of a Master student. Lecturer substitution.

EDUCATION

EPFL (École Polytechnique Fédérale de Lausanne) - Switzerland
PhD, Chemistry
2016 - 2020

EPFL (École Polytechnique Fédérale de Lausanne) - Switzerland
Master's degree, Chemistry
2014 - 2016

IQS (Institut Químic de Sarrià), Barcelona - Spain
Bachelor's degree, Chemistry
2010 - 2014

PUBLICATIONS

- E. Socie, B. R. C Vale, A. Burgos-Caminal and J.-E. Moser. Direct Observation of Shallow Trap States in Thermal Equilibrium with Band-Edge Excitons in Strongly Confined CsPbBr₃ Perovskite Nanoplatelets. *Submitted* (2020)
- A. Burgos-Caminal, E. Socie, M. E. F. Bouduban and J.-E. Moser. Exciton-Carrier Dynamics in 2D Perovskites. *Preprint: arXiv:2006.03843* (2020)
- A. Burgos-Caminal *et al.* Hot Carrier Mobility Dynamics Unravel Competing Sub-ps Cooling Processes in Lead Halide Perovskites. *Preprint: arXiv:1909.04589* (2019)
- B. R. C Vale, E. Socie, A. Burgos-Caminal *et al.* Exciton, Biexciton, and Hot Exciton Dynamics in CsPbBr₃ Colloidal Nanoplatelets. *J. Phys. Chem. Lett.* **11**, 387–394 (2019).
- E. A. Alharbi *et al.* Atomic-Level Passivation Mechanism of Ammonium Salts Enabling Highly Efficient Perovskite Solar Cells. *Nat. Commun.* **10**, 3008 (2019).
- W. Yan, A. Burgos-Caminal, T. Das Gupta, J.-E. Moser and F. Sorin. Direct Synthesis of Selenium Nanowire Mesh on a Solid Substrate and Insights into Ultrafast Photocarrier Dynamics. *J. Phys. Chem. C* **122**, 25134–25141 (2018).
- M. E. F. Bouduban, A. Burgos-Caminal, R. Ossola, J. Teuscher and J.-E. Moser. Energy and Charge Transfer Cascade in Methylammonium Lead Bromide Perovskite Nanoparticle Aggregates. *Chem. Sci.* **8**, 4371–4380 (2017).
- M. E. F. Bouduban, A. Burgos-Caminal, J. Teuscher and J.-E. Moser. Unveiling the Nature of Charge Carrier Interactions by Electroabsorption Spectroscopy: An Illustration with Lead-Halide Perovskites. *Chimia* **71**, 231–235 (2017).
- J. Torra, A. Burgos-Caminal *et al.* Singlet Oxygen Photosensitisation by the Fluorescent Protein Pp2FbFP L30M, a Novel Derivative of Pseudomonas Putida Flavin-Binding Pp2FbFP. *Photochem. Photobiol. Sci.* **14**, 280–287 (2015).

TALKS

- Hybrid & Organic Photovoltaics (HOPV) international conference. 2019, Rome.
- Swiss Chemical Society (SCS) fall meeting. 2019, Zürich.
- Swiss Chemical Society (SCS) fall meeting. 2018, Lausanne.

POSTERS

- Ultrafast Science & Technology Spain (USTS) meeting. 2019, Madrid.
- Perovskite Solar Cells and Optoelectronics (PSCO) International conference. 2019, Lausanne.
- Swiss Chemical Society (SCS) photochemistry symposium. 2019, Fribourg.
- Materials Research Society (MRS) spring meeting. 2019, Phoenix. Best poster nominee.

- National Center of Competence in Research - Molecular Ultrafast Science and Technology (NCCR MUST) annual meeting. 2019, Grindelwald.
- National Center of Competence in Research - Molecular Ultrafast Science and Technology (NCCR MUST) annual meeting. 2018, Grindelwald.
- Perovskite Solar Cells and Optoelectronics (PSCO) International conference. 2017, Oxford.
- Swiss Chemical Society (SCS) fall meeting. 2017, Bern.
- National Center of Competence in Research - Molecular Ultrafast Science and Technology (NCCR MUST) annual meeting. 2017, Grindelwald.
- Swiss Chemical Society (SCS) fall meeting. 2016, Zürich.
- Perspectives on photonics: the route from materials to devices, summer school. 2016, Gstaad.

OUTREACH

- Photochemistry introduction and demonstration for secondary school students, Escola Joan Pelegrí. 2019, Barcelona.
- Introduction to solar energy conversion for chemistry students, Institut Químic de Sarrià (IQS). 2016, Barcelona.